7-1-2016

Thin film AlSb carrier transport properties and room temperature radiation response

Erin Vaughan

Erin Ivey Vaughan
Candidate

Nuclear Engineering
Department

This dissertation is approved, and it is acceptable in quality and form for publication:

Approved by the Dissertation Committee:

Adam A. Hecht, Chairperson

Ganesh Balakrishnan

Cassiano de Oliviera

Ashwani K. Sharma

Thin film AlSb carrier transport properties and room temperature radiation response

by

Erin Ivey Vaughan

B.A., Astrophysics, University of New Mexico, 2006

M.S., Nuclear Engineering, University of New Mexico, 2013

DISSERTATION

Submitted in Partial Fulfillment of the
Requirements for the Degree of

Doctor of Philosophy
Engineering

The University of New Mexico
Albuquerque, New Mexico

July, 2016

Acknowledgements

A great deal of gratitude is reserved for my graduate research advisor, Dr. Adam A. Hecht, who was quite patient with me over the years, and who taught me how to be an engineer. He is meticulous about the details, knowledgeable about the science, and undeniably committed to his students. Dr. Ganesh Balakrishnan was also a great mentor and was very influential during my research projects. In addition to providing a highly functional research team to grow and characterize samples for my research, he was also always able to offer an explanation for whatever weird phenomena I was observing in my experiments. The other members of my dissertation committee, Dr. Ashwani K. Sharma and Dr. Cassiano de Oliveira, were generous with their time and constructive criticism with regard to the preparation and presentation of this manuscript.

Thanks to Stephen Clark, Orlando Romero, Tom Rotter, Nassim Rahimi, Sadhvikas Addamane, Emma Renteria, and Darryl Shima for their hard work growing and conducting quality characterization measurements on my samples. Also, for teaching me how to do some of the characterization myself and for explaining the meaning and implication of the results. Thanks to Chris Hains for helping me troubleshoot and repair equipment issues in the lab.

Special consideration is given to Dr. Stephen Johnston of the National Renewable Energy Laboratory in Golden, CO, for the donation of his time and access to resources

used to perform lifetime measurements.

My father, Fred K. Husher, has been invaluable during my time as a graduate student. His ingenuity and generosity were most exemplified by the design and construction of a microprobe station and a current source mirror, without which I would not have been able to complete my research. Countless hours of phone discussions with him helped me work out a multitude of issues, and re-energized my spirits when things seemed overwhelming.

Many hours of babysitting were provided by my sister, Brianne Reynolds, and my aunt, Vivian Jones, allowing me some much needed quiet time to devote to the writing of this manuscript.

My loving and supportive husband, Jeremy, was always there to remind me that life is bigger than whatever academic matter or research woe was bothering me at the moment. He is my constant and my best friend. Becoming a mother to our darling baby, Owen, during my last year as a graduate student made things substantially more challenging, but that much more fulfilling. Thanks, Jeremy, for your "Daddy-daycare" days, and Owen, for your sweet snuggling breaks. Now Mommy will have more time for both of you.

Thin film AlSb carrier transport properties and room temperature radiation response

by

Erin Ivey Vaughan

B.A., Astrophysics, University of New Mexico, 2006

M.S., Nuclear Engineering, University of New Mexico, 2013

Ph.D., Engineering, University of New Mexico, 2016

Abstract

Theoretical predictions for AlSb material properties have not been realized using bulk growth methods. This research was motivated by advances in molecular beam epitaxial (MBE) growth technology to produce high-quality thin-film AlSb for the purpose of evaluating transport properties and suitability for radiation detection. Simulations using MCNP5 were performed to benchmark an existing silicon surface barrier detector and to predict ideal AlSb detector behavior, with the finding that AlSb should have improved detection efficiency due to the larger atomic number of Sb compared with Si. GaSb diodes were fabricated by both homoepitaxial MBE and ion implantation methods in order to determine the effect on the radiation detection performance. It was found that the radiation

response for the MBE grown GaSb diodes was very uniform, whereas the ion-implanted GaSb diodes exhibited highly variable spectral behavior. Two sets of AlSb heterostructures were fabricated by MBE methods; one for a Hall doping study and the other for a radiation response study. The samples were characterized for material quality using transmission electron microscopy (TEM), Nomarski imaging, atomic force microscopy (AFM), x-ray diffraction (XRD), I-V curve analysis, and Hall effect measurements. The Hall study samples were grown on semi-insulating (SI) GaAs substrates and contained a thin GaAs layer on top to protect the AlSb from oxygen. Doping for the AlSb layer was achieved using GaTe and Be for n- and p-type conductivity, respectively, with intended doping densities ranging from 10^{15} to 10^{17} cm^{-3}. Results for net carrier concentration ranged 2×10^{9} to 1×10^{17} cm^{-3}, 60 to 3000 cm^2/Vs for mobility, and 2 to 10^6 Ω-cm for resistivity, with the undoped AlSb samples presenting the best values. The radiation detector samples were designed to be PIN diodes, with undoped AlSb sandwiched between n-type GaAs substrate and p-type GaSb as a conductive oxygen-protective layer. Energy spectra were measured from ^{241}Am, ^{252}Cf, and ^{239}Pu sealed sources, with good peak resolution and signal to noise response. Both GaSb PN diodes and AlSb PIN diodes exhibited larger pulses for smaller surface area samples, in good agreement with voltage-capacitance relationships for junctions. Microwave photoconductive decay (MW-PCD) measurements were performed on the Hall samples to determine the effect of doping on the minority carrier lifetime. Contrary to expectations, more heavily doped samples presented with longer decay times, some as large as hundreds of microseconds. There also appeared to be multiple exponential decay curves, potentially associated with different decay mechanisms. Collectively, the

studies presented here reinforce the predicted nature of AlSb with respect to radiation detection.

Contents

List of Figures

List of Tables

Chapter 1

Motivation & Background

1.1 Motivation for Research

1.1.1 Introduction

For gamma radiation, the most popularly used detectors are sodium-iodide (NaI) scintillators, high-purity germanium (HPGe) semiconductors and cadmium-zinc-telluride (CZT) semiconductors. For optimal resolution, HPGe detectors must be cooled to liquid nitrogen temperatures, limiting portability and ease of use. NaI detectors are operable at room temperatures but are significantly inferior to HPGe with respect to energy resolution. The most recent addition, CZT, operates at room temperature, has improved resolution [1] (compared to NaI), but has low hole mobility, reducing it to a single charge carrier detector. This is a well-known disadvantage that results in poor spectral performance [2], and reduced photopeak efficiency [1]. This also limits the detector size to maintain reasonable resolution, as an event near the cathode will have different charge collection properties than an event near the anode [2]. This effect will be revisited in detail in the following subsection.

Advancements in modern technology involving semiconductor production

introduces new materials to be considered for use in this field. The properties that impact the performance of semiconductor materials will be covered extensively in the following subsection. Of the many compounds recently explored by various researchers, aluminum antimonide (AlSb) has several promising properties for radiation detection, some of which suggest that it may be operable at room temperature while maintaining good resolution. There are, however, several properties that remain unknown. Until recently, bulk growth methods had primarily been used to produce AlSb and, due to difficulties with the material reacting with air and crucibles, high levels of defects were observed. In spite of the encouraging theorized and measured characteristics [2, 3], this reactivity has prevented production of AlSb by any method with low enough defect levels to achieve a gamma-ray induced response measurable above noise.

1.1.2 Desirable Properties for Radiation Detection

When energetic photons interact with the semiconductor detector, a large number of electron-hole pairs are generated proportional to the energy deposited by the incident photon. A reverse bias is applied to produce a depletion region so no current flows except for charge liberated by radiation in the depletion region itself. This depletion region is the active region of the detector. Due to the applied electric field the electrons and holes move as charge carriers through the semiconductor device toward the opposing electrodes. The charge induced on the electrodes varies according to the movement of the charge carriers and this charge is converted to a voltage pulse using a charge sensitive amplifier. The signal

amplitude should be proportional to the energy deposited by the gamma radiation. [4]

The intrinsic or engineered crystal properties involving the generation and transit of electrons and holes are of considerable interest. For optimal device performance with respect to detection of high-energy photons, a few parameters require careful consideration. These include the atomic numbers of the constituents, the band gap of the material, the mobility of both electrons and holes, the electron-hole recombination time and trapping time of the carriers, and the noise contribution from electrical contacts. [5]

1.1.2.1 Atomic Number, Z

The three types of photon interactions that are important for radiation detection measurements are photoelectric absorption, Compton scattering and pair production. The third mechanism only occurs when the incident photon energy exceeds 1.02 MeV (twice the electron mass energy), and remains highly improbable until photon energies reach several MeV [6]. This work is more confined to the sub-MeV region where photoelectric and Compton effects are relevant.

Semiconductor compounds with large atomic number Z exhibit a high interaction cross-section for energetic photons. As the atomic number increases, the likelihood of photoelectric effect interactions occurring at higher incident photon energies also increases, expanding the range over which full photon energies are absorbed, thus improving the peak efficiency. The photoelectric effect dominates photon interactions below a few hundred keV, and that effect is strongly dependent on the atomic number of the material and may

be several orders of magnitude larger than the Compton scattering cross section. Above that energy, Compton scattering is less strongly dependent on, but scales linearly with, Z.

During photoelectric effect interactions all of the photon energy is absorbed in the collision. An inner shell electron is then ejected, called a photoelectron, from the atom with a kinetic energy equal to the difference between the incident photon energy (hν) and the electron binding energy (E_1), $E=h\nu-E_1$. Then, an outer shell electron moves to fill the vacancy, resulting in the emission of characteristic x-rays which are also typically absorbed in the material. The absorption cross section for photoelectric effect photons is:

$$ {}^{a}_{p}\sigma = AZ^{n}(h\nu)^{-s} \qquad (1) $$

where A is constant, $4<n<5$ and $1<s<3.5$ [7].

The mass attenuation plot in Figure 1 illustrates how the cross section for the photoelectric effect (PE) decreases with increasing incident photon energy for AlSb ($Z_{Sb}=51$, $Z_{Al}=13$) and Ge (Z=32), and is a trend with all materials. The log-log representation of the plot is shown to illustrate large-scale features but it should be noted that the interaction cross section is 10,000 times larger for 1 keV photons than for 100 keV photons.

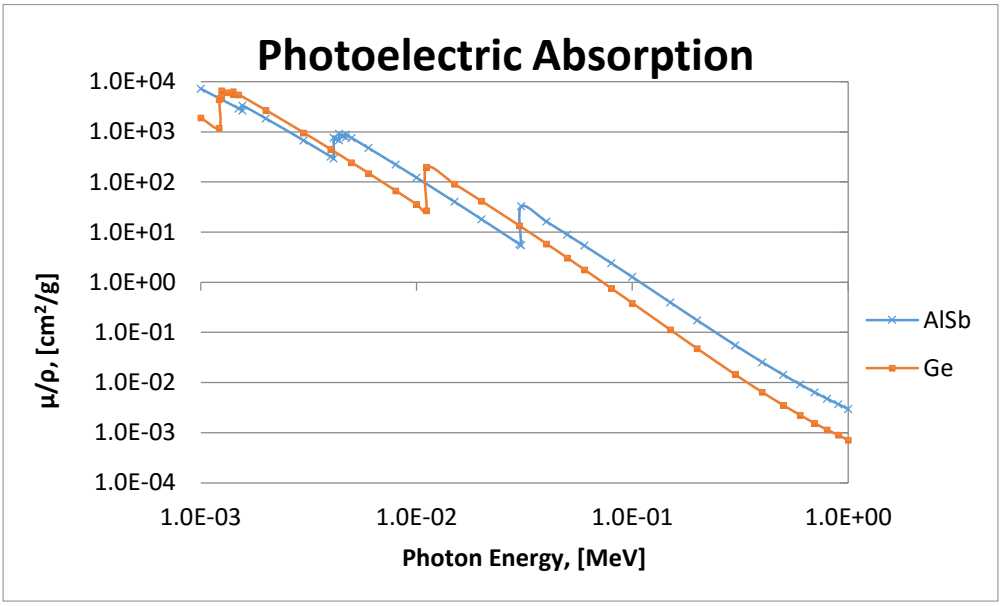

Figure 1.Mass attenuation curves for AlSb and Ge [8].

A Compton scattering interaction occurs when an incident photon collides with a stationary electron, transferring a portion of its energy. The energy transferred is dependent on the scattering angle and can range from zero to a large fraction of the gamma ray energy. If zero energy is transferred the photon retains its initial energy (hν) and simply scatters with a scattering angle of zero degrees, according to equation (2), where hν' is the scattered photon energy. [6]

$$h\nu' = \frac{h\nu}{1 + \frac{h\nu}{m_0 c^2}(1 - cos\theta)} \tag{2}$$

The scattered photon can then be reabsorbed by photoelectric effect resulting in a full energy deposition.

An atomic number greater than 40 is said to be competitive with germanium

without requiring excessive detector thickness. [5, 7, 9]

1.1.2.2 Band Gap

The energy difference between the conduction band and the valence band, commonly referred to as the band gap, determines the energy required to ionize atoms within the crystal. A smaller band gap means a greater number of charge carriers (N) are released per energy deposited and, due to higher statistics and lower proportional variation, higher resolution. From Poisson statistics, the relationship to the device resolution (from the standard deviation, $\sigma = (E_\gamma/\varepsilon)^{1/2}$ goes approximately as $N^{1/2}$, or $\varepsilon^{-1/2}$, where ε represents the energy required to form an electron-hole pair. The proportional uncertainty, σ_E/E goes as $(\sqrt{N})/N = 1/\sqrt{N}$ and so a smaller band gap, and thus a larger N, for the energy deposited improves resolution.

The probability of thermal ionization is also larger for a smaller band gap; so narrow band gap detectors must be operated at very low temperatures for optimal performance. The number of thermal carriers generated is proportional to $\exp(-E_g/k_BT)$, where E_g is the band gap energy, k_B is the Boltzmann constant, and T is absolute temperature. Increased E_g allows for increased T. If the band gap is larger, dopants (which are used to provide steps across the band gap) can be used to accurately adjust the physical properties of the semiconductor to suit the targeted energy detection range.

For room temperature operation with intrinsic detector noise reduced to an acceptable level, a band gap between about 1.4 and 2.2 eV is optimal. The lower limit

reflects the minimization of the background signal from thermally generated carriers, while the upper limit represents a maximization of the number of carriers generated as a result of radiation energy deposited. [10]

The distribution of electrons in a semiconductor device is governed by the Fermi function, equation (3) below, and is illustrated by the diagrams in Figure 2.

$$f(E) = \frac{1}{1 + \exp\left(\frac{E - E_F}{k_B T}\right)} \tag{3}$$

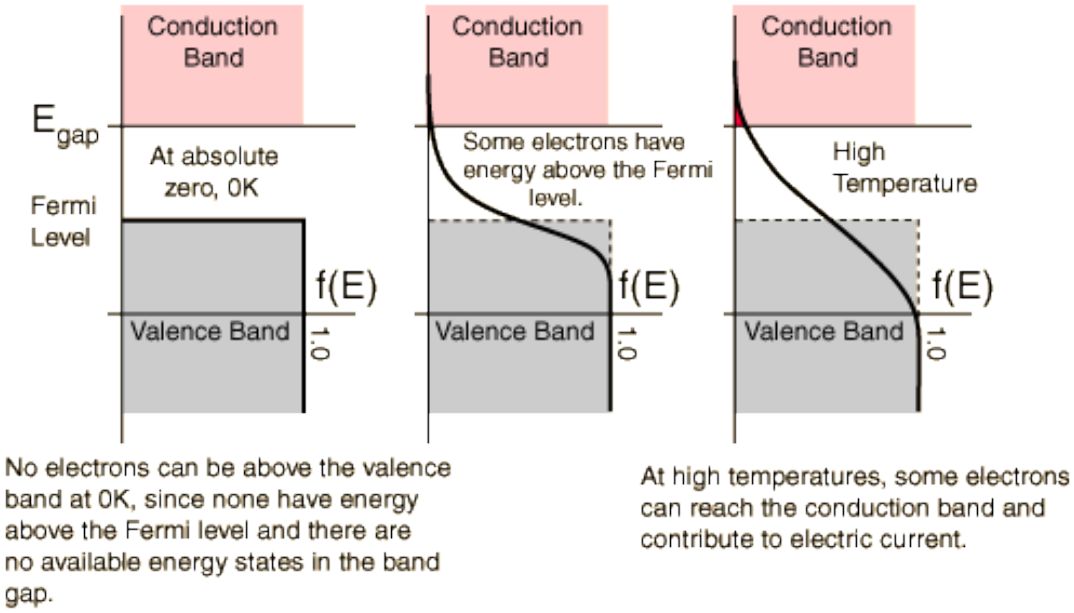

Figure 2. Fermi-Dirac distribution with increasing temperature [11].

The number of available states, or the density of states (ρ), is given in equation (4) as a function of energy. The product of the density of states and the probability of

occupation of those states gives the number of electrons per volume with energy between E and dE.

$$\rho(E) = \frac{8\sqrt{2}\pi m^{3/2}}{h^3}\sqrt{E - E_{gap}} \tag{4}$$

$$N(E)dE = \rho(E)f(E)dE = \frac{8\sqrt{2}\pi m^{3/2}}{h^3}\sqrt{E - E_{gap}}\,\frac{1}{e^{(E-E_F)/kT} + 1}dE$$
$$where \quad E_F = \frac{E_{gap}}{2} \tag{5}$$

As equation (6) shows, the electron population in the conduction band, N_{cb}, can be calculated by integrating this product from the top of the band gap to infinity. [12]

$$N_{cb} = \int_{E_{gap}}^{\infty} N(E)dE = AT^{3/2}e^{-E_{gap}/2kT}$$
$$where \;\; A = \frac{8\sqrt{2}(\pi mk)^{3/2}}{h^3} = 4.83 \times 10^{21}\,\frac{electrons}{m^3K^{3/2}} \tag{6}$$

The number of thermally generated electrons was calculated for relevant band gap energies and temperatures, shown in Table 1. Values for HPGe are given for liquid nitrogen and room temperatures. Notice that fewer thermal electrons are generated for AlSb than for CZT.

Table 1. Numbers of electrons in the conduction band for HPGe cooled to liquid nitrogen temperatures, CZT and AlSb at room temperature, and the upper and lower limits for desirable band gap for semiconductor radiation detectors.

Semiconductor Material	**E_{gap} [eV]**	**Temperature [K]**	**Number of Electrons in Conduction Band [electrons/ m^3]**
HPGe	0.74	77	1.98
HPGe	0.67	300	1.53×10^{19}
Lower Limit	1.4	300	4.36×10^{13}
CZT	1.57	300	1.63×10^{12}
AlSb	1.61	300	9.11×10^{11}
Upper Limit	2.2	300	8.31×10^{6}

Figure 3 illustrates the effect of a reverse bias on a semiconductor with a P-I-N junction [13]. The "P" region represents an extrinsic p-type semiconductor material with intentionally added acceptors, or holes, whereas the "N" region contains excess donors, or electrons. Placed between the p+ and n+ doped regions, the "I" region is ideally intrinsically semi-insulating and provides for a constant electric field through a large depletion zone. This allows for the consistent proportionality of the output signal to the energy deposited by incident radiation interactions.

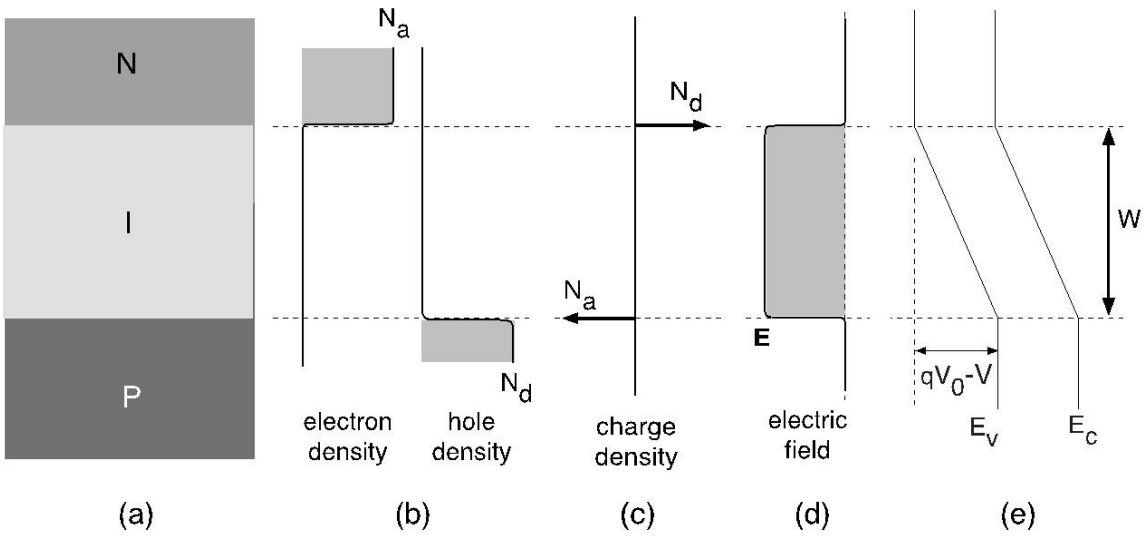

Figure 3. Diagrams showing the (a) structure, (b) carrier distribution, (c) charge distribution, (d) electric field, and (e) energy bands of a P-I-N diode under reverse bias [13].

1.1.2.3 Dual Carrier Transport

The transport of charge carriers in semiconductor materials is a crucial intrinsic parameter, which can be evaluated by observing the drifting behavior of electrons and holes under an applied bias voltage. As Knoll [6] describes in detail, the output pulse begins to form the moment the particle deposits its energy in the detector. At that point, the charge carriers begin to travel towards their respective electrodes and the motion of the carriers is what causes the signal to form, a process known as charge induction.

To understand the pulse shape seen on the oscilloscope induced by the motion of the charge carriers, a simple parallel plate capacitor can be used to model the planar diode

detector. When a constant voltage potential (V_0) is applied across the parallel plate spacing (d), an electric field (ε) is formed. And, if a radiation event causes a number of electron-hole pairs (n_0) to be generated at a position between the plates, at a distance x from the positively charged plate, an electric potential (φ) is established. The energy required to move a positive charge (q_0) through an electric potential difference ($d\varphi$) is $dE = -q_0 d\varphi$. $\varepsilon(x)$ and $\varphi(x)$ are related differentially by $\varepsilon(x) = -d\varphi(x)/dx$, and the absorbed energy as a function of position is

$$\frac{dE}{dx} = q_0 \varepsilon(x) = q_0 \frac{V_0}{d} \quad . \tag{7}$$

The stored energy of the parallel plate capacitor, proportional to the capacitance (C) by $E = (CV_0^2)/2$, is used to move the carriers from their formation position towards their respective electrodes. The velocities of the carriers (v_h *for holes and* v_e *for electrons*) and the travel time (t) determine how much of the stored energy is absorbed by the carriers during transit. Energy is conserved in this process, as described by the following equation of equilibrium:

$$\frac{1}{2} C V_0^2 = n_0 e E v_h t + n_0 e E v_e t + \frac{1}{2} C V_{ch}^2 \tag{8}$$

where the last term represents the remaining stored energy in the capacitor. The signal voltage $V_R = V_0 - V_{ch}$ is usually small compared to V_0, so the following approximations can be made:

$$V_0 + V_{ch} \cong 2V_0$$

$$\frac{V_{ch}}{d} = \frac{V_0}{d}$$

Rearranging terms in equation (8) and substituting in the approximations, equation (9) represents the rising portion of the signal pulse, and applies only during the period of time when both electrons and holes are in motion.

$$V_R = \frac{n_0 e}{dC}(v_h + v_e)t \tag{9}$$

A negative (or positive) change in the voltage potential difference occurs when the hole (or electron) drifts a distance $x = v_h t$ *(or* $x = v_e t$*)*, and is equivalent to a decrease (or increase) in capacitance by an amount $n_0 e v_h t/d$ *(or* $n_0 e v_e t/d$*).* When the holes (or electrons) reach the cathode (or anode) after a time $t_h = x/v_e$ *(or* $t_e = (d-x)/v_h$*)*, equation (9) becomes

$$V_R = \frac{n_0 e}{dC}(v_h t + x) \quad for\ electrons, and$$

$$V_R = \frac{n_0 e}{dC}[(d - x) + x] = \frac{n_0 e}{C} \quad for\ holes \tag{10}$$

To reiterate, the process of inducing charge does not require that the charge carriers reach their respective electrodes, only that they are in motion. However, the maximum pulse amplitude occurs when the all of the charge carriers are collected at the appropriate electrodes. At this point, the maximum signal voltage is simply

$$V_R = \frac{n_0 e}{C} \tag{11}$$

In terms of the energy absorbed by the carriers as they move from x_0 to x,

$$\Delta E = \int_{x_0}^{x} dE = q_0 V_0 \int_{x_0}^{x} dx = \frac{q_0 V_0}{d}(x - x_0) \tag{12}$$

$$\Delta V_R = \frac{\Delta E}{C V_0} = \frac{q_0}{C}\frac{(x - x_0)}{d} \tag{13}$$

The induced charge is then

$$\Delta Q = C \Delta V_R = q_0 \frac{(x - x_0)}{d} \tag{14}$$

The Shockley-Ramo theorem is used to describe the instantaneous current induced on a given electrode (*i*), and can be written as

$$i = q\vec{v} \cdot \vec{E}_0 \tag{15}$$

where q is the carrier charge, $\vec{v}$ is the carrier velocity, and $\vec{E}_0$ is the weighting field. When the last charge carrier reaches the electrode the pulse has fully formed, and information regarding the nature of the incident radiation particle can be deduced. The timing behavior of the detector is governed by the intrinsic transport properties of the detector material.

For optimal signal generation, a quantity known as charge induction efficiency (CIE) is maximized. Simply, CIE is a ratio of the measured induced charge on an electrode (Q_m) to the charge actually created in the material (eN), CIE = Q_m/eN. For perfect charge

induction this ratio is 1, meaning the all of the holes and electrons are fully accounted for at the electrodes. In reality, impurities and defects trap charge carriers so that perfect CIE is never achieved. [2]

The product of charge mobility (μ) and carrier lifetime (τ) is of particular interest for calculating the induction efficiency, (η).

$$\eta(x) = \frac{(\mu\tau)_e E}{D}\left[1 - \exp\left(-\frac{D-x}{(\mu\tau)_e E}\right)\right] + \frac{(\mu\tau)_h E}{D}\left[1 - \exp\left(-\frac{x}{(\mu\tau)_h E}\right)\right] \qquad (16)$$

Here, D is the detector thickness, E is the electric field intensity (E = bias voltage/detector thickness for planar geometry), x is the distance from the cathode, and $(\mu\tau)_e$ and $(\mu\tau)_h$ are mobility-lifetime products for electrons and holes, respectively. Called Hecht's Relation [6], it describes the behavior of charge transport, as a function of the distance (x) from the cathode surface at which the radiation interacted and separated the charges. If the CIE is non-uniform the spectral resolution of the detector will be compromised.

As is depicted in Figure 4, germanium maintains constant CIE regardless of a carrier's distance from the electrodes. This is a result of germanium's symmetric and high μτ properties for electrons and holes, allowing for consistent charge collection. The angled line in Figure 4 represents typical values for electron and hole μτ products for a material with non-symmetric properties, such as CZT. CZT has low hole mobility and poor hole lifetime properties, compared to electron properties, which causes lower CIE for radiation interactions near the anode, following Hecht's relation [14]. This can be interpreted as holes moving slowly towards the cathode and the induced pulse thus being broad and being

lost to shorter amplifier shaping times, a ballistic defect. On top of that, defects and crystal impurities can trap charges on their path.

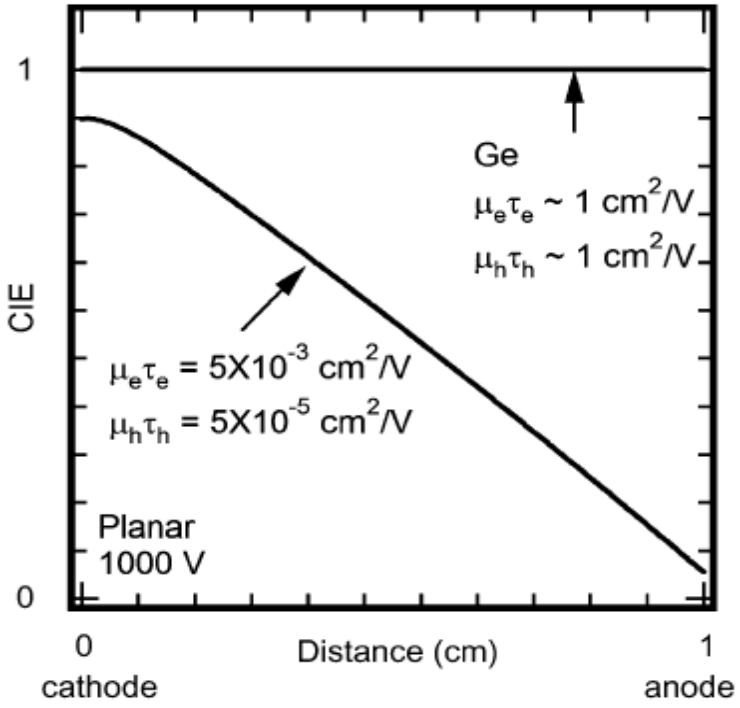

Figure 4. Charge induction efficiency as a function of radiation interaction position for two materials [2].

The result is a low energy tail in spectra, meaning poorer photo-peak efficiency within the 12-14% energy window around the photo-peak of interest [1]. This is illustrated for Tc-99m, a common isotope used in nuclear medicine, in Figure 5, where the curve shaded in yellow represents the spectrum expected from CZT and the curve without shading is indicative of a NaI spectrum.

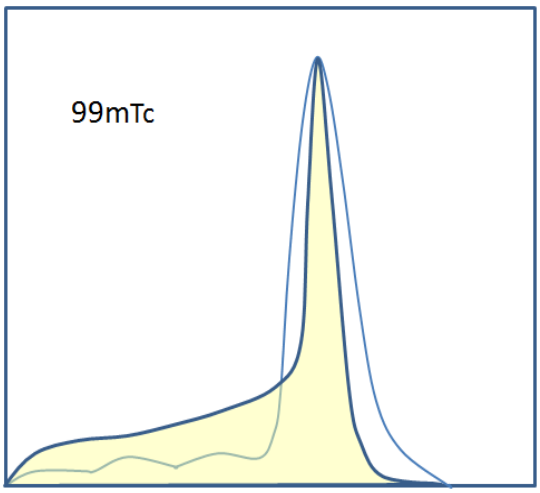

Figure 5. Tc-99m 140 keV spectra obtained with CZT (shaded in yellow) and NaI (light blue outline) [1], where the vertical axis represents the number of particles detected and the horizontal axis indicates the energy deposited in the detector by the radiation particle. Notice the low-energy tail of the CZT.

High-resolution detection requires high carrier mobilities and long carrier lifetimes. An indirect band gap can improve carrier lifetimes by quenching radiative recombination [15]. At room temperature the mobility, μ, will be limited by electron-phonon scattering, although defects in the material can cause μ to be considerably lower.

A higher carrier mobility (μ) and longer lifetime (τ) means improved charge detection. A μτ product greater than about 0.1 cm^2/V is preferred for optimal detector resolution [10], although a μτ product greater than 10^{-3} cm^2/V would be competitive with CZT.

1.1.3 Difficulties with Bulk Growth AlSb

With the exception of liquid nitrogen cooled Ge and AlSb, all of the compounds summarized in Table 2 have highly non-symmetric values for electron and hole mobilities, which suggests inferior spectral performance. While Yee *et al*. calculate relatively large theoretical mobilities for AlSb at room temperature (μe = 1100 cm2/Vs and μh = 700 cm2/Vs), other researchers observed much smaller measured values (see Table 3). Yee *et al*. also propose that the theoretical free-carrier recombination time should be on the order of 10-3 s for high quality AlSb with a net impurity concentration of about 1012-1014 cm-3. Based on the theorized properties for low-impurity defect-free AlSb, it has potential for improved performance compared to other compound semiconductor materials.

Table 2, published by Luke and Amman in 2006 [2], outlines several emerging or recently improved compound semiconductor materials that have been evaluated for desirable radiation detection properties. Cooled germanium is also included for comparison. Based on these values, it is easy to compare performance characteristics such as the peak efficiency (atomic number), room temperature operation (band gap) and consistent resolution across the energy spectrum (carrier lifetime and mobility).

With the exception of liquid nitrogen cooled Ge and AlSb, all of the compounds summarized in Table 2 have highly non-symmetric values for electron and hole mobilities, which suggests inferior spectral performance. While Yee *et al*. [5] calculate relatively large theoretical mobilities for AlSb at room temperature (μ_e = 1100 cm^2/Vs and μ_h = 700 cm^2/Vs), other researchers observed much smaller measured values (see Table 3). Yee *et*

al. [5] also propose that the theoretical free-carrier recombination time should be on the order of 10^{-3} s for high quality AlSb with a net impurity concentration of about 10^{12}-10^{14} cm^{-3}. Based on the theorized properties for low-impurity defect-free AlSb, it has potential for improved performance compared to other compound semiconductor materials.

Table 2. Useful material properties for some semiconductor radiation detectors [2].

Material	Ge (77K)	HgI_2	CdTe	CdZnTe	GaAs	AlSb
Atomic number	32	80, 53	48, 52	48, 30, 52	31, 33	13, 51
Band gap (eV)	0.74	2.13	1.50	1.57	1.43	1.6
Energy per e-h pair (eV)	2.97	4.2	4.4	4.6	4.2	?
Fano factor	0.08	0.19	0.11	0.09	0.14	?
μ_e (cm^2/Vs)	40,000	100	1100	1000	8000	1100
μ_h (cm^2/Vs)	40,000	4	100	10	400	700
τ_e (s)	10^{-3}	10^{-6}	10^{-6}	10^{-6}	10^{-8}	?
τ_h (s)	10^{-3}	10^{-5}	10^{-6}	10^{-6}	10^{-7}	?

Another noticeable feature of Table 2 is the missing information for AlSb. The difficulty involved in working with bulk AlSb has prevented reliable characterization measurements from taking place. Experiments performed by other research groups have resulted in inconsistent values being reported for important transport properties (Table 3). These include carrier recombination lifetime, mobility, resistivity, and carrier concentration. Most of the characterization reports seen in literature are representative of AlSb materials grown by bulk methods. This is a problem because AlSb oxidizes very

rapidly in air and Al and molten AlSb are extremely volatile, reacting with all types of crucible materials [16]. This leads to large concentrations of defects and impurities introduced during growth, which in turn results in poor transport and device quality. Although many bulk growth methods have been used to produce AlSb, the two most common techniques are Bridgman and Czochralski. Both methods rely on the melting of bulk elements in a crucible and using a seed crystal to "pull" the compound crystalline material. The exposure to air and contaminants from the crucibles further degrades the already temperamental AlSb.

The ranges of values reported for bulk AlSb mobility, carrier concentration, and resistivity can be seen in Table 3. Many of the samples represented in this table have one parameter that is optimized and another with a poor result.

The reason these properties seem to vary so much is that they are very sensitive to growth conditions, processing, and defects. However, the large atomic number for antimony (Z=51) and the size of the band gap (1.6 eV) are well-established values, and are encouraging for the purpose of this study. And, as Yee *et al*. point out, even poor quality AlSb has better hole transport behavior than CZT [5]. One property that seems to be consistently reported is the p-type conductivity of undoped AlSb [17, 18, 19], although theory [15, 20] predicts n-type nature for pure AlSb.

Table 3. Inconsistent reports of AlSb properties in literature.

Reference	Growth Method	Mobility [cm^2/Vs]	Carrier Concentration [cm^{-3}]	Resistivity [Ω-cm]
[10]	Bulk - Czochralski	450	1.4×10^{13}	1.5×10^{4}
[20]	Bulk – Czochralski	10	10^{13}	10^{5}
	Modified Czochralski	400-500	$> 10^{15}$	10-100
	Te-doped, Modified Czochralski	150-300	$< 10^{12}$	10^{5}
[16]	Bulk – HP Bridgman	380-520	2.7×10^{16} - 2.4×10^{17}	8×10^{4}
[21]	Bulk – Czochralski, undoped	320	2×10^{15}	10
	Se-doped Czochralski	1.3	5×10^{15}	960
	Te-doped Czochralski	630	6×10^{15}	0.2
[19]	Bulk- Czochralski	115	1.4×10^{16}	1.27
	Se-doped Czochralski	1.7(p) 3.2(n)	1.4×10^{14} 2.4×10^{14}	2.56×10^{4} 8.23×10^{3}
	Te-doped Czochralski	350(n)	4.6×10^{17}	0.04
	In-doped Czochralski	190-220(p)	$1.8\text{-}2.4\times10^{17}$	0.14-0.15
	Mn-doped Czochralski	50(p)	2.7×10^{16}	5.02
	Yb-doped Czochralski	120(p)	1.2×10^{16}	4.42
	Pr-doped Czochralski	120(p)	5.1×10^{16}	1.03

1.1.4 Thin Film AlSb

As epitaxial AlSb layers are often utilized for their well-behaved semi-insulating properties as buffer regions [22], AlSb transport properties are rarely measured. However, several doping studies have been performed previously and the resulting effect on charge transport was reported by several research groups. The pertinent details are outlined in Table 4.

Table 4. Epitaxial AlSb transport properties from literature.

Reference	Growth Method (Year)	Dopant	Mobility [cm^2/Vs]	Carrier Concentration [cm^{-3}]	Resistivity [Ω-cm]
[23]	MBE (1988)	Te (n)	45 - 65	$6 - 9\times10^{17}$	-
[24]	MBE (2000)	Be (p)	61 – 327	$10^{15} - 10^{19}$	-
		Si (p)	187 - 293	5×10^{15} to 2×10^{17}	-
[25]	CVD (2005)	unknown	200 (electrons) 400 (holes)	-	-
[26]	MBE (1982)	undoped (p)	200	10^{14}	120
		Ge (p)	50	10^{19}	-
[27]	MBE (1999)	Be (p)	172 - 327	$10^{15} - 10^{18}$	-

1.2 High Quality AlSb Grown by MBE Methods

Epitaxial growth of AlSb material has improved considerably in the last 30 years with advancements in vacuum technology, although some exposure to contaminants from source materials still occurs. Additionally, epitaxial growth allows for precise control of layer thicknesses and added dopant concentrations. While epitaxial methods are routinely used to grow AlSb, transport properties are not often measured or reported, as it is often utilized for buffer regions [22] rather than active regions within growth structures.

Molecular beam epitaxy (MBE) is a material growth technique that utilizes one or several molecular beams to deposit a series of single atomic layers, monolayers, onto a heated crystalline substrate. Solid materials are kept in evaporation cells which may be opened or closed depending on the atom or compound being deposited. The temperature of the substrate is adjusted according to the desired surface structure.

Previous AlSb research was conducted using MBE methods nearly 20 years ago in 1994. Secondary Ion Mass Spectrometry (SIMS) results are illustrated in Figure 6, which shows high oxygen content in the AlSb layer originating from oxygen incorporated during growth from the Sb source material [28].

Recent improvements in antimony purity, minimizing exposure to air during chamber loading, and more effective out-gassing techniques reduce deep level defects in AlSb associated with oxygen. These developments allow for production of an AlSb crystal that is nearly defect free and potentially detector grade. Introducing sophisticated growth techniques [29], collaborators at the Center for High Technology Materials (CHTM) at the

University of New Mexico were able to produce several AlSb crystals by MBE for use in this research.

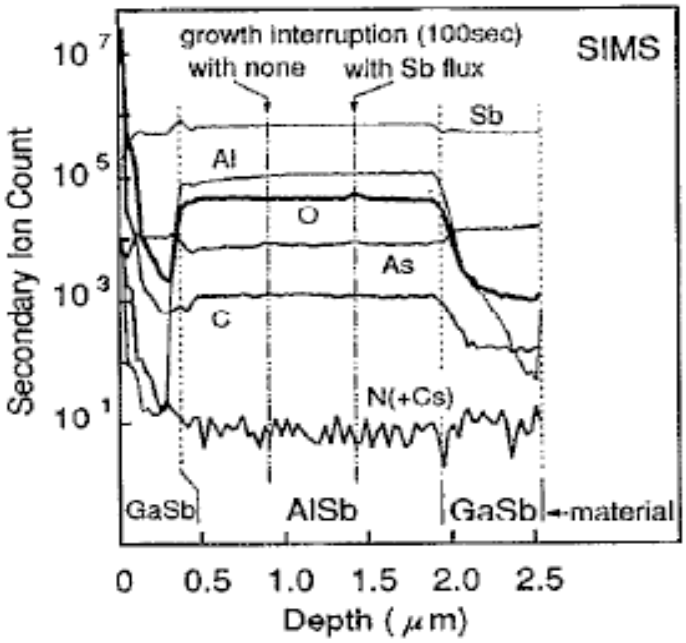

Figure 6. SIMS profile of MBE grown AlSb [28].

For the substrate material, GaAs is used exclusively in this study due to its relatively low cost (compared to GaSb) and highly-resistive, semi-insulating nature. This introduces, however, a large lattice mismatch (~8%) between the substrate and the AlSb epi-layer. The strain related defect density, which includes misfit and threading dislocations, grows quickly with increasing lattice mismatch between epi-layers [27, 30].

The diagram in Figure 7 shows the distribution of lattice constants for many semiconductor compounds while the compounds of interest for this research are circled. From this diagram it is easy to recognize compounds that have similar lattice parameters

and might be more compatible as sequential epitaxial layers during MBE growth.

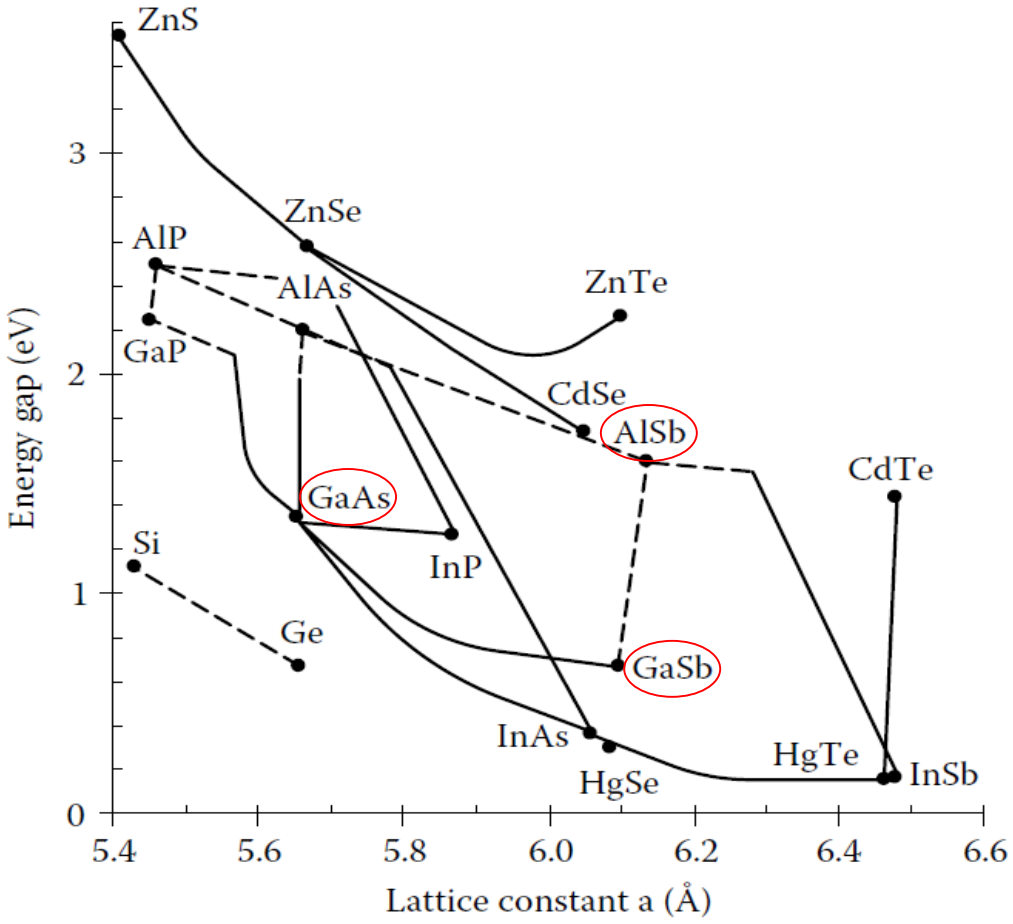

Figure 7. Lattice constants and bandgap energies for III-V semiconductors at room temperature [30]. Dashed lines indicate an indirect gap.

The strain introduced by the lattice mismatch is simply:

$$f \equiv \frac{a_s - a_e}{a_e} \ [\%] \tag{17}$$

where a_s and a_e are the lattice constants of the substrate and the epilayer, respectively. Using the lattice values in Table 5 and equation (17), the magnitude of the strain can be

calculated for each epitaxial layer. For AlSb grown directly on the GaAs substrate, a mismatch of 8.53% would introduce large strain leading to high threading dislocation densities.

Table 5. Lattice constants for important AlSb diode structure layer interfaces [30].

Compound	Lattice Constant, *a* [Å]
GaAs	5.6534
GaSb	6.0960
AlSb	6.1357

Using the Matthews and Blakeslee Force Balance Model, as is derived by Ayers [30], the thickness of an epitaxial layer of a non-homogenous structure is limited due to strain caused by mismatched lattice constants. Termed the Critical Layer Thickness, h_c can be calculated using equation (18) below.

$$h_c = \frac{b(1-\nu cos^2\alpha)[\ln\left(\frac{h_c}{b}\right)+1]}{8\pi|f|(1+\nu)cos\lambda} \tag{18}$$

For (001) zinc blende semiconductors, cosα = cosλ =1/2, b = α /√2, and ν ≈ 1/3. If a layer thickness is less than the critical thickness, $h < h_c$, the strain force will not overcome the tension between atoms in the layer. However, if the critical thickness is exceeded, $h > h_c$, lattice relaxation will occur and threading dislocations will become misfit dislocations at the epilayer interface [30]. The relationship between the critical layer thickness, as

derived by Matthews and Blakeslee, People and Bean, and van der Merwe, is shown in Figure 8 [30].

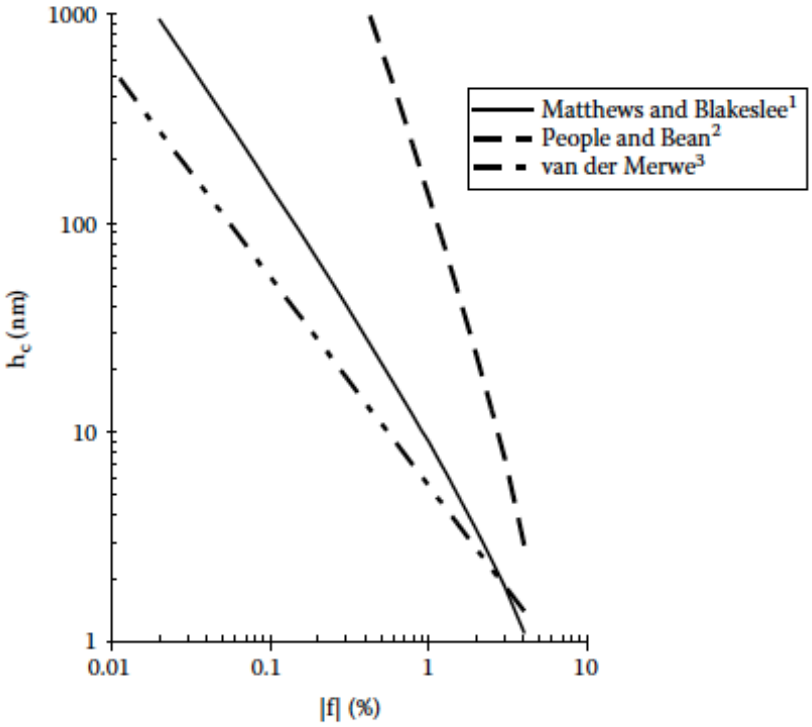

Figure 8. Critical layer thickness as a function of lattice mismatch [30].

There are three stages that occur during the epitaxial growth process. The initial stage is the pseudomorphic stage, which exists when the thickness is less than the critical thickness. The strain at this point is 100%. When the growth exceeds the critical thickness dislocations begin to occur in the material. This reduces the strain and the material is said to relax. To overcome this limiting factor, and ultimately to decrease threading dislocations propagating all the way through the structure, an interfacial misfit (IFM) dislocation layer

is employed using GaSb. Using equation (17), the mismatch between GaSb and AlSb is only 0.65%. The following images [31] in Figure 9 illustrate the formation of IFM dislocations, which would allow for strain relief between the GaSb and GaAs layers, and provide a closer lattice matched surface for subsequent AlSb growth.

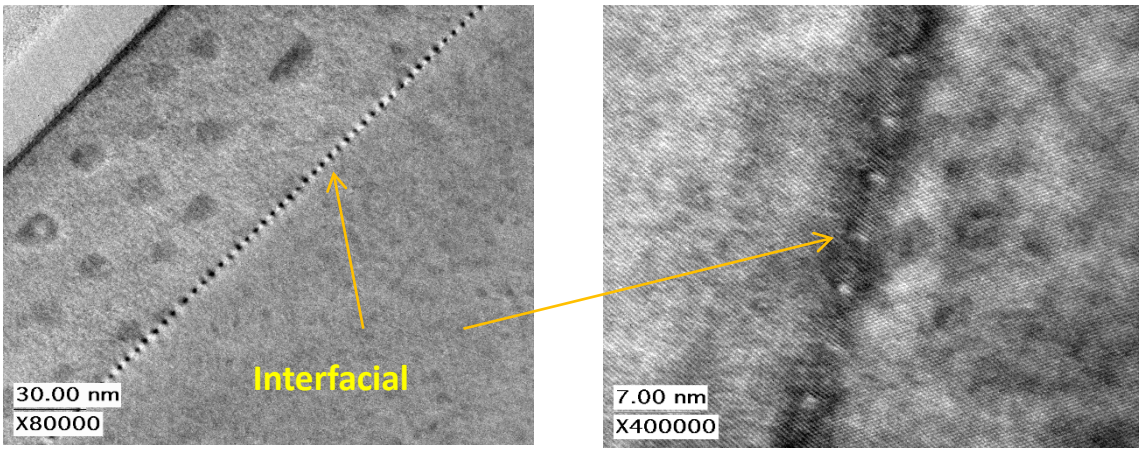

Figure 9. IFM dislocations [31].

1.3 Dissertation Outline

This dissertation is organized into five chapters, beginning with a review of the background and motivation for research. The proceeding chapter will describe the MNCP simulation models and benchmarking work performed using a silicon surface barrier detector. All input files are provided in Appendix A. Chapter 3 outlines the comprehensive proof-of-concept studies conducted using GaSb PN diodes and AlSb PIN diodes. Here, the reader will find device structure details, material quality characterization results, and radiation detector performance results. Optimization studies to investigate the influence of

doping on transport properties are covered in Chapter 4. Resistivity, carrier mobility, and recombination lifetime properties are thoroughly discussed and results of the studies are presented. Finally, a discussion of the research is provided in Chapter 5, where the results are summarized, conclusions are drawn, and avenues for additional research and future work are suggested.

Chapter 2

Simulations & Benchmarking

2.1 Introduction

To become convinced of the suggested superior performance of AlSb as a detector material, simulations and measurements were performed to benchmark an existing detector and compare the detection response with an idealized AlSb model. Next, AlSb structures were grown and characterized for material quality. This chapter is devoted to these steps. Chapter 6 will cover the radiation response of MBE grown diodes.

2.2 Radiation Detection Simulations & Benchmarking

Monte Carlo simulations were performed using floating object in vacuum geometry. To benchmark the simulation work, models were developed for a silicon surface barrier (SSB) used as a thin film x/gamma ray detector, exposed to ^{133}Ba and ^{57}Co x/gamma rays, and the results were compared to measured spectra. Simulated spectra for ^{133}Ba and ^{57}Co were broadened using MCNP Gaussian techniques to more closely approximate measured spectra.

2.2.1 Si Benchmarking Model

To benchmark simulations for AlSb detector behavior, modeling of SSB detector response was compared with measurements. Simulations were conducted using MCNP version 5 with photon data from the ENDF/B-VI.8 libraries [32]. ^{57}Co and ^{133}Ba were selected for experimental measurements for their low energy photons. This is important for thin samples where low energy photons have reasonable interaction efficiency. Because the materials were grown by MBE methods, the AlSb layer thickness was limited to 5 microns. To keep the dimensions as similar as possible, the thinnest (50 microns) SSB detector available in the lab was chosen for benchmark experiments.

The SSB detector geometry was modeled with a gold contact layer 1 micron thick and the isotropic point source was placed 1.5 mm away, as the images generated by MCNP5 in Figure 10 illustrate. The medium between the source and the detector is air (0.755636% N, 0.231475% O, and 0.012889% Ar, by weight) with a density of 0.0013 g/cm^3, depicted in yellow. In the image on the right side of Figure 10 the silicon and gold layers can be seen. The vertical lines represent boundaries for geometry splitting variance reduction.

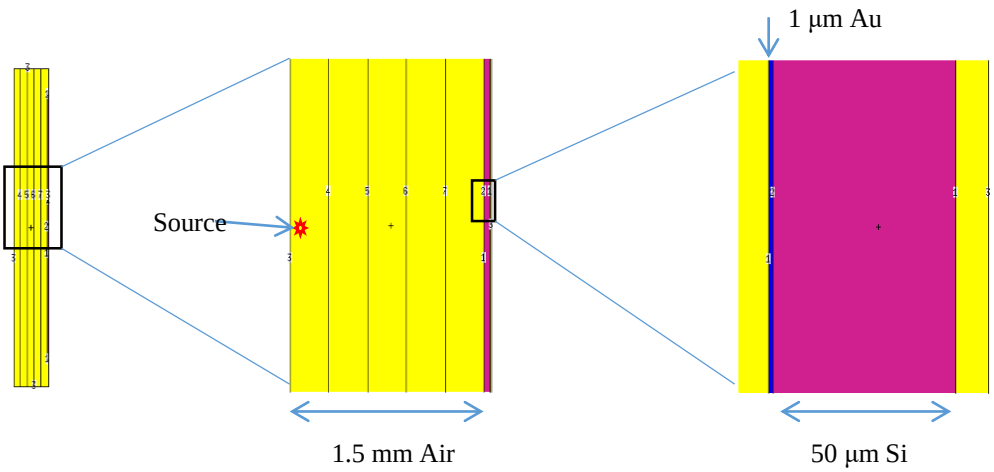

Figure 10. SSB detector geometry as modeled with MCNP5.

To determine the number of photons needed for acceptable statistics, an F4 mesh tally was applied. Figure 11 depicts the particle flux and relative error for 100,000 (two left images) and 10,000,000 photons (four right images) generated by MCNP5. The mnemonic "nps" is the terminology used in the MCNP User's Manual [33] to represent the number of histories to be tracked during a single execution. The relative error color scale is also shown at the bottom right of Figure 11, with purple representing 100% and orange representing 0% uncertainties. The two left images in Figure 11 show the side view of the SSB detector volume with boundaries corresponding to those shown in Figure 10. Shown are the photon flux (far left), most concentrated in red where the source is closest to the detector, and associated relative error (center left) where a statistical uncertainty of greater than 25% is observed over much of the region. Similarly, the images on the top right of Figure 11 represent a top view (analogous to Figure 10) of the particle flux in the detector where the

source is centered (center right) and associated relative error (far right) with most relative errors below 5%. Side views and relative errors of this same detector are shown in the lower images, (center right and far right, respectively). To reduce statistical variation to less than 5%, 10,000,000 photons were tracked for each simulation.

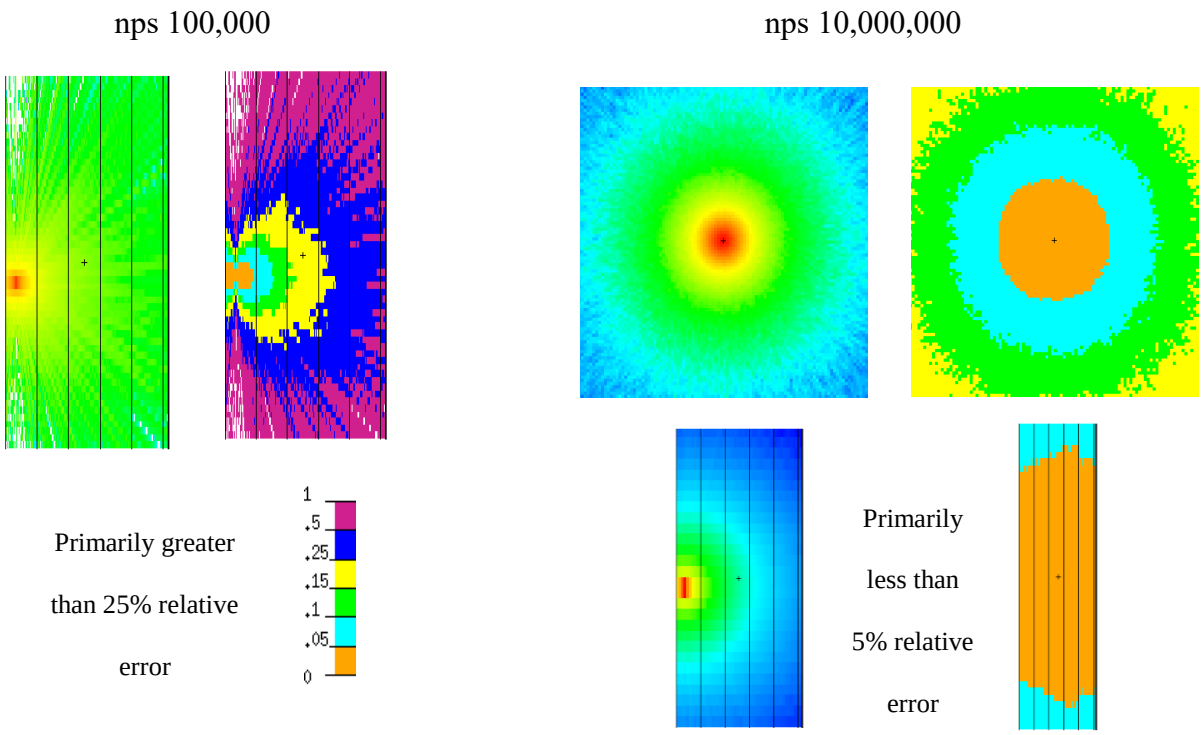

Figure 11. F4 mesh tally showing particle flux and associated relative error. Particle fluxes are shown with highest and lowest intensity indicated by red and blue, respectively. The relative error scale is shown (bottom left) ranging from 0 (0%) to 1 (100%).

2.2.2 AlSb Simulation Model

For reasons that will be discussed thoroughly in Chapter 4, the geometry for the AlSb structure is more complicated, making modeling of the AlSb detector slightly more challenging. In addition to the 5 micron thick AlSb layer, the structure design includes 0.1 microns of GaSb to provide strain relief between mismatched AlSb and GaAs lattices, a 300 micron thick GaAs substrate, another GaSb layer to prevent exposure of the AlSb to oxygen, and ohmic contact layers on each side. The structure is shown in Figure 12 (left), where layer thicknesses are not represented to scale.

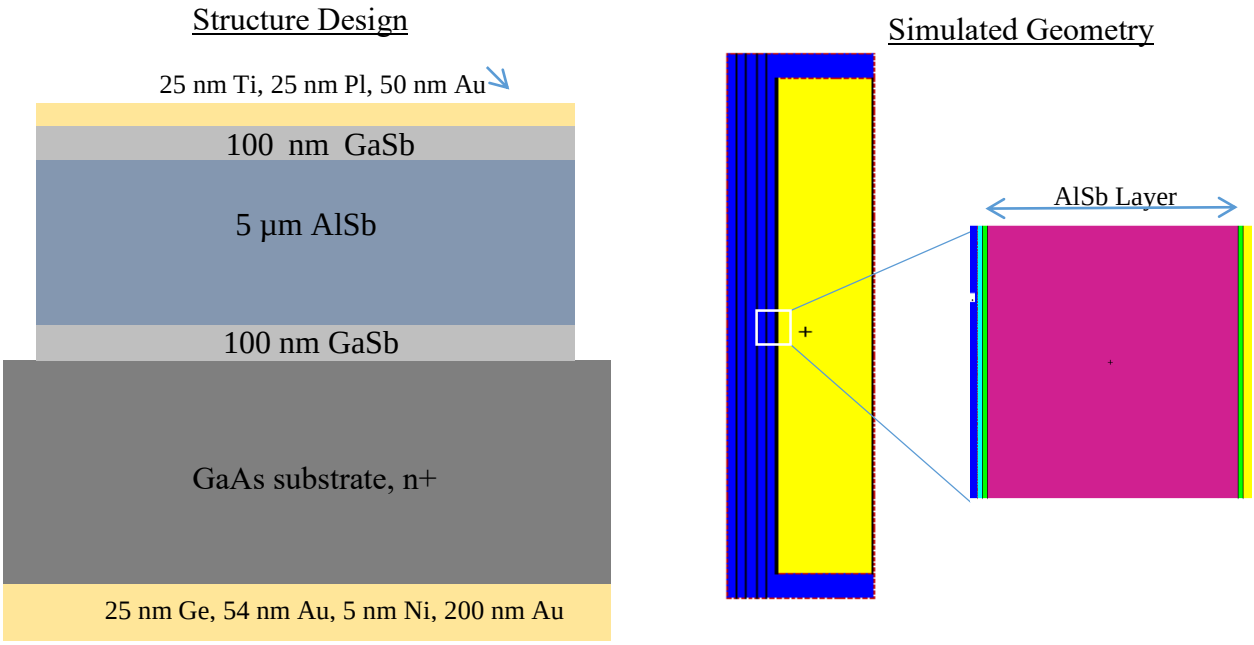

Figure 12. AlSb growth structure design (left) and MCNP5 simulation geometry (right).

To simplify things very slightly the ohmic contact layers were modeled using Au exclusively, neglecting the other elemental components but maintaining the overall layer

thickness. Geometry splitting was used as a variation reduction technique in the air region between the source and the detector surface. The simulated geometry, generated by MCNP5, for AlSb is shown in Figure 12 (right), where the scale is accurate. The dark blue region in this case depicts air and yellow is the GaAs substrate. The image on the far right shows the AlSb layer (purple) and the other nearby layers.

Again, a mesh was used to confirm that the number of particle histories tracked is statistically appropriate, illustrated in Figure 13. The images show the photon flux (top) and associated relative error (bottom) for side and top views of the AlSb detector for 100,000 and 10,000,000 particle histories. The black rectangular line in each side view represents the outermost detector structure boundary.

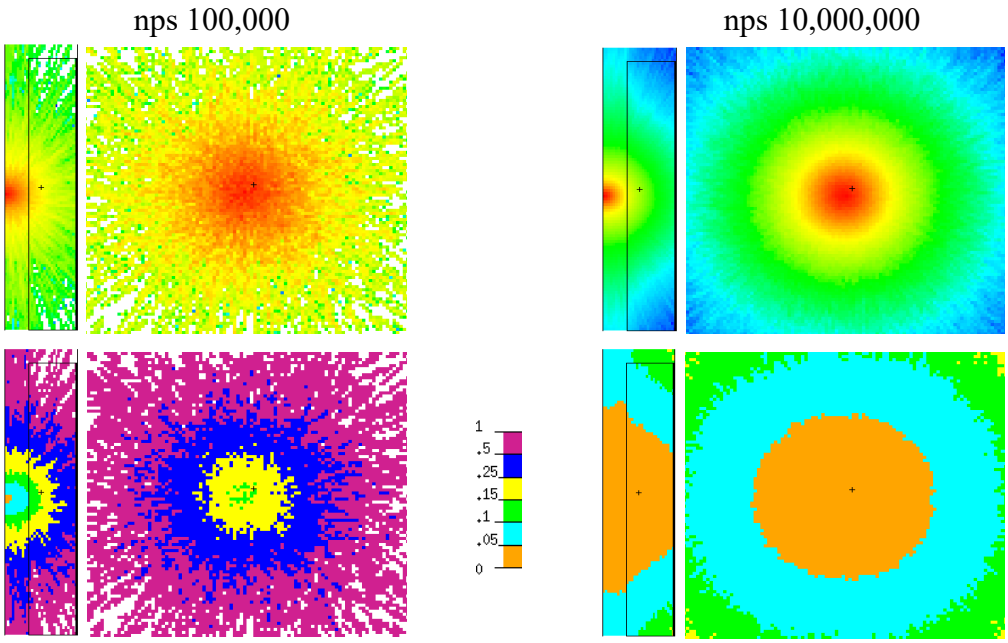

Figure 13. Photon flux and associated relative error for MCNP5 simulation of an AlSb detector, where each set of images shows the top and side views of the detector. The right

and left columns of images correspond to 100,000 and 10,000,000 simulated particle histories (nps), respectively. Particle fluxes (top row) are shown with highest and lowest intensity indicated by red and blue, respectively. On the bottom are the associated relative error results for each simulation. The relative error scale is shown (bottom center) ranging from 0 (0%) to 1 (100%).

2.2.3 Simulated Radiation Response

The SSB detector response was simulated using an F8 pulse height tally for modeling spectra from ^{57}Co and ^{133}Ba. An attempt was made to modify the spectra with the Gaussian energy broadening function in MCNP5. Because of the thin film nature of the material being modeled, the thick-target bremsstrahlung approximation was removed from the physics of the problem by setting IDES=1. All of the MCNP5 input files are included in Appendix A at the end of this document.

The SSB simulations were compared with measurements for benchmarking. These are compared graphically in Figure *14* (^{57}Co) and Figure 15 (^{133}Ba). The measurements were performed with ^{57}Co and ^{133}Ba sealed sources and a 50 micron thick SSB detector in a light tight metal box with an Ortec 142 preamp and Ortec 428 bias supply. Pulse height data were digitized using an Ortec Easy-MCA module. The linear, semi-log, and broadened plots on the left sides of Figure *14* and Figure 15 were produced using the MCNP plotter. On the right side, spectra from actual measured counts are shown.

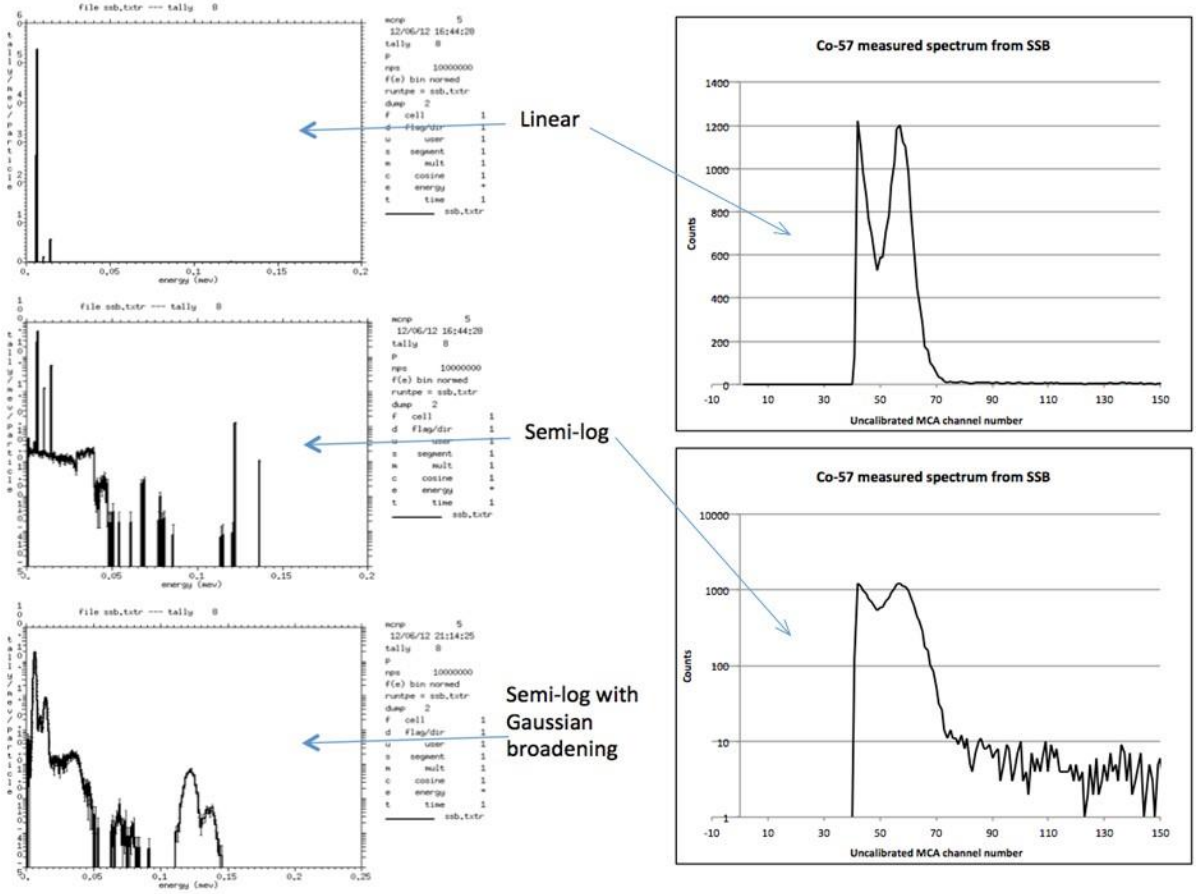

Figure 14. *Simulated (left) and measured (right)* ^{57}*Co spectra for SSB detector. The vertical axes for the simulated spectra represent the number of particles and the horizontal axes indicate the energy deposited in the detector in MeV. The features in the semi-log measured plot may correspond with features seen in the broadened simulated spectrum.*

The absence of measured data between channel numbers 0 and 45 was a deliberate low energy cut off, performed to isolate peak features in the spectrum from low pulse height electronic noise. Some features in the measured semi-log plots may correspond to features in the simulated semi-log Gaussian broadened plots.

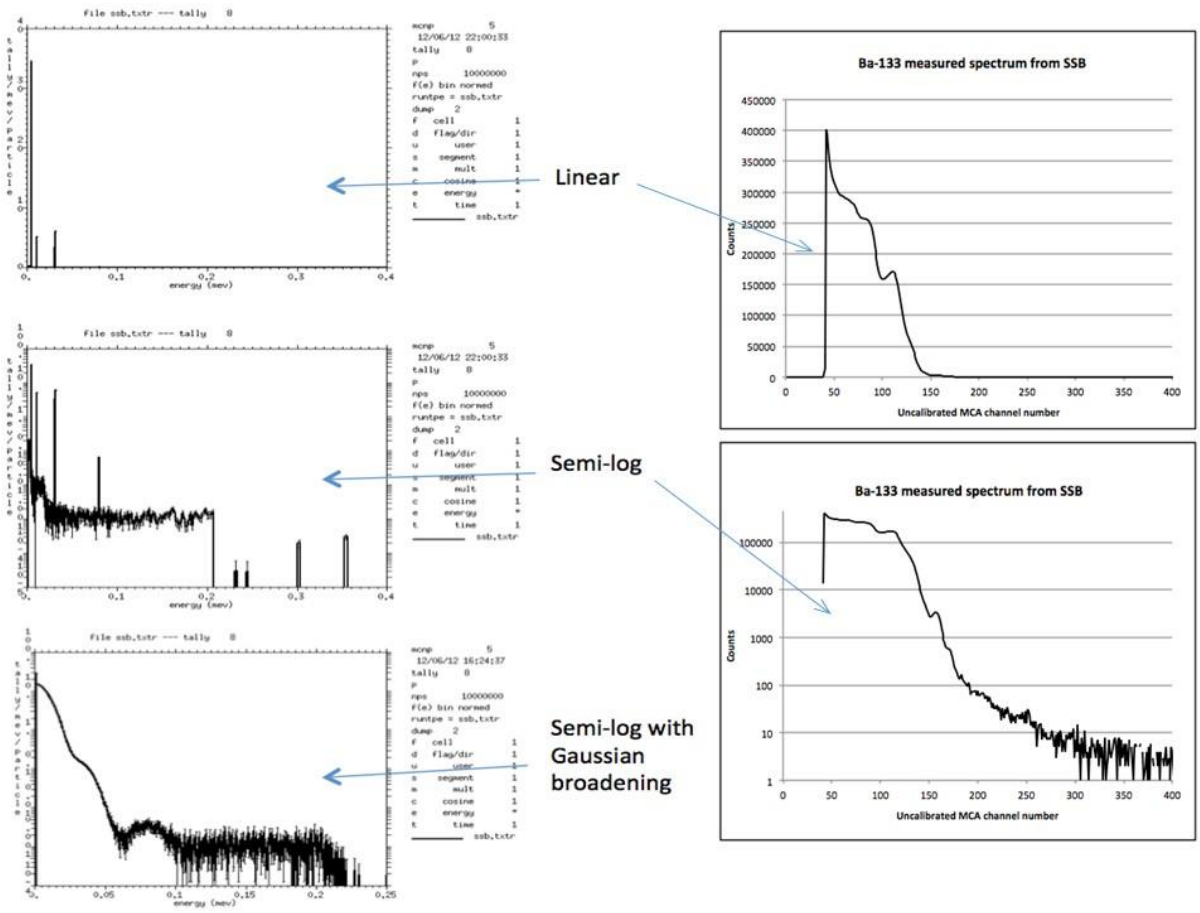

Figure 15. Simulated (left) and measured (right) ^{133}Ba spectra for SSB detector. The vertical axes for the simulated spectra represent the number of particles and the horizontal axes indicate the energy deposited in the detector in MeV. The features in the semi-log measured plot may correspond with features seen in the broadened simulated spectrum.

MCNP5 requires three known FWHMs to calculate the values used by the Gaussian energy broadening (GEB) function to modify the simulated spectra [33]. The measured spectra from the SSB detector did not generate resolution sufficient to calibrate the MCA. Therefore, a FWHM was not measured and could not assist in simulating peak broadening. Instead, an iterative series of reasonable guesses was made to produce the broadened

spectra shown.

Figure 16 (^{57}Co) and Figure 17 (^{133}Ba) portray the simulated spectra (without broadening) for the AlSb detector on the left, compared to the SSB detector on the right.

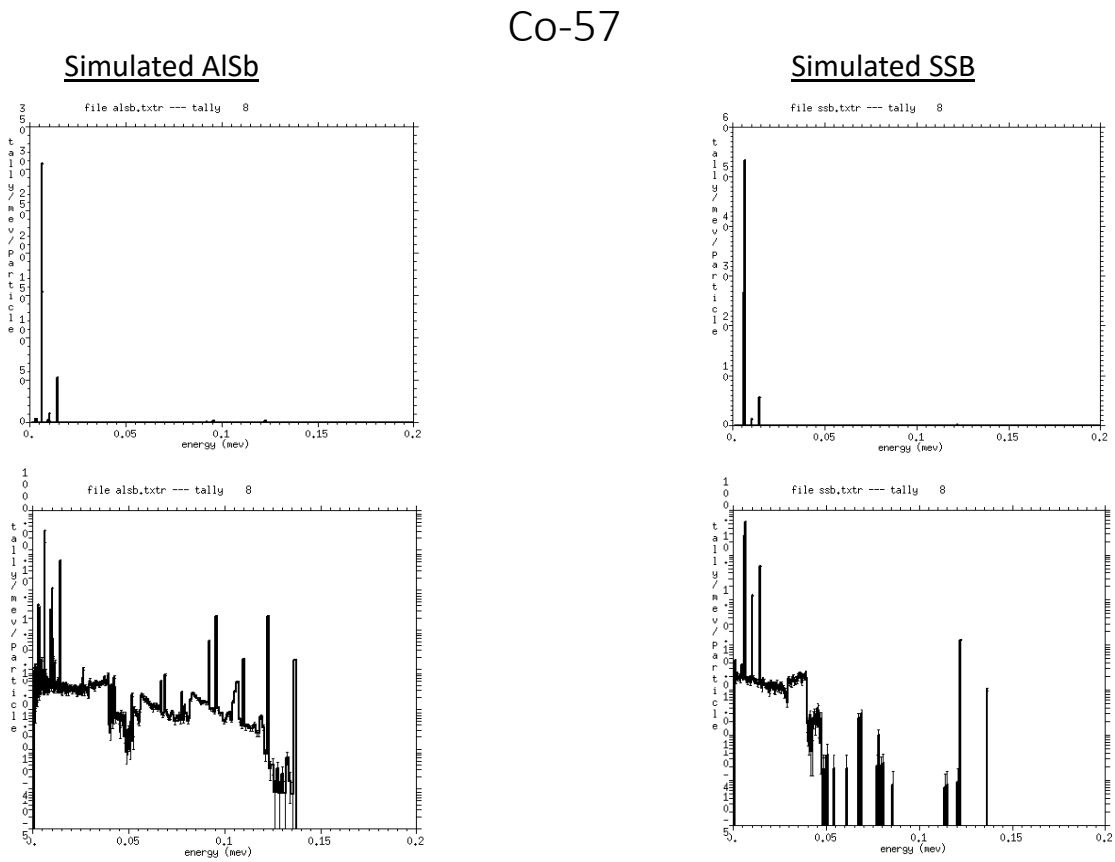

Figure 16. Simulated linear (top) and semi-log (bottom) spectra for AlSb (left) compared to SSB (right) for ^{57}Co. Horizontal axes represent particle energy in MeV and vertical axes indicate the number of particles.

For ^{57}Co the number of simulated counts in the highest energy peak, $E_{x\text{-}ray}$=6.4 keV, was 310 for AlSb and 54 for SSB, as seen in Figure 16. In the case of ^{133}Ba, shown in Figure 17, the photon count was 310 and 34 for AlSb and SSB, respectively, for the highest

peak associated with x-rays having energy equal to about 4.4 keV. The semi-log simulated plots for both radioisotopes reveal improved details and structure with AlSb when compared to SSB. Simulated AlSb spectra include more counts overall, with about 10 times more photons being detected across the energy spectrum, and much higher efficiency at higher energies for these thin films, even with a thinner AlSb than SSB. This apparent improved detection efficiency can be attributed to the higher atomic number of AlSb (Z_{Sb} = 51) compared to Si (Z = 14).

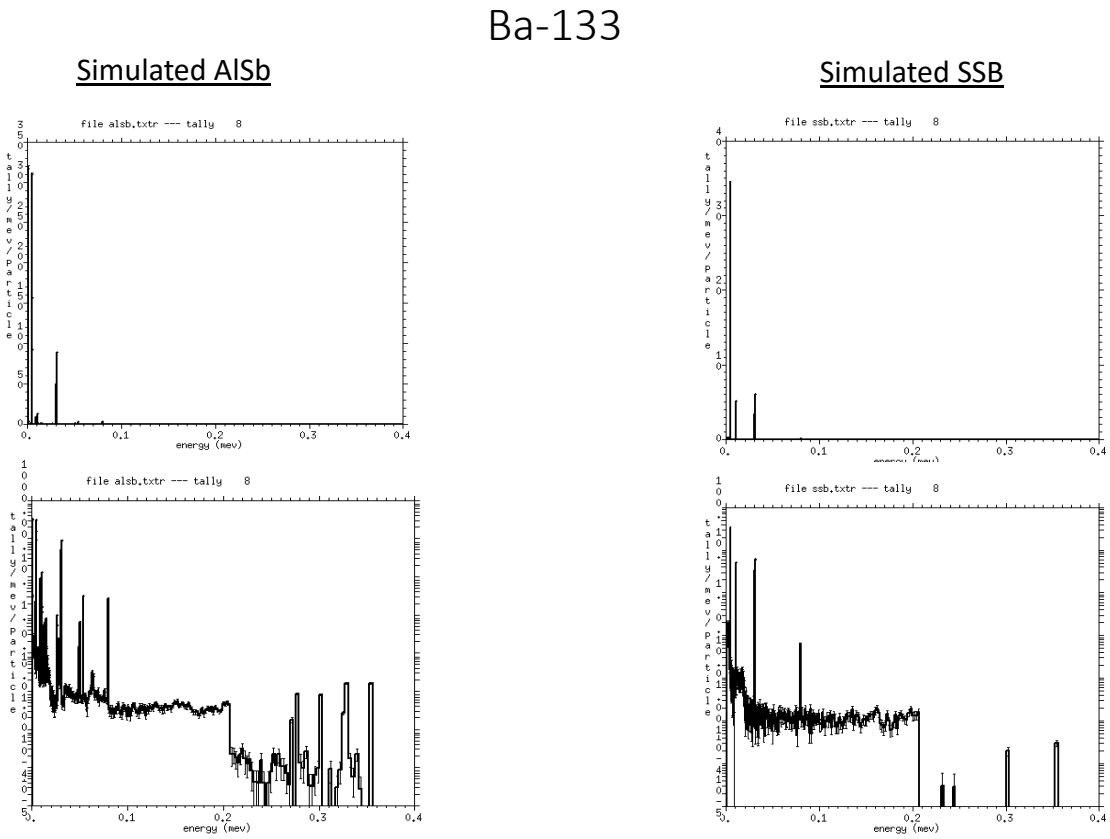

Figure 17. Simulated linear (top) and semi-log (bottom) spectra for AlSb (left) compared to SSB (right) for ^{133}Ba. Horizontal axes represent particle energy in MeV and vertical axes indicate the number of particles.

Geometry splitting is not a recommended method of variance reduction for F8 tallies [33]. Instead, the weight windows method is suggested for most accurate results, although use of the weight windows generator is discouraged. Modifying the variance reduction technique could be addressed in future work.

In spite of difficulties involving variance reduction and GEB functions, simulated spectra were generated with features comparable to measured SSB spectra for both ^{57}Co and ^{133}Ba. Based on this observation, the simulated AlSb spectra suggest that more photons overall should be detected with thin film AlSb, and that known energy peaks should be identifiable.

Chapter 3

Proof of Concept: MBE Diode Radiation Detectors

3.1 GaSb PN Diode Detectors

Although this research was focused on MBE grown AlSb radiation detectors, simple GaSb P-N junctions were examined for their detector performance. GaSb does not oxidize and high-quality n-GaSb substrates are readily available, allowing for a homo-epitaxial structure without lattice-mismatch induced strain. In their studies on epitaxial Sb structures, Bennett and Shanabrook [27] report no evidence of spiral growth (indicative of strain) on such structures, although they did observe concentric ring shaped mounding, which they attribute to imperfections on the substrate surface. GaSb is theoretically easier to grow than AlSb, so this diode work was seen as a preliminary test before moving forward with AlSb diode work.

This study on GaSb was published in the Journal of Electronic Materials [34].

3.1.1 Sample Fabrication

GaSb PN junctions were fabricated by two methods: by solid-source molecular beam epitaxy (MBE) on n-GaSb substrates, and by Be ion implantation into n-GaSb substrates.

For the epitaxial structure (Figure 18), a 500 nm thick p-type GaSb layer was grown directly on an n-type GaSb substrate, producing a sharp boundary between p-type and n-type regions. Beryllium was used as the p-type dopant with a dopant-atom concentration of 5×10^{18} cm^{-3}.

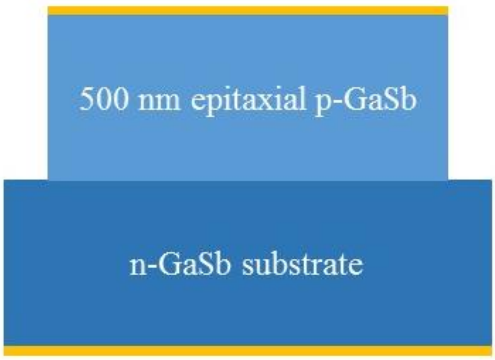

Figure 18. Epitaxial GaSb detector structure.

For the implanted diode structure (Figure 19), two sequential Be implantation processes on the same n-GaSb substrate were designed using SRIM software [35]. The first, thinner region was designed as the contact layer and contains higher p-doping (1×10^{19} cm^{-3}). The simulated Be ion fluence and energy were 1×10^{14} cm^{-2} and 10 keV, respectively. The second region, which was designed to perform as an emitter, is thicker than the first

implantation layer and has slightly lower doping to provide a sufficient carrier concentration. To satisfy this requirement, the implanted ions in the second section had to penetrate deeper into the substrate. Considering these parameters, the simulated areal dopant density for the desired doping was calculated to be 5.7×10^{13} cm^{-2} with a Be ion energy of 60 keV. Following these calculations, the expected p-doping at the PN junction was 1×10^{18} cm^{-3} at a depth of 200 nm, assuming 50% activation [36], and with a more gradual interface between p- and n-type regions than in the epitaxial samples.

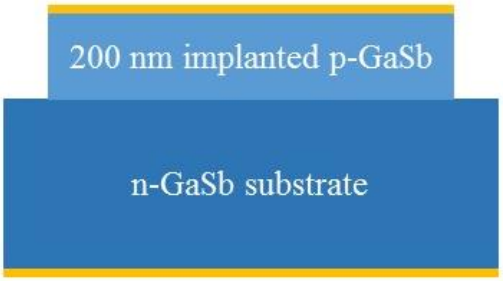

Figure 19. Implanted GaSb detector structure.

3.1.2 Radiation Response

Prior to radiation measurements, electrically isolated devices of different surface areas were produced during processing for both types of structures. This involved the application of low resistance ohmic metallization [37] to the top and bottom surfaces of the diode structures that the radiation readily penetrates. Samples fabricated by both methods produced devices with similar doping profiles. The devices varied in surface area from 500×500 μm^2 to 2×2 mm^2. Figure 20 indicates the epitaxial devices 1-10 and implanted

devices 1-4, all with contact patterns of the same surface area, 2×2 mm^2. Smaller area epitaxial device contacts are not numbered but are located to the right of the numbered devices on the image. The microprobe tips for measuring signals are shown also for reference.

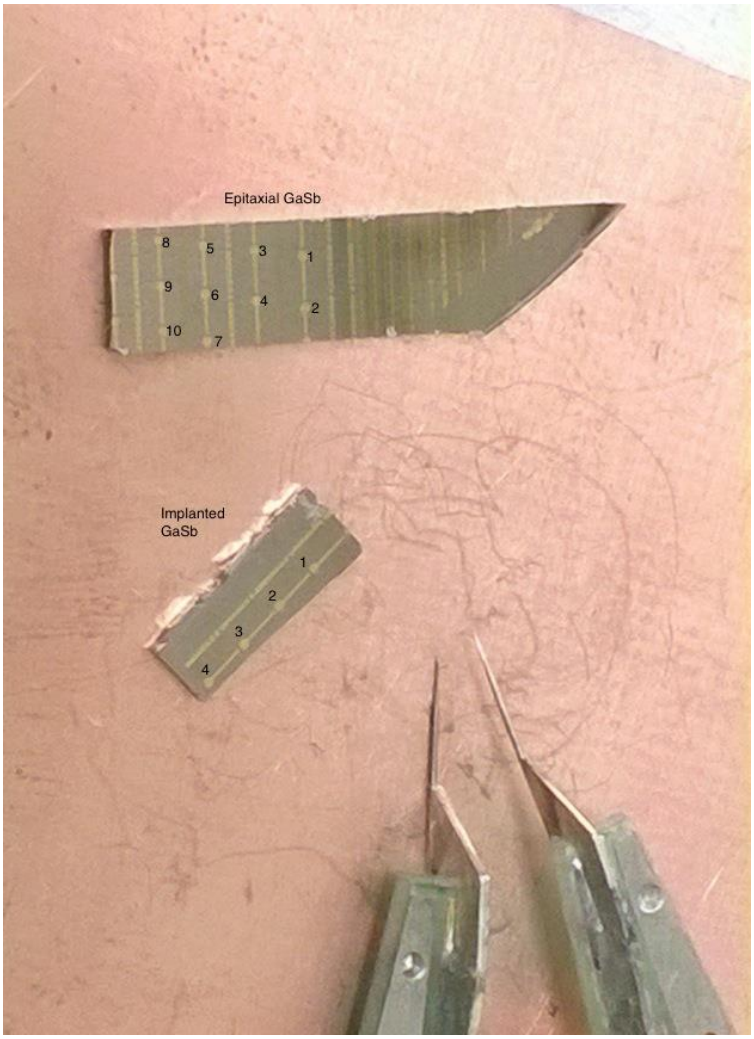

Figure 20. GaSb diodes shown with microprobe tips for reference. The set of epitaxial devices are numbered 1-10 on the top sample, whereas the bottom sample has implanted devices 1-4 numbered.

To test radiation response, each GaSb diode device was placed with the n-type metalized substrate in contact with a copper plate. A probe tip was placed on the p-type metalized GaSb surface to read out signal and to apply a bias from an Ortec 428 HV power supply, though zero applied bias was used in the analysis presented. The probe station was placed inside a RF shielding enclosure to reduce noise. The signal was fed into an Ortec 142 charge-sensitive preamplifier, which was then amplified by an Ortec 570 shaping amplifier. The amplified pulses were digitized by an Ortec EasyMCA multichannel analyzer, which linearly converts electronic pulse heights to channels to produce histogram spectra. The pulse heights depend on the energy deposited in the active region of the device and the particular response of each device. The charged particle radiation sources used were ^{241}Am and ^{252}Cf, with activities of 1.9 kBq and 40.4 kBq, respectively, though the Am source was partially blocked by the source geometry, reducing the effective activity. During measurements, the sources were placed 8 mm above the p-GaSb surface to provide alpha-particle and fission-fragment irradiation at known energies, and to minimize angular divergence from the small point sources. This charged particle radiation has a high linear energy transfer and a short stopping distance in the material, though calculations showed that only a fraction of the energy was deposited in the thin active detection region, and that this fraction is much smaller for alpha particles than for fission fragments. For direct comparison, a series of measurements was performed using different devices of the same size for each of the fabrication structures.

Figure 21 shows spectra obtained from 10-minute ^{252}Cf exposures using four different 2×2 mm^2 implanted GaSb devices. The horizontal axis of these event histograms

corresponds to the voltage pulse height observed at the electrodes, and is proportional to the energy deposited in the active region of the detector material. The lowest energy peak, best observed in Figure 21(d) near channel 70, is associated with the alpha emitted from ^{252}Cf with 6.1 MeV incident energy. The binary fission-fragments from ^{252}Cf have distinct energy distributions, centered near 80 and 100 MeV for the heavy and light fragments, respectively. Both fragment peaks can be seen in all of the energy spectra in Figure 21. For the 2×2 mm^2 implanted devices the average position of the centroid of the light fission-fragment peak is channel number 680 with a standard deviation of 190, or 28%, due to the large variation in response. The high count rate on the left side of each plot is due to low pulse height events caused by background noise (electronic noise, leakage current, etc.) and is not a true radiation response. While the alpha peak is resolved from noise in the samples in Figure 21(a, c, d), it is not in the sample in Figure 21(b). As only a fraction of the alpha-particle's kinetic energy is deposited as it penetrates the very thin active region, this may be remedied with larger depletion widths.

For the implanted GaSb diodes, there is a large variation in peak position for measurements taken using different devices of the same size, which does not correspond to any obvious variation in device characteristics. This is suggestive of a non-uniform P-N junction and thus a different thickness of the active region produced during the ion implantation process. This leads to different amounts of energy being deposited in the active region, different numbers of electrons liberated in this region, and a variation of the pulse height observed. This is confirmed in the cross-sectional transmission electron microscope (XTEM) image in Figure 22(b), where implantation damage zones are shown

to be unevenly distributed throughout the Be ion penetration depth.

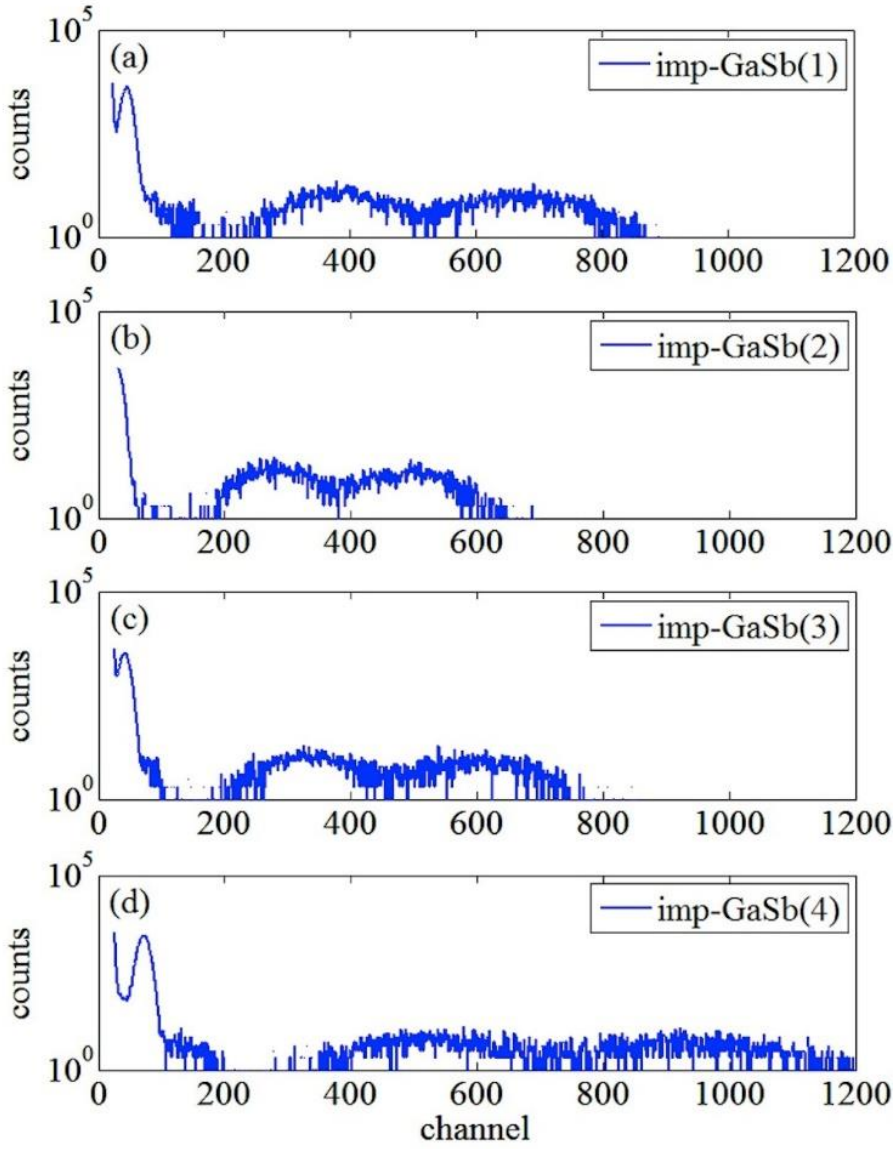

Figure 21. Measurements of ^{252}Cf radiation with different devices of the implanted GaSb diode. Counts are in log scale. Plots (a) through (d) represent 2×2 mm^2 devices. Measurements were taken with the source placed 8 mm directly above the relevant device. Charged particle detection response is non-uniform across different implanted devices of the same size.

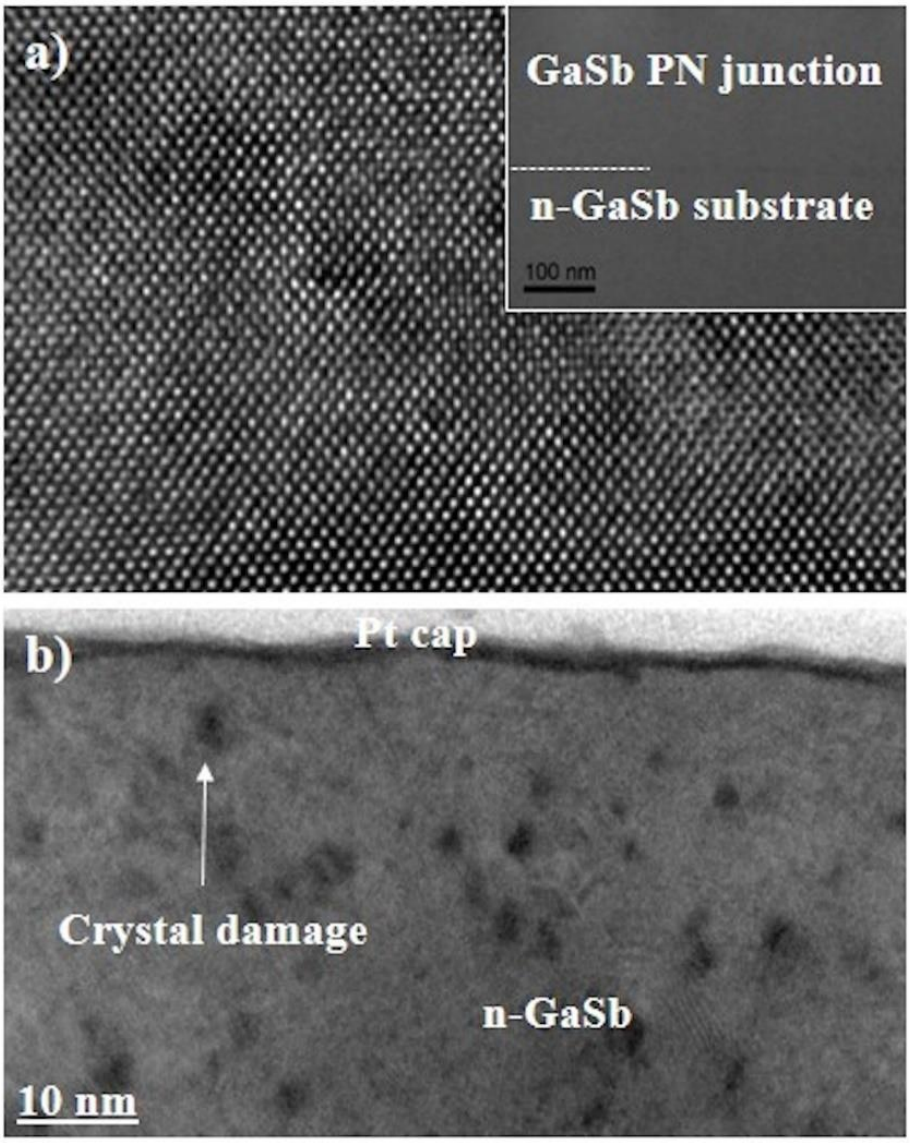

Figure 22. a) XTEM image (inset) of MBE grown epitaxial GaSb PN diode with high quality crystal structure and a HR-XTEM image of the diode showing the GaSb atomic structure on the 110 plane. b) XTEM image of Be implanted in n-GaSb showing a variety of implantation induced crystal damage.

A similar set of 10-minute measurements was conducted to determine the radiation detector response from the epitaxially produced GaSb structure. Nine devices (epitaxial numbers 1-9 in Figure 20) were used to measure the ^{252}Cf spectra shown in Figure 23, with a single device presented in Figure 23(a) for clarity. The different devices responded very similarly to the same radiation for this diode structure, as seen in an overlap of spectra from eight 2×2 mm^2 devices in Figure 23(b). While the alpha peaks are more difficult to resolve from the baseline noise, the fission-fragment peaks are remarkably lined up for the same sized devices measured. While the average position of the centroid of the light fission-fragment peak is lower than that of the implanted devices, channel 155, the standard deviation is only 12 channels, or 8%, for the 2×2 mm^2 epitaxial devices.

This result suggests a much more uniform depletion region and thus a much more uniform and well-defined junction across the material grown by epitaxial methods. The XTEM in Figure 22(a) illustrates the superior material quality and lattice uniformity across the growth boundary. Device 7 was smaller due to cleaving, and the spectrum, shown in Figure 23(c), has a higher pulse height response for the same incident particle energies.

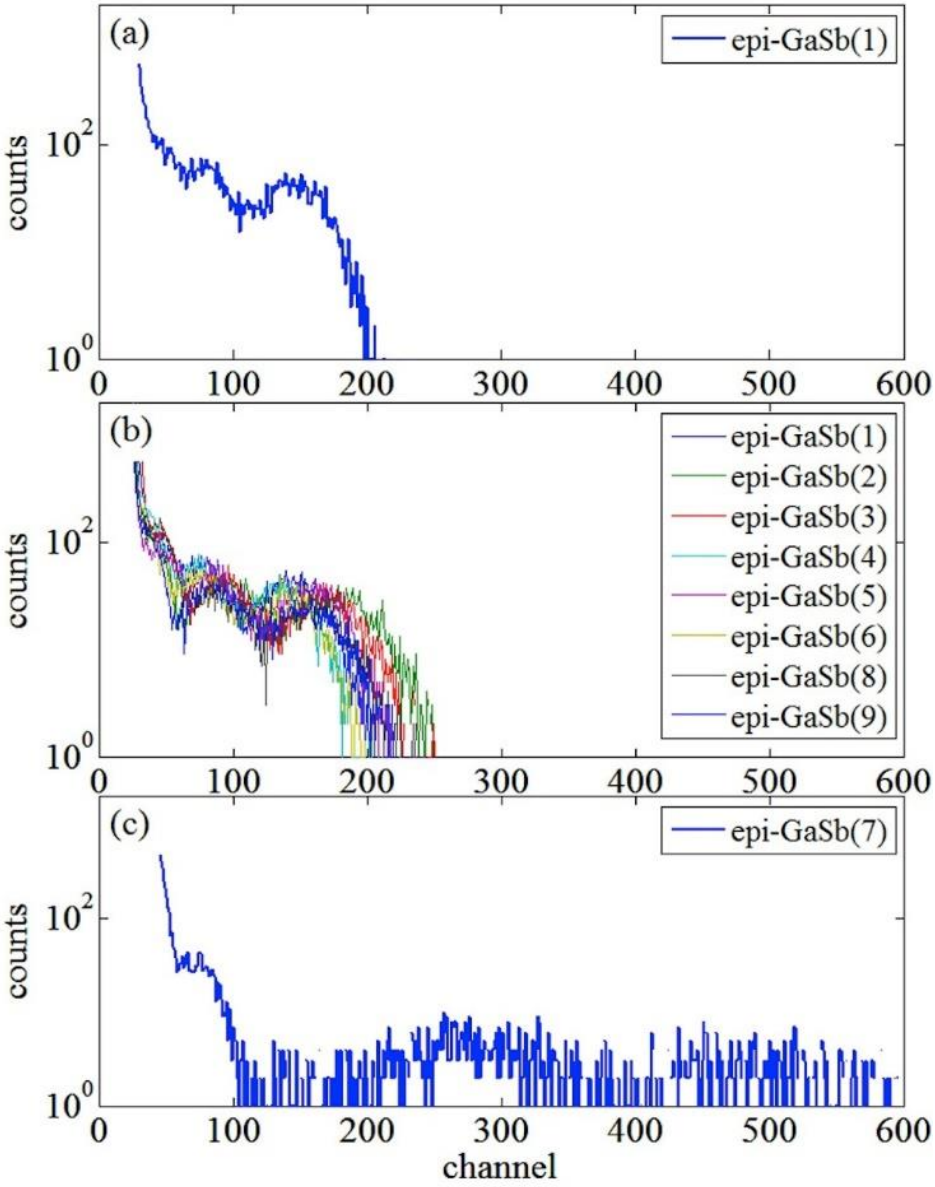

Figure 23. Measurements of charged particle radiation from ^{252}Cf with different devices of the epitaxial GaSb diode material. Counts are in log scale. (a) Only device 1 for clarity; (b) Devices 1-6, 8, 9; (c) Device 7. All devices except 7 are 2×2 mm^2. Device number 7 has reduced surface area due to cleaving. The radiation response is very consistent for epitaxially produced GaSb devices of the same area.

Despite the epitaxial and implanted materials being very similar in composition and doping density, and using identical readout electronics and settings, the detector responses are clearly different. The depletion widths were calculated to be 25 and 26 nm for the epitaxial and implanted structures, respectively, assuming an abrupt junction in each case. This is a reasonable assumption when considering epitaxially grown materials, as the doping can be controlled precisely between layers. Highly uniform detector response was seen with epitaxial devices of the same surface area. In the case of diodes fabricated by ion-implantation, the doping density is a maximum at the average penetration depth for the incident ion energy, with some ions implanted nearer to or farther from the incident surface. Damage zones within the implanted material may have also contributed to the variation in detector response observed with ion-implanted devices of the same size. The implanted GaSb devices have a better signal-to-noise ratio, seen by the separation of the alpha peak from the baseline noise, while the epitaxially grown devices have a much more a uniform response.

The smaller epitaxial device, number 7, had an improved signal-to-noise response, with the alpha peak separated from the noise, and the fission-fragment peaks spread out past channel 600. To further examine the effects of reduced device size, additional measurements were taken with the epitaxial GaSb samples and the ^{241}Am alpha-particle source. The amplifier gain was lowered and measurements were taken for 100 minutes each for three small devices, with results in Figure 24. These devices were significantly smaller than the ones used for Figure 23, ranging from 500×500 μm^2 to 900×900 μm^2, and results demonstrate the detector behavior for different device surface areas.

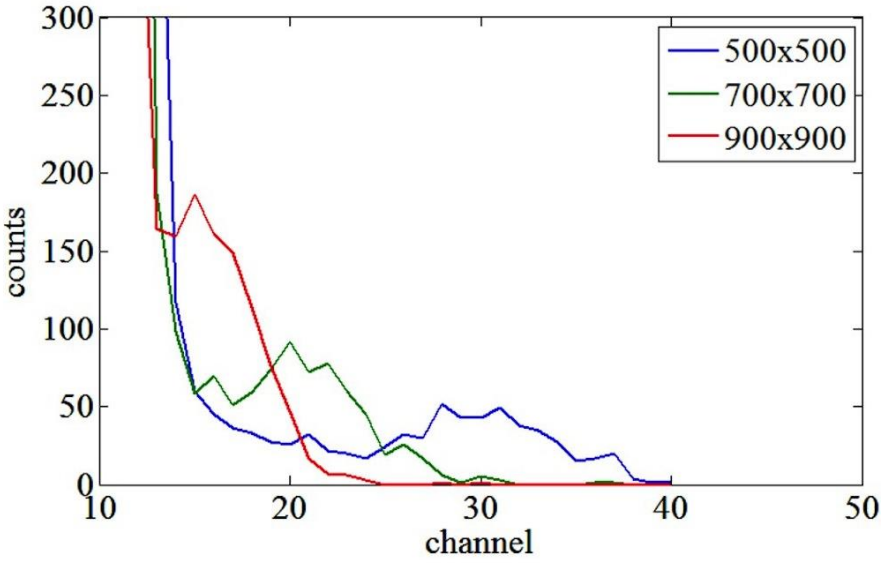

Figure 24. Measurements of ^{241}Am with different device areas, ranging from 500×500 μm^2 to 900×900 μm^2, using epitaxial GaSb diodes. The alpha peak shifts up and away from low channel background noise and the counting efficiency decreases as the device size is reduced.

As seen in Figure 24, the energy deposited from 5.5-MeV alpha-particles from ^{241}Am is in a higher channel and is most separated from the background noise for the smallest device, while it is lower and least separated for the largest device. The energy resolution improved with the epitaxial GaSb device size decrease, with 46%, 36% and 26% for 900×900 μm^2, 700×700 μm^2, and 500×500 μm^2, respectively, for these thin films with only partial alpha energy deposition. Voltage-capacitance relationships for PN junctions dictate that the diode capacitance increases as the cross sectional area of the junction [38] and the pulse height is inversely proportional to the capacitance [7], seen in other work [39, 40].

Similar behavior was also noted by Klann and McGregor [40], where they observed lower noise and cleaner signals for smaller area GaAs detectors. Decreasing the total capacitance by widening the depletion region would allow for larger detector surface areas while producing sufficiently large pulses. Alternatively, small area detectors could be joined in series to achieve a balance between pulse height and detection efficiency, as has been suggested by Steinberg [39]. With improved signal-to-noise and energy resolution, X-ray and gamma-ray spectroscopy applications may become feasible.

In this study, my collaborators and I have demonstrated charged particle radiation detection by use of GaSb diodes fabricated by both ion implantation and epitaxial growth, with identifiable peaks in the spectrum from alpha particles and fission fragments. A consistent detector response is obtained from MBE-grown antimonide diodes whereas more variation is observed for similarly sized Be ion-implanted devices. The signal pulse height, and thus the signal-to-noise ratio, is improved when device size is reduced; this can be attributed to a decrease in the diode depletion capacitance. A disadvantage of reduced device surface area is reduced geometric detection efficiency. Because GaSb has not previously been considered for detection of radiation, much scope for improvement is possible. Increasing the detector depletion width to enable full energy deposition would improve energy resolution and overall detection performance.

3.2 AlSb PIN Diode Detectors

Following successful measurement of heavy charged particles with simple homoepitaxial GaSb diodes, AlSb P-I-N structures were grown and characterized for their radiation response. Bennet and Shanabrook [27] report a much smoother surface for AlSb growth on GaAs substrates than with GaSb epilayers on GaAs. Because of the larger band gap of AlSb, compared to GaSb, reduced thermal noise was expected.

Results of this study were published in the proceedings of the IEEE Nuclear Science Symposium and Medical Imaging Conference and the Journal of Electronic Materials [41, 42].

3.2.1 Structure & Fabrication Techniques

Heterostructures composed of GaAs, GaSb and AlSb were grown using a twin VG V80 MBE reactor with valved As and Sb crackers and VEECO's SUMO^{TM} effusion cells for In, Ga and Al. The Al and Sb used for this work has 7N purity. Processed and cleaved samples of the AlSb devices fabricated for this study are shown in Figure 25.

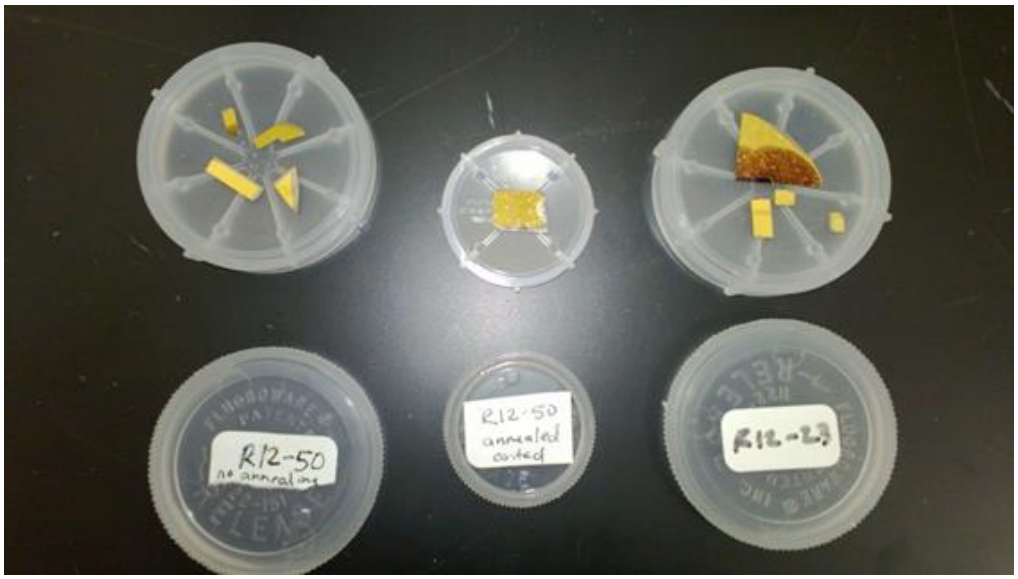

Figure 25. Metalized AlSb diode samples R12-23 and R12-50.

As the goal of this project was to analyze MBE grown AlSb for radiation detection, the primary growth structure was a p-type/insulator/n-type (P-I-N) diode, as shown in Figure 26. Undoped AlSb was grown to 5 µm thick on a commercially obtained n-type GaAs substrate, with 10 nm of p-type GaSb doped with Be atoms as an oxygen protective capping layer to prevent the AlSb from oxidization. Structures R12-23 and R12-50 were grown under identical conditions, although on different days. Prior to the application of ohmic contacts to the R12-50 diode, it was cleaved into two pieces and one was annealed. The structures were then further cleaved to produce samples of various dimensions.

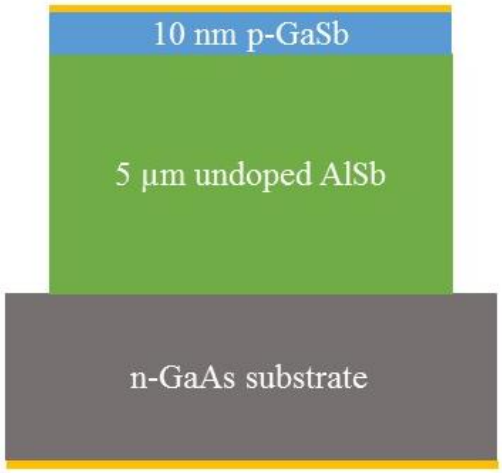

Figure 26. R12-23 and R12-50 AlSb structure used for all characterization excluding Hall measurements.

The simple structure (Figure 27) was necessary for Hall measurements, as the substrate and capping layers needed to be non-conductive for characterization of the AlSb layer.

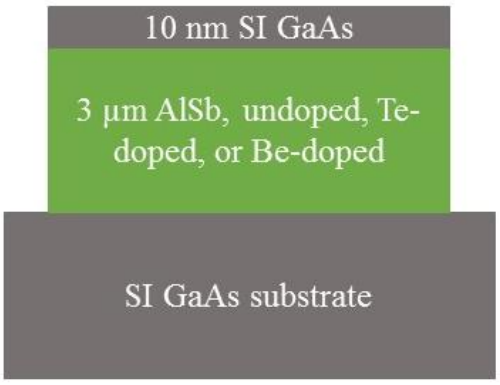

Figure 27. R14-145, R14-171, R14-172, R14-175, R14-176, R14-177, R14-178, R15-34; AlSb structure used for Hall measurements.

3.2.2 Characterization

3.2.2.1 Surface Quality

All surface measurements were performed using diode structures R12-23 and R12-50, illustrated in Figure 26, prior to the application of ohmic contact layers. The surface was found to contain some defects, as was expected for heteroepitaxial growth.

Nomarski imaging provides nondestructive topographical information on a microscopic scale by taking advantage of the interference contrast of two images of the same surface area. Height differences are measured using the gradient of the refractive index and an image is produced that accentuates edges and boundaries on the surface [30]. Different levels of magnification can be used to examine surface characteristics over a wide range of dimensions. The following images in Figure 28 and Figure 29 depict features observed at different levels of magnification for R12-50 and R12-23, respectively.

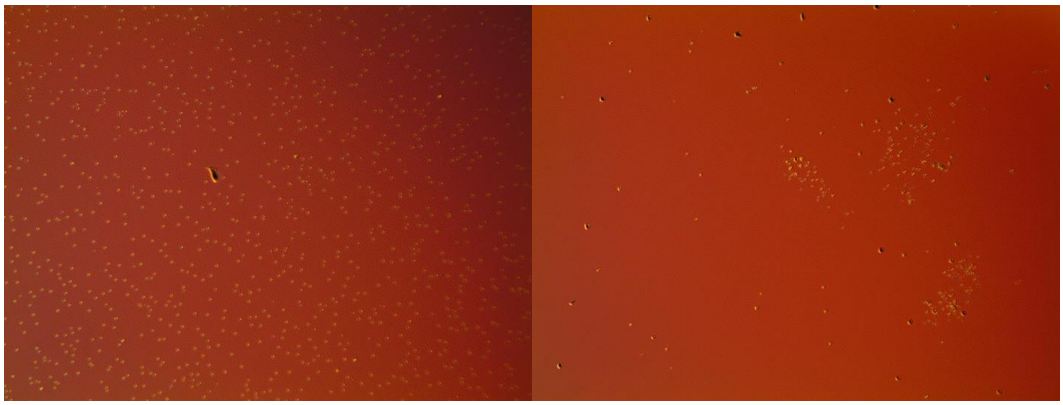

10×

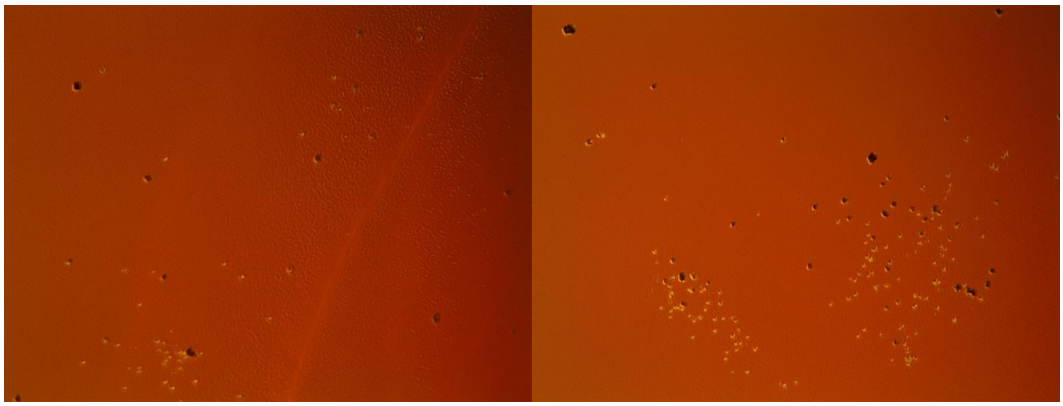

20×

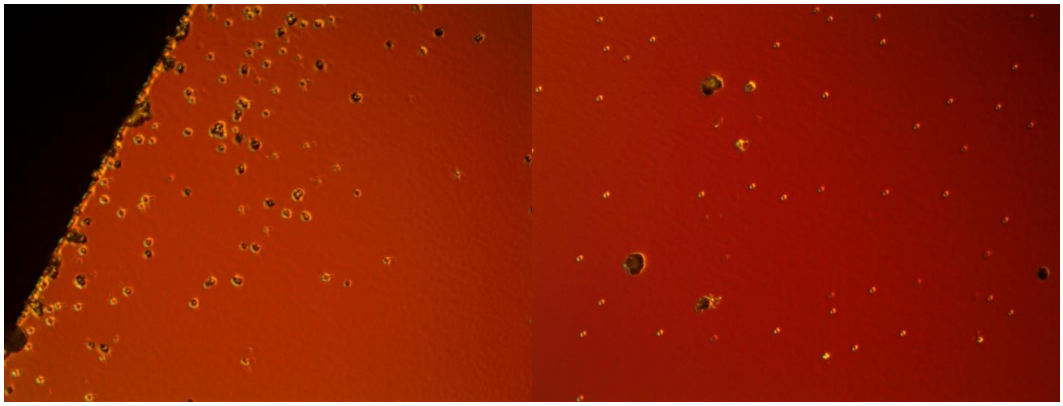

50×

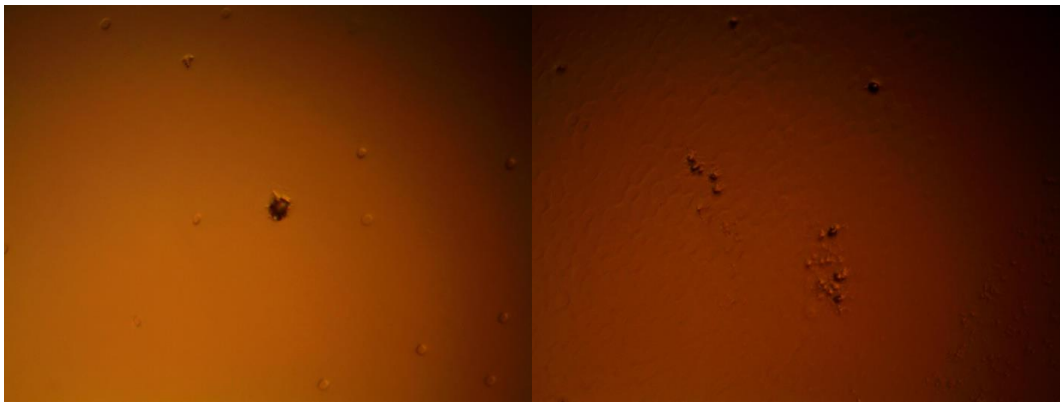

100×

Figure 28. Nomarski images of sample R12-50 at 10, 20, 50 and 100 times magnification.

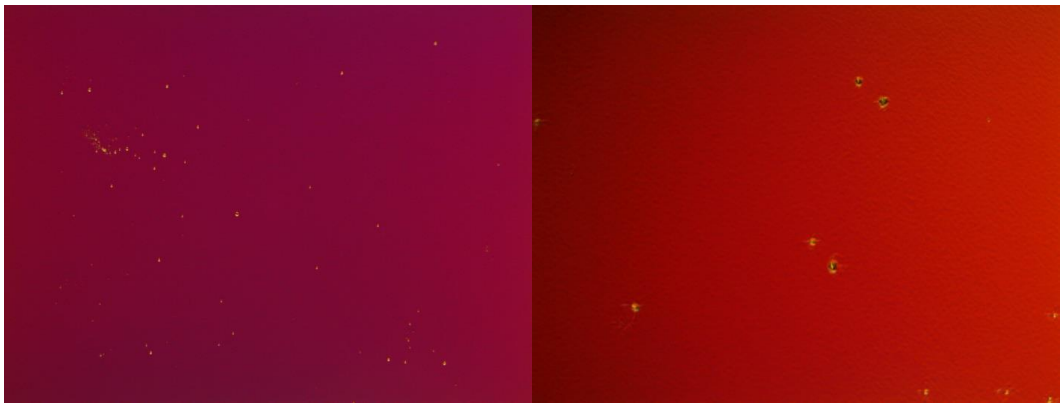

10× 50×

Figure 29. Nomarski images of sample R12-23 at 10 and 50 times magnification.

The circular pits on each optical image are crystal surface defects, more concentrated near the edge, which are expected when growth is non-homogeneous. However, these pits may contribute to electrical shorting through the material when a bias is applied. The "orange peel" texture, normal during antimony growth on arsenides, is representative of a roughened surface appearance due to wrinkle-like defects. A comparison between the two samples for 10× and 50× magnification reveals a higher defect density on the surface for R12-50, which suggests that it is more likely to have electrical shunting issues.

Atomic force microscopy (AFM) also provides surface data. The digital images are produced by measuring the small, but constant, force of a diamond tip as it scans across the material surface being examined [30]. AFM measurement results for sample R12-50 are shown in Figure 30.

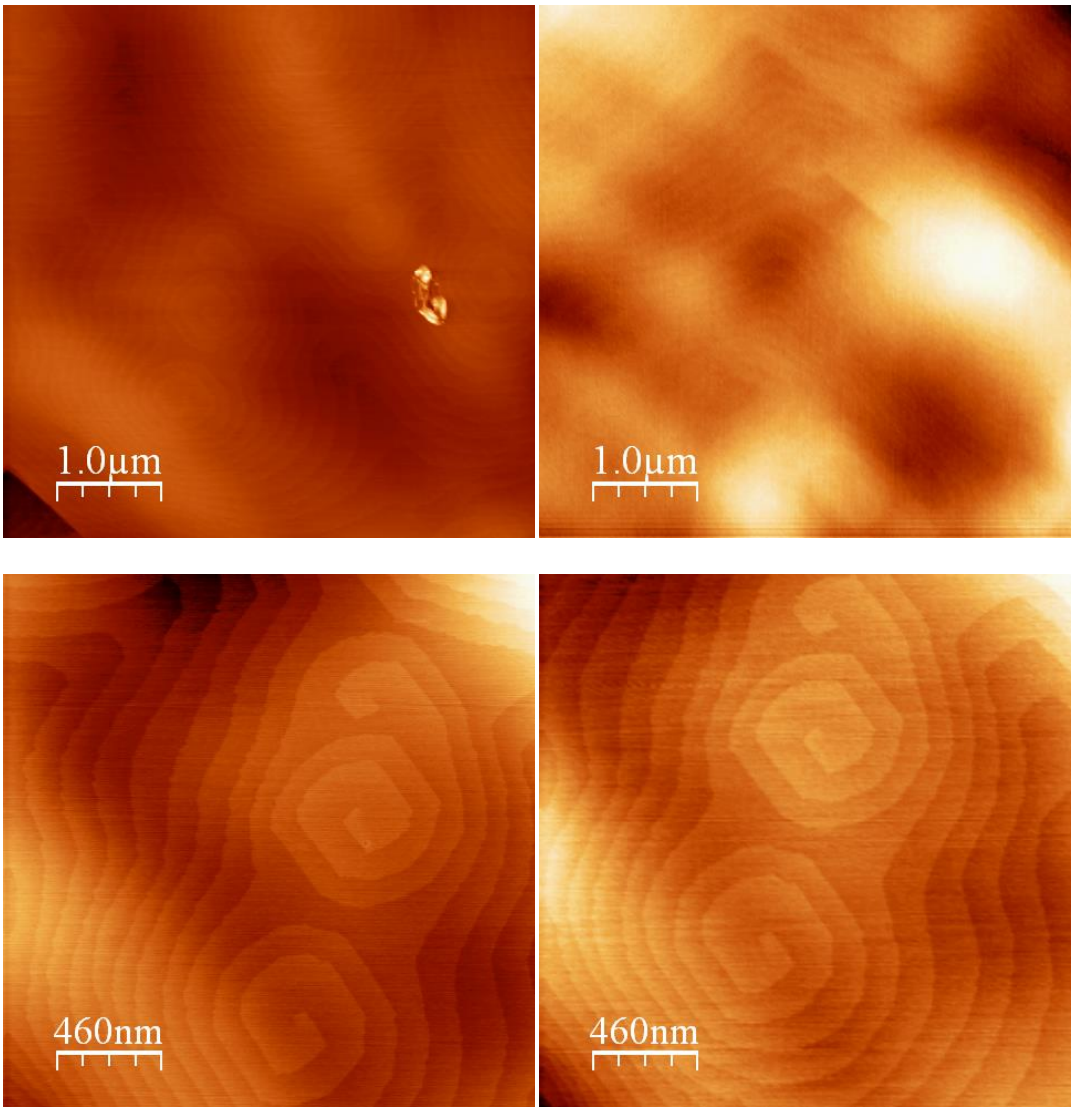

Figure 30. Atomic Force Microscopy images for sample R12-50.

Screw dislocations are a result of shear strain between lattice-mismatched layers. To relieve stress, the atomic layers begin to shift by one atom in a spiral staircase fashion, as is illustrated in Figure 31 below [30]. The spiral features on the AFM images in Figure 30 indicate the existence of screw dislocations, which is common (but not desirable) for

heteroepitaxial growth structures, especially those involving antimonides and arsenides. The AFM images confirm that the AlSb growth is typical and there are no issues.

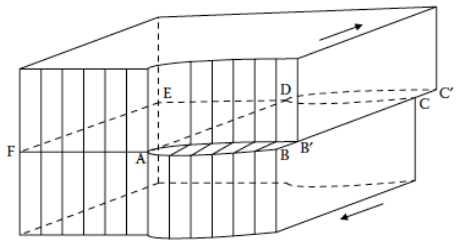

Figure 31. Screw dislocation [30].

3.2.2.2 Lattice Quality

Material composition measurements were also performed to evaluate the lattice quality using the diode structures R12-23 and R12-50 prior to the final processing step of applying ohmic contacts, and one of the undoped Hall structures, R12-145.

Bragg scattering is used to evaluate the regularity of the crystal lattice. With a perfect lattice, the scattering maxima follow the Bragg scattering equation, $n\lambda = 2d\sin\theta$. An x-ray beam of wavelength λ is scattered off of the surface of a crystal at an angle θ and the reflected beam is measured. The distance between atomic layers in the crystal (lattice constant) is d, and n is an integer. Bragg's law describes the difference in path length for scattering of x-rays with atoms of different crystal lattices, shown in the diagram in Figure 32.

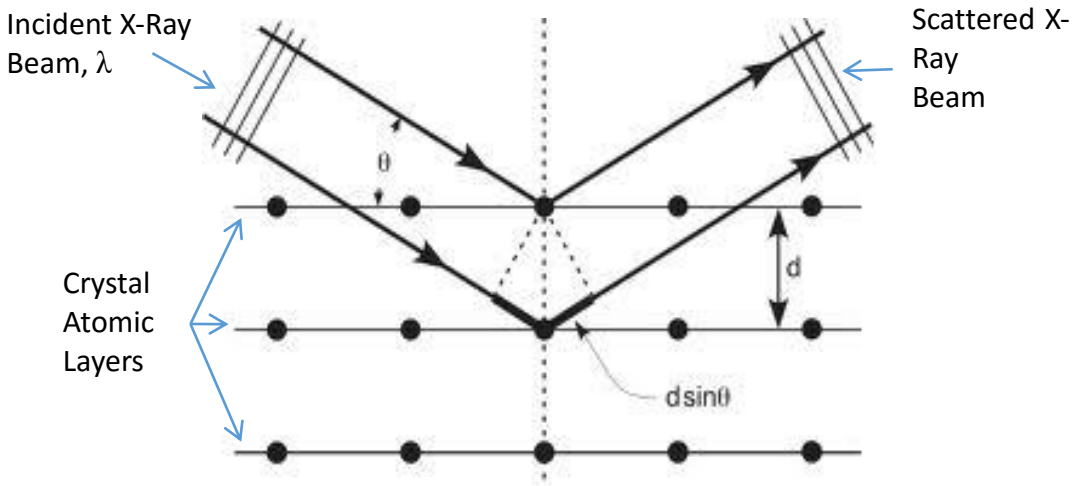

Figure 32. Bragg scattering, nλ=2dsinθ.

For imperfect crystals, the distance between lattice points, the lattice constant, will vary, resulting in broadened reflection maxima. The XRD characterization plot is presented in **Error! Reference source not found.** for R12-50, where a sharp peak at 32.5˚ is observed on the right which represents the GaAs substrate with a lattice constant of 5.65 Å. The farthest left peak near 29.5˚ is associated with the AlSb layer with a lattice constant of 6.13 Å, while the broadest peak around 30˚ represents the 100 nm GaSb capping, with a lattice constant of 6.09 Å. The layering is shown in Figure 26. The relative low intensity of the GaSb peak indicates that there is less material represented, which is expected since it is the thinnest layer of the structure. The AlSb shows a sharp scattering peak indicative of good crystal structure. The relative sharpness of the AlSb peak compared to the GaSb peak suggests that the GaSb layers contain more strain related defects than the AlSb layer. While the AlSb peak is not as narrow as that of the GaAs substrate, it does appear to have a fairly regular lattice, indicating good epitaxial growth with very little residual strain.

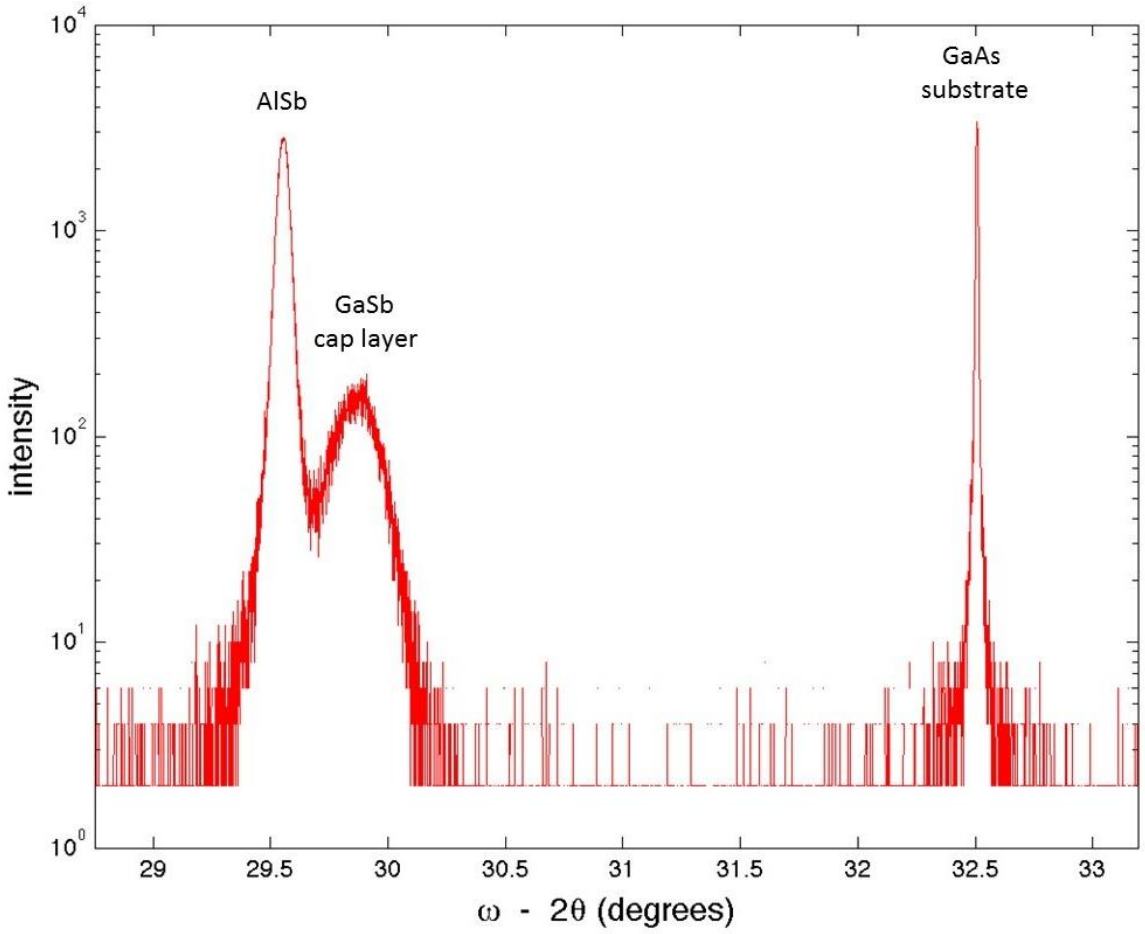

Figure 33. XRD plot of R12-50.

A similar plot is shown in Figure 34 for R12-23, where the horizontal axis has been converted to arc seconds and normalized such that the substrate is the zero reference. The range of the horizontal axis has also been shortened, making the peaks appear to be broader in this plot, although they are actually very similar.

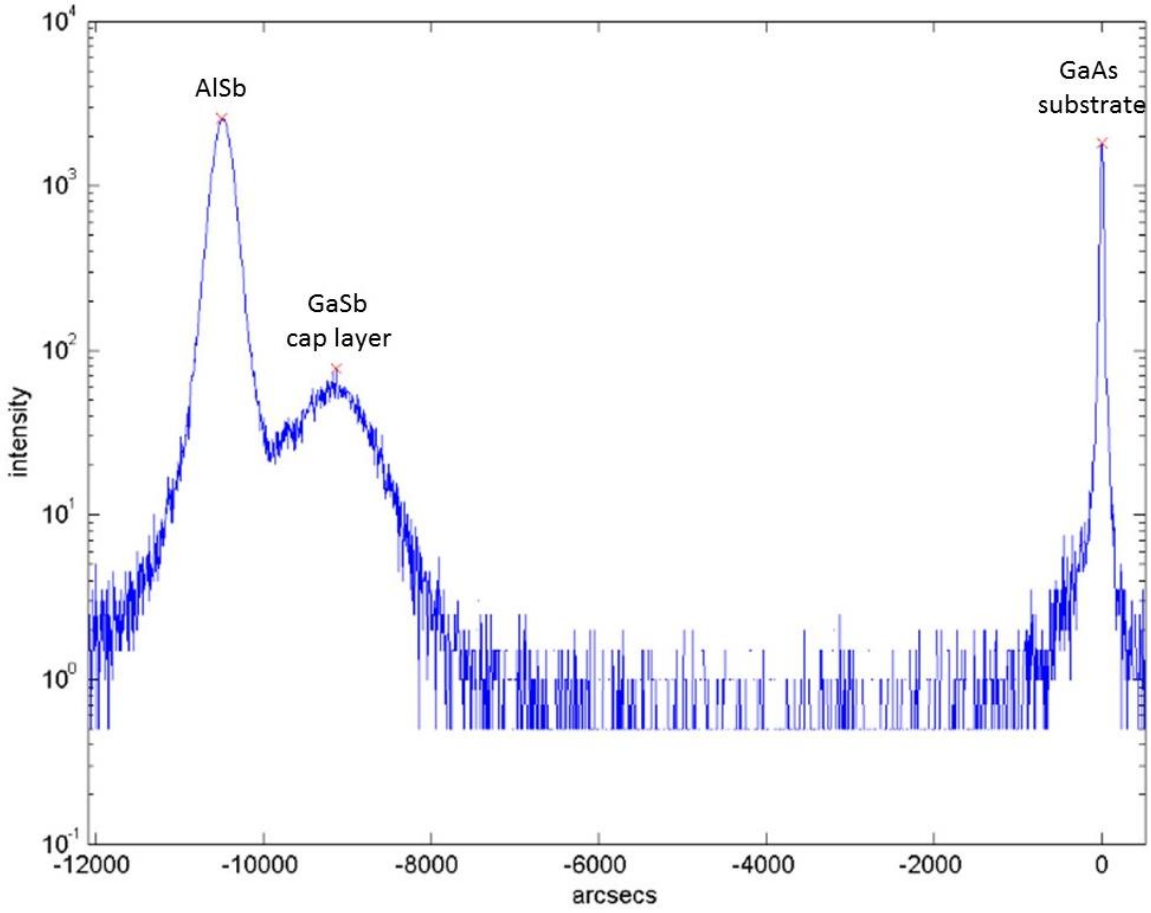

Figure 34. XRD scan of R12-23 PIN structure. Here, the horizontal axis has been converted to arc seconds, with the GaAs substrate set to zero.

The XRD scan of the undoped Hall structure, R12-145, is shown in Figure 35. Here, the GaSb peak is absent, as the structure only contains AlSb and GaAs layers (structure in Figure 27). There is some broadening to the right side of the AlSb peak, indicating tensile strain between the AlSb and GaAs layers.

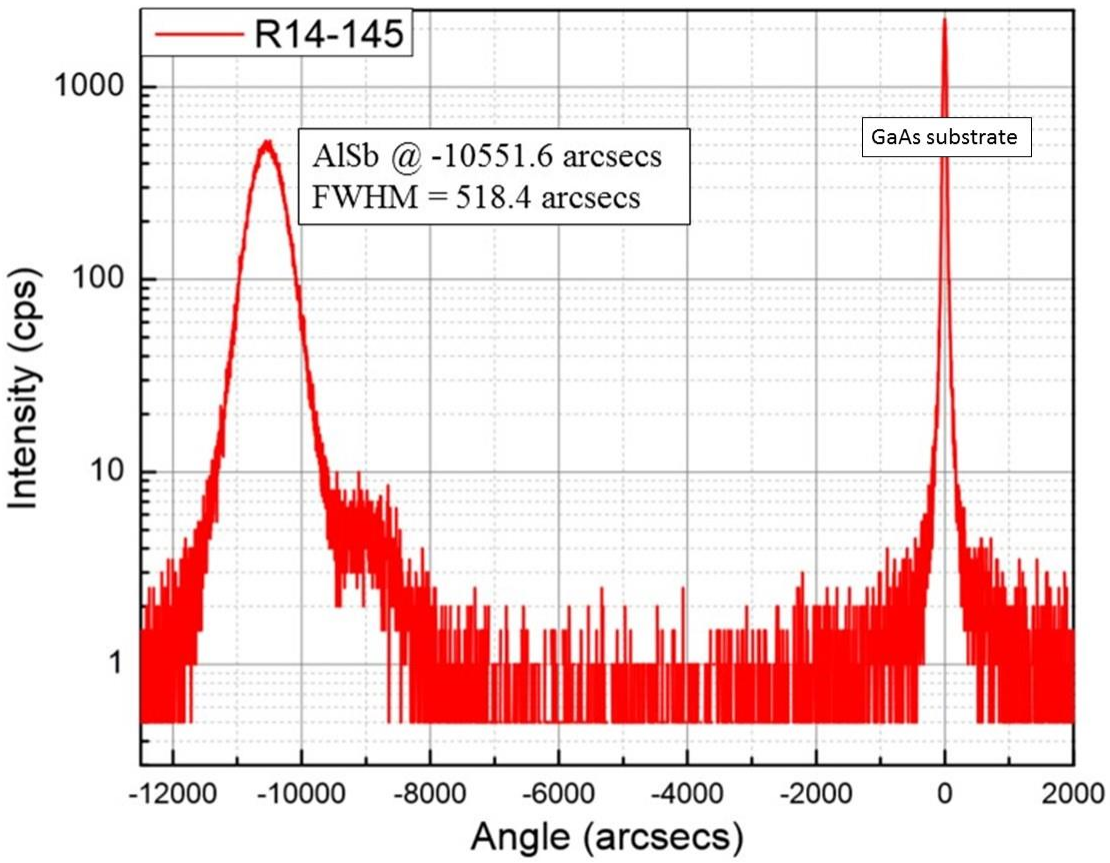

Figure 35. XRD of R14-145 undoped AlSb Hall structure. Here, the horizontal axis has been converted to arc seconds, with the GaAs substrate set to zero.

3.2.2.3 Electrical Quality

The electrical characterization of the AlSb samples was primarily performed using Hall effect measurements of the doped and undoped Hall structures (Figure 27), though I-V curves were also measured for cleaved pieces of the diode structures (Figure 26).

A comprehensive study of the transport properties using Hall effect measurements for undoped and doped AlSb is presented in Chapter 7.

The diode samples R12-23 and R12-50 were cleaved to remove metalized edges and to create samples with different dimensions. The I-V measurement results for R12-50 are shown in Figure 36, where sub-sample R12-23d appears to have the most diode-like behavior.

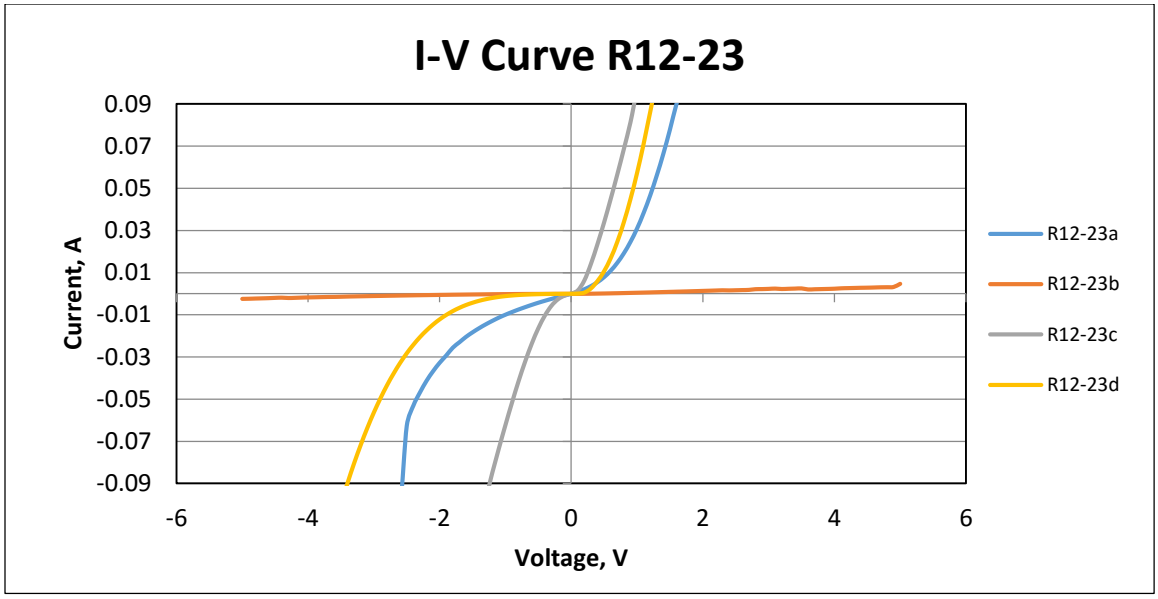

Figure 36. I-V measurements of R12-23.

Figure 37 shows the I-V measurement results for annealed and non-annealed sub-samples of R12-50, where none of the curves are very diode-like.

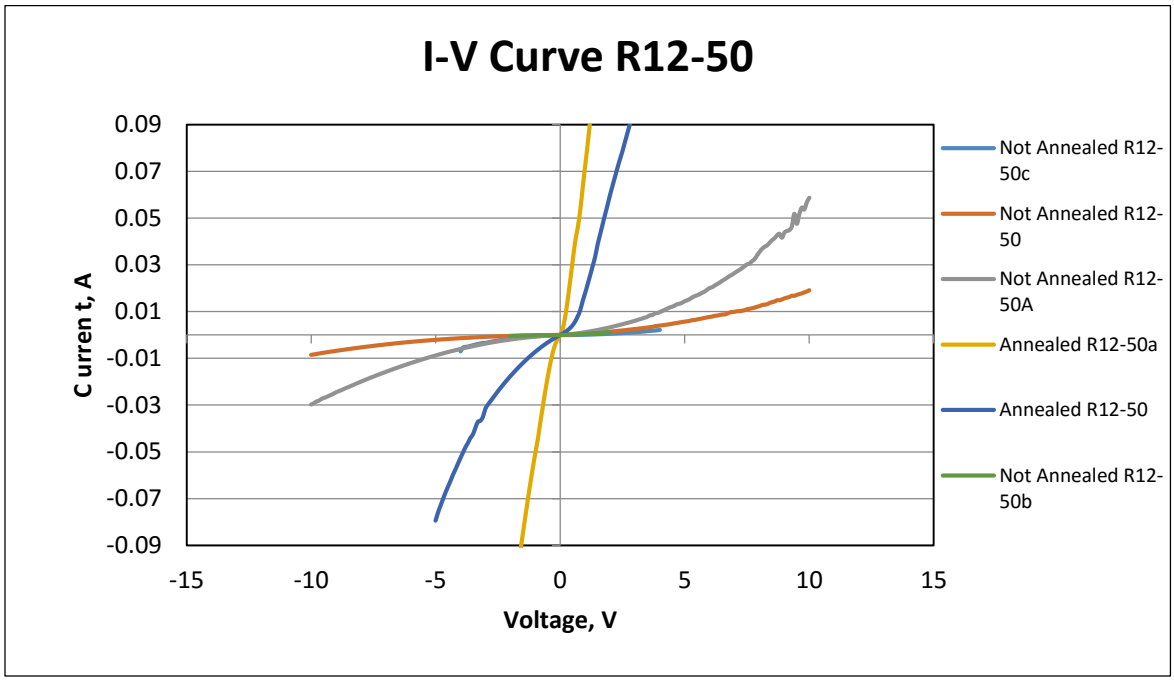

Figure 37. I-V measurements of R12-50.

Growth of AlSb on GaAs substrates introduces a large strain due to the large lattice mismatch (~8%). After a few monolayers of psuedomorphic growth under compression, the epilayer relaxes leaving an array of periodic dislocations as an interface, as shown in the TEM image in Figure 38, left. The threading dislocation density was large near the interface but was reduced significantly as the AlSb growth progressed (Figure 38, right). Nomarski imaging was used to analyze the surface, which was found to be smooth with few defects. The RMS roughness is in the range of 1-2 mm. Screw dislocations (5×10^{7} cm^{-2}) were observed with AFM measurements, indicative of shear strain commonly seen with heteroepitaxial growth of antimonides. XRD analysis also showed some strain in the AlSb

layer, with a FWHM of 0.1440 degrees. This corresponds to a defect density of 4-6×10^8 cm^{-2} based on XRD rocking curve calculations.

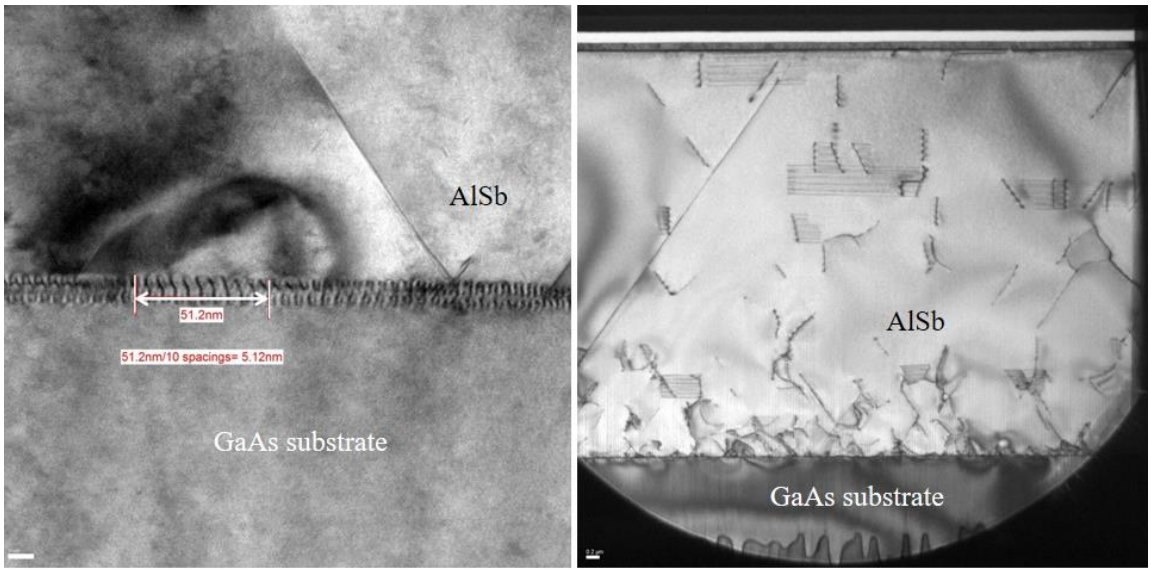

Figure 38. TEM images of AlSb on GaAs, with higher resolution at left to show lattice dislocation spacing.

3.2.3 Radiation Response

During radiation response measurements, the diode structure was placed with the n-type substrate in contact with a copper plate while probes were placed on the copper plate surface and the p-type side of the structure to deliver bias and to measure output pulses. The microprobe station was kept inside a metal enclosure to reduce RF noise. The photographs in Figure 39 show the experimental setup. Standard readout electronics were used and the output signals were converted by Maestro software to produce pulse-height spectra. Sealed radiation sources used include ^{241}Am, ^{252}Cf, and ^{239}Pu, and the distance

between the sources and the detector surface was fixed at 8 mm. The thin film AlSb diodes were cleaved into smaller area pieces to improve signal pulse height, per known voltage-capacitance relationships for diodes.

Figure 39. Images of radiation detection experimental setup.

Direct radiation measurements were performed with the MBE grown AlSb diodes using ^{252}Cf, ^{241}Am, and ^{239}Pu alpha particles, with fluence rates of 2500, 150, and 4700 cm^{-2} s^{-1}, respectively, with the caveat on Am effective activity from chapter 5. For ^{241}Am alpha particles, the detector responses from diode samples with surface areas ranging from 10.5 mm^2 to 1.0 mm^2 are shown in Figure 40 (top), where it was observed that smaller surface area detectors produced larger output voltage pulses, associated with higher channel number. This is consistent with capacitance-voltage relationships for diodes, where the diode capacitance increases as the cross sectional area of the junction [38] and the pulse height is inversely proportional to the capacitance [43], seen in other work [34, 39, 40].

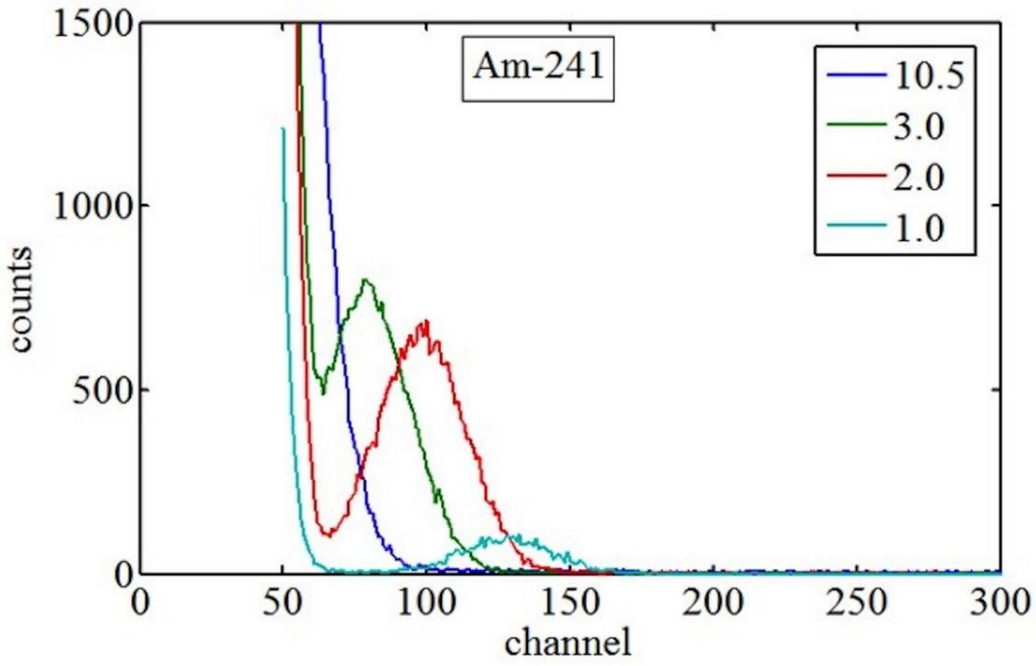

Figure 40. AlSb radiation response from detector samples of different surface areas.

As the PIN structure samples were grown prior to optimization studies, the smallest of the diodes (1 mm^2) was used for best signal-to-noise results. The diode IV curve (Figure 41) is representative of the 1 mm^2 AlSb sample. With more optimized materials based on the current study, diode characteristics and signal-to-noise are expected to greatly improve.

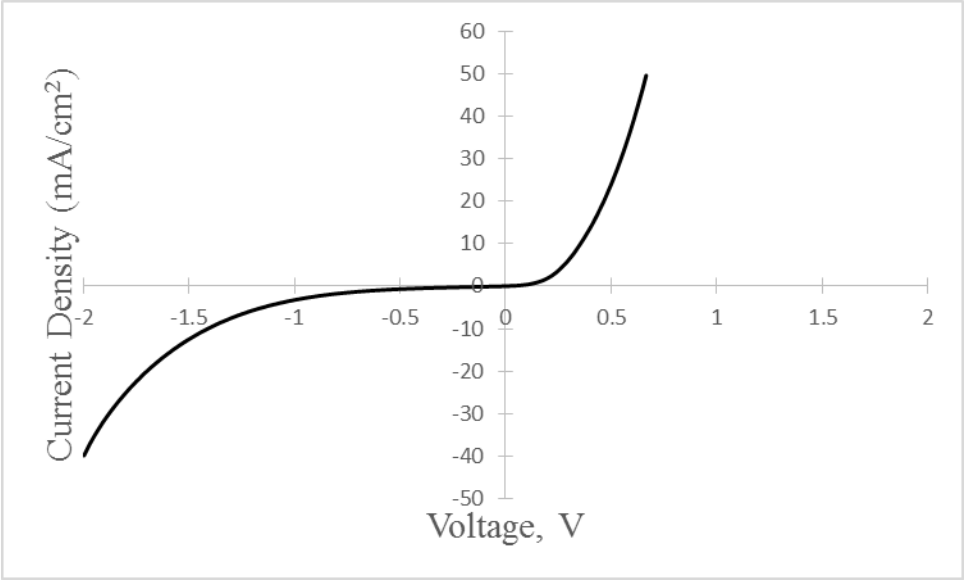

Figure 41. I-V measurement of AlSb PIN diode sample (R12-23d) used for radiation detection.

Though full energy was not deposited in the thin active layer, the alpha particle peaks remained strong and easily discernible above background, and basic energy spectroscopy was performed comparing the sources over 48 hours, see Figure 42(top). The average centroid for the alpha peaks was channel 135 with a standard deviation of 12 channels, resulting in an energy resolution of about 9%. Following the Bragg curve for alpha energy deposited in matter as a function of the penetration depth (Figure 42, bottom),

more energetic alphas traveled deeper into the material but deposited less energy in the thin detector region. Conversely, less energetic Pu-239 alphas deposited more energy into the detector, resulting in a larger pulse in the oscilloscope and the alpha peak being centered at a higher channel number. The colored vertical lines in the top plots in Figure 42 correspond with the colored curves in the Bragg illustration below.

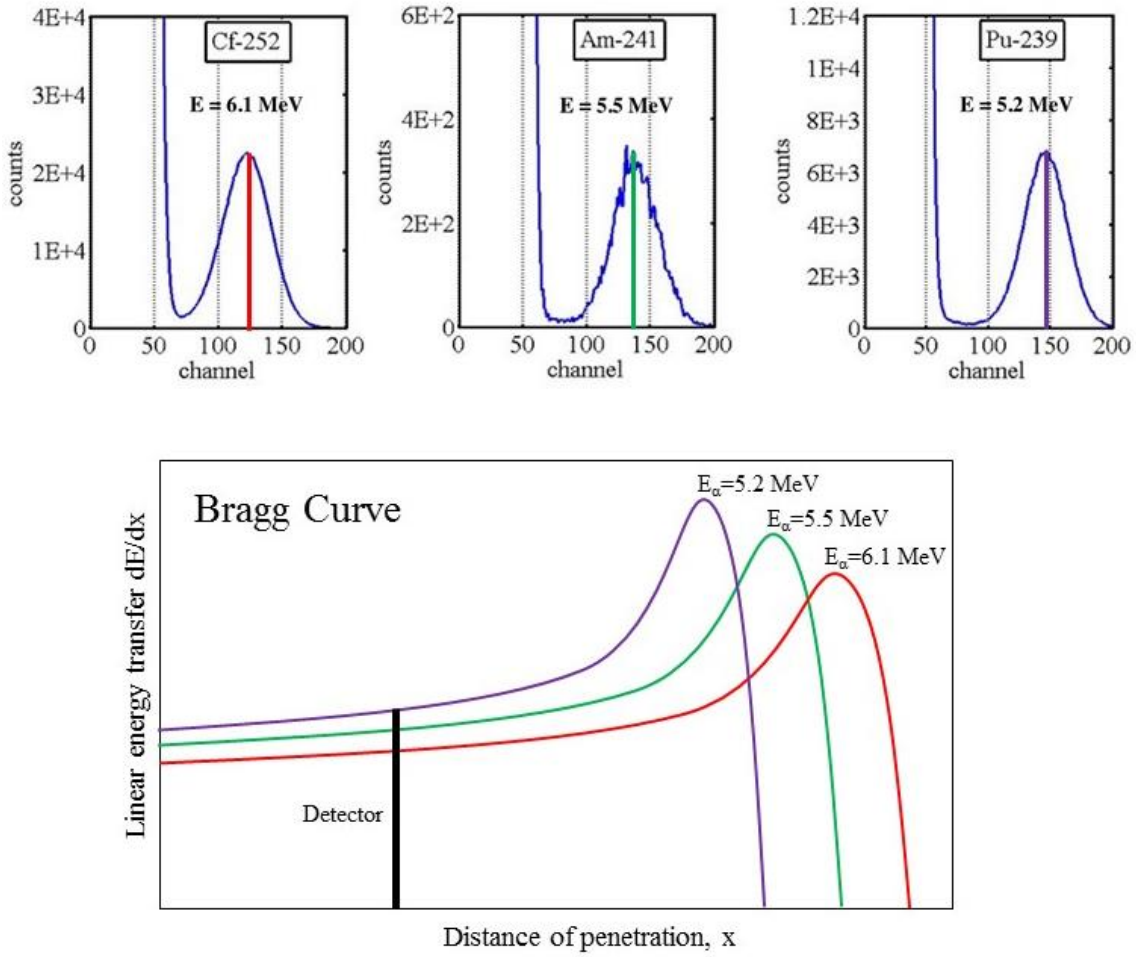

Figure 42. AlSb detector response for different alpha energies, top, and corresponding illustration of Bragg curves, bottom.

3.3 Comparison of AlSb with GaSb

In addition to improved counting statistics, the AlSb detection pulses were also larger compared with those seen with the GaSb detectors, resulting in higher channel peaks and better signal to noise response. This can be seen clearly in the plots in Figure 43, where the alpha peaks are more separated from background for the AlSb spectra. In the GaSb spectra, as the surface area approaches 1 mm^2 the signal nearly gets lost in the noise, whereas in the AlSb spectra the surface area is larger than 3 mm^2 before the noise dominates. This can be attributed to the larger band gap for AlSb material, resulting in fewer thermally generated charge carriers compared with GaSb.

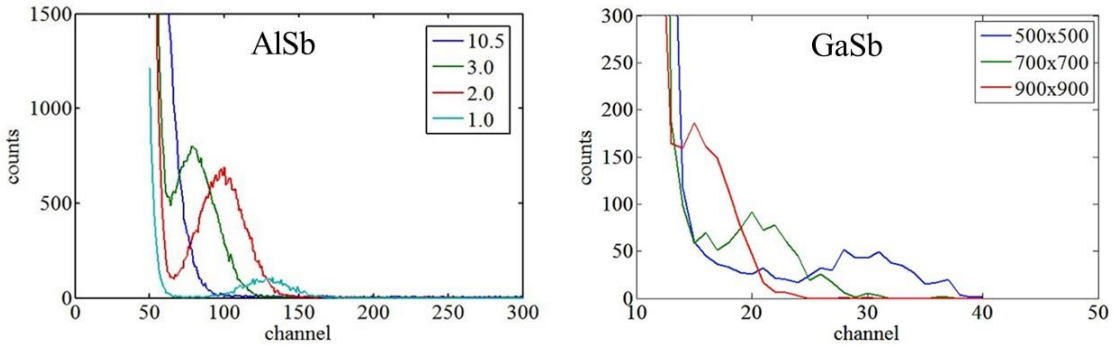

Figure 43. AlSb (left) compared with GaSb (right) spectra of Am-241 alphas detected by devices of different surface areas, from Figure 24 and Figure 40.

Chapter 4

Optimization of Transport Properties

4.1 Transport Properties

In terms of radiation detectors, it is desirable to have high carrier mobilities (for both electrons and holes), high resistivity, and low free carrier concentrations. As discussed in Chapter 1, charge motion induces a pulse in the electrodes following a radiation interaction event, which depends on carrier mobility. High resistivity allows the use of high fields to accelerate the charges and reduce recombination without an overwhelming leakage current. Carrier concentration is inversely proportional to both mobility and resistivity, so minimizing this value in turn has the effect of optimizing the other material properties.

Carrier transport properties in semiconductors are largely governed by scattering effects [44]. The following subsections will describe these properties and discuss the theory behind the measurement or calculation methods used in this research. Dieter Schroder [45] gives a comprehensive review of this subject in his textbook Semiconductor Material and

Device Characterization and the reader is directed there for further details, as the discussion below is a summary.

4.1.1 Carrier Concentration

The intrinsic concentration of charge carriers in a material is a measure of the number of electrons in the conduction band and holes in the valence band. These carriers are not generated by radiation interactions and exist in steady state, where they contribute to leakage currents under an applied bias in a semiconductor detector. In the case where the intentionally added dopants are uniformly distributed, the majority carrier density is the same as the doping concentration [45], and the following discussion will use this assumption. Although the carrier concentration may be measured myriad ways, both optically and electrically, using the Hall effect is a clever way of determining several transport properties in a single measurement. This method computes an average carrier density [45].

Theoretically, the Hall coefficient is described by

$$R_H = \frac{r(p - b^2 n)}{q(p + bn)^2} \ , \tag{19}$$

although it is often simplified into two equations; one for each carrier type [45]:

$$R_H = \frac{r}{qp} \text{ for p-type} \tag{20}$$

$$R_H = -\frac{r}{qn} \text{ for n-type}$$

where r is the scattering factor. Since r is most often unknown, it is usually assumed to be unity, although its actual value is between 1 and 2. The other parameters, *n*, *p*, *q*, and *b*, represent the electron density, hole density, electronic charge, and a ratio of the carrier mobilities, respectively. Experimentally, the Hall coefficient (R_H) is related to the sample thickness (*t*), the Hall voltage (V_H), the magnetic field (*B*), and the current (*I*) by

$$R_H = \frac{tV_H}{BI} \ . \tag{21}$$

Rearranging the reduced theoretical and experimental equations, the carrier densities for holes and electrons can be calculated by

$$p = \frac{B}{tRq}$$
$$n = -\frac{B}{tRq} \ . \tag{22}$$

Note that the measureable carrier concentration is related to the difference between the donor and acceptor densities.

4.1.2 Resistivity

The resistivity of a semiconductor material is dependent on the nature of the charge carriers and how much they resist against the flow of an electric current. Bulk grown

materials do not maintain uniform resistivity due to variability in growth, whereas epitaxially grown materials are highly uniform and thus exhibit very consistent resistivity throughout the crystal [45]. The following relationship between the carrier densities and mobilities can be used to calculate the resistivity in the case where the population of the majority carrier is much larger than that of the minority carrier, so that the minority carrier terms can be neglected,

$$\rho = \frac{1}{q(n\mu_n + p\mu_p)} \tag{23}$$

However, we wish to use the resistivity to calculate the carrier mobility, so another approach is needed.

Van der Pauw's theory and equations provide the necessary tools to directly measure the resistivity of an arbitrarily shaped sample, so long as a set of conditions is maintained [45]:

a) the location of the contacts is at the periphery of the sample, as in Figure 44,
b) the size of the contacts is small enough to be mathematically neglected,
c) the thickness of the sample is uniform, and
d) the sample surface is continuous.

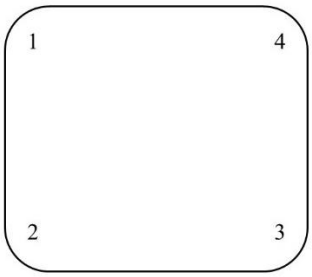

Figure 44. Van der Pauw contacts.

The measurement required is that of the resistances between neighboring contacts, which is often calculated using Ohm's Law,

$$R_{12,34} = \frac{V_{34}}{I_{12}}$$
$$R_{23,41} = \frac{V_{41}}{I_{23}} \tag{24}$$

where the subscript indicates the contacts uses (e.g., I_{12} represents current flow from 1 to 2). In general, a correction factor, *F*, is used to account for the difference in resistances between neighboring contacts when calculating the resistivity of an asymmetrical sample.

$$\rho = \frac{\pi t}{\ln(2)} \frac{(R_{12,34} + R_{23,41})}{2} F \tag{25}$$

However, if the sample geometry is also symmetrical (as in Figure 44), the resistivity between neighboring contacts is equal and the equation may be reduced to

$$\rho = \frac{\pi t}{\ln(2)} R_{12,34} \ . \tag{26}$$

Semiconductor resistivity is sensitive to changes in carrier concentration, as illustrated in Figure 45 for n- and p-type GaP, GaAs and Ge [46].

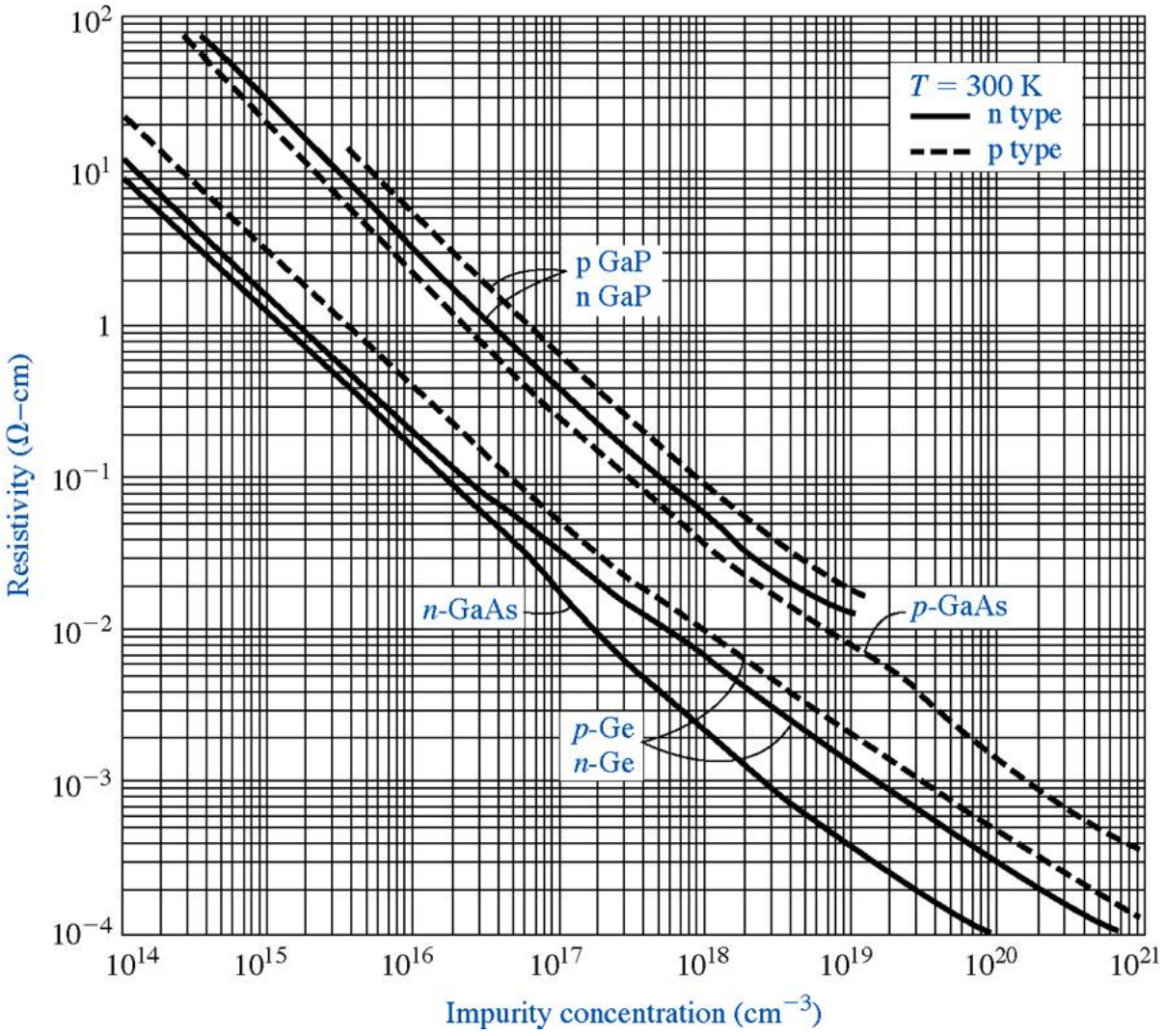

Figure 45. The effect of dopant concentration on resistivity [46].

High-resistivity ($\rho > 10^{7}$ Ω-cm) measurements using van der Pauw methods are susceptible to errors due to leakage paths and sample loading by the voltmeter [45].

4.1.3 Carrier Mobility

The carrier mobility is a term which is used to describe the ease with which electrons or holes move within a semiconductor when influenced by an electric field. It is proportional to the conductivity. There are several different types of mobility parameters for a given material, though the drift mobility and the Hall mobility are most often considered for characterization purposes. Hall measurement techniques are most often used as they are easily performed. Hall mobility and drift mobility are related by the scattering factor, *r* [44, 45]. This section will be limited to a discussion of the Hall mobility, as it is the parameter characterized in this research.

The Hall effect is a phenomenon that occurs when a magnetic field is applied to a conducting material perpendicular to the flow of current. As Figure 46 illustrates, the free dominant carriers accumulate at one edge under the influence the orthogonally applied current and magnetic field.

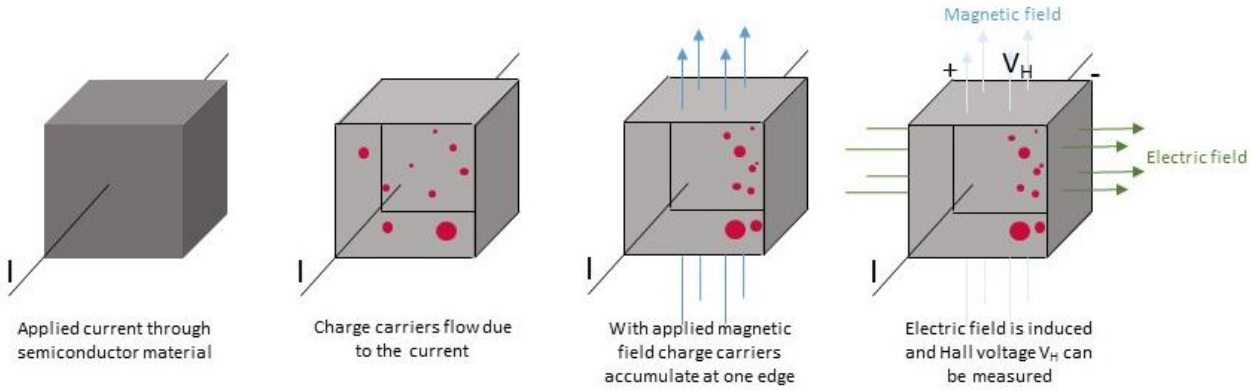

Figure 46. Diagram of the Hall effect showing the relation between field and charge motion.

This induces an electric field orthogonal to both the current and the magnetic field. The voltage potential difference, V_H, is measured and used to calculate the Hall coefficient, R_H. The Hall mobility is proportional to the Hall coefficient and the resistivity, ρ, or conductivity, σ, of a material.

$$\mu = \frac{|R_H|}{\rho} = |R_H|\sigma \tag{27}$$

Because of added scattering, increasing the dopant concentration tends to reduce the mobility of charge carriers. This effect is shown in Figure 47 for Ge, Si and GaAs of both n- and p-type conductivity [46]. However, if the semiconductor material is already intrinsically more p or n-type, dopants can be added for compensation, which can in turn reduce the number of free carriers and thus improve transport.

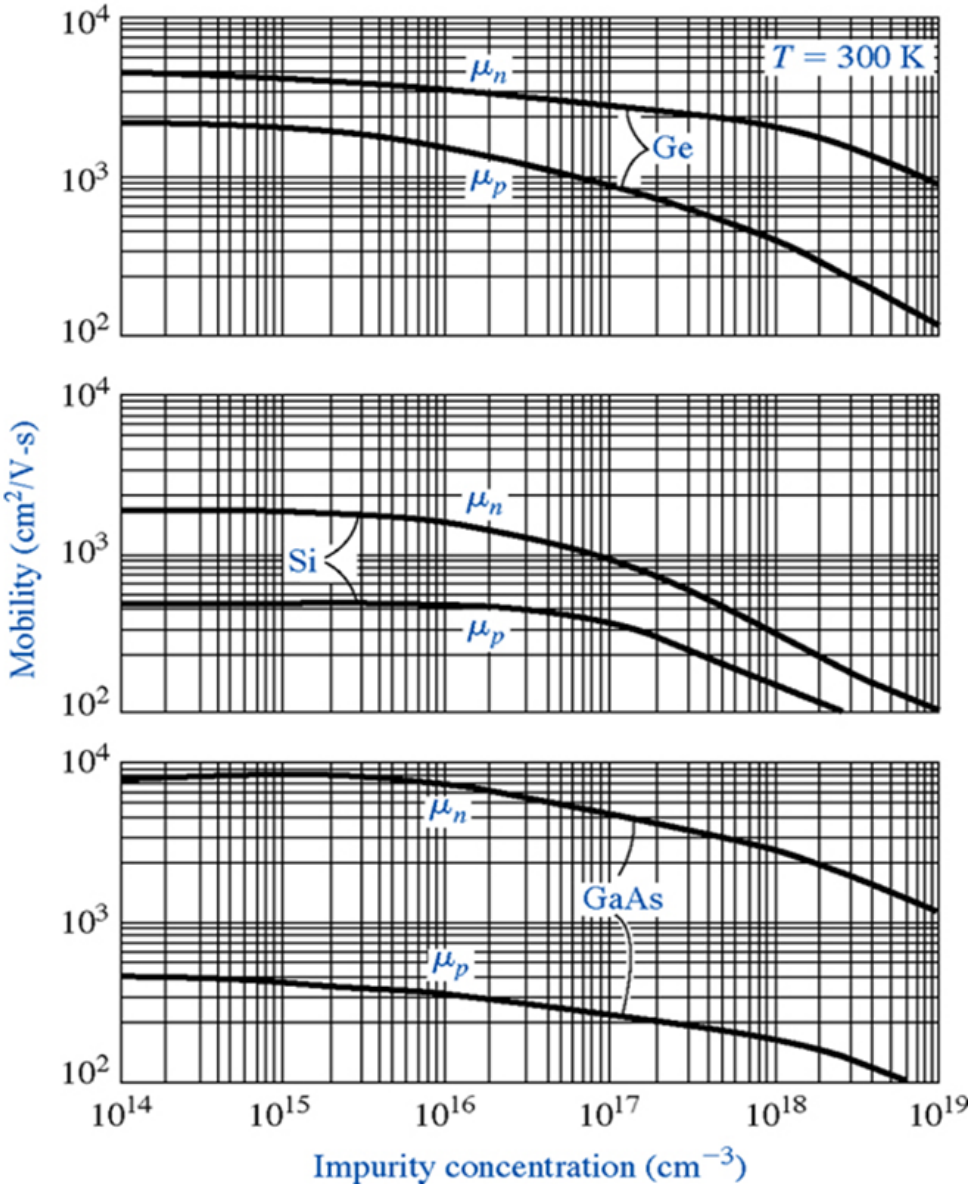

Figure 47. The effect of dopant concentration on mobility [46].

4.2 Doping Concentration – Hall Study

Several growths were performed with varying levels of p- and n-type intentional doping, and no intentional doping, to examine trends to produce high quality AlSb. To characterize the materials, Hall measurements were taken using four-point probe and van der Pauw methods.

The purpose of the Hall measurement study was to determine the effect of p- and n-type doping on the carrier mobility and resistivity. These parameters are very sensitive to defects and impurities in the material and have been inconsistently reported in literature due to variations in material quality for different growths. MBE techniques are used to grow very high quality structures using AlSb, although the electrical properties are rarely measured as the AlSb layer is often used as a buffer and not an active region. This study has resulted in better understanding of the electrical properties of undoped and doped MBE grown AlSb material. These findings were published in the proceedings of the IEEE Nuclear Science Symposium and Medical Imaging Conference and the Journal of Electronic Materials [41, 42].

It was expected, based on bulk growth reports, that the AlSb material would exhibit p-type conductivity and that compensation by doping would improve electrical performance. Doped samples were grown on the GaAs substrates using GaTe for n-type and Be for p-type conductivity in the AlSb layer. One undoped AlSb sample and seven doped AlSb samples were compared with an undoped homoepitaxial GaAs sample to rule

out contribution from the substrate. Be doping ranged from 6×10^{14} cm^{-3} to 1×10^{17} cm^{-3} and Te doping ranged from 8×10^{9} cm^{-3} to 1×10^{17} cm^{-3}.

4.2.1 Sample Structure & Doping Design

As shown in Figure 48, the structure design for the Hall effect characterization of AlSb consisted of 3 microns of undoped or doped AlSb grown on a semi-insulating GaAs substrate, with a 10 nm GaAs cap layer on top to protect the AlSb from oxidation. The choice was made to use GaAs, rather than lattice-similar GaSb, for the substrate and cap layer material to minimize conductivity in the non-AlSb layers.

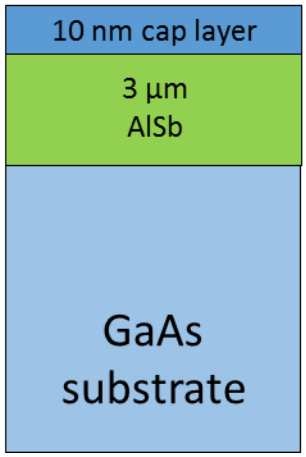

Figure 48. AlSb doping study sample structure.

Intended dopant concentration levels for Be doped samples were 5×10^{15}, 1×10^{16}, and 1×10^{17} cm^{-3}, corresponding with Be source cell temperatures of 590, 615, and 660 ºC, respectively. Because the AlSb material is already slightly p-type, additional p-type doping was straightforward and predictable.

To change the polarity of the dominant carrier, the p-type nature must first be compensated for. During the transition from slightly p-type (nearly SI), the material becomes SI before exhibiting n-type conductivity.

The intended doping for the Te-doped samples was 1×10^{15}, 5×10^{15}, 2×10^{16}, and 1×10^{17} cm^{-3}, corresponding with Te source cell temperatures of 320, 365, 393, and 430 ºC, respectively.

4.2.2 Hall Measurements

The Hall measurements were performed at the Center for High Technology Materials (CHTM) at the University of New Mexico. Samples were cleaved into 1 cm × 1 cm squares and In contacts were annealed to the corners of the epi-surface (GaAs cap layer) using a hotplate at 350 ºC for 3 minutes. For measurement, each prepared Hall sample was then placed into a holder with probes anchored to each corner contact, as seen in Figure 49.

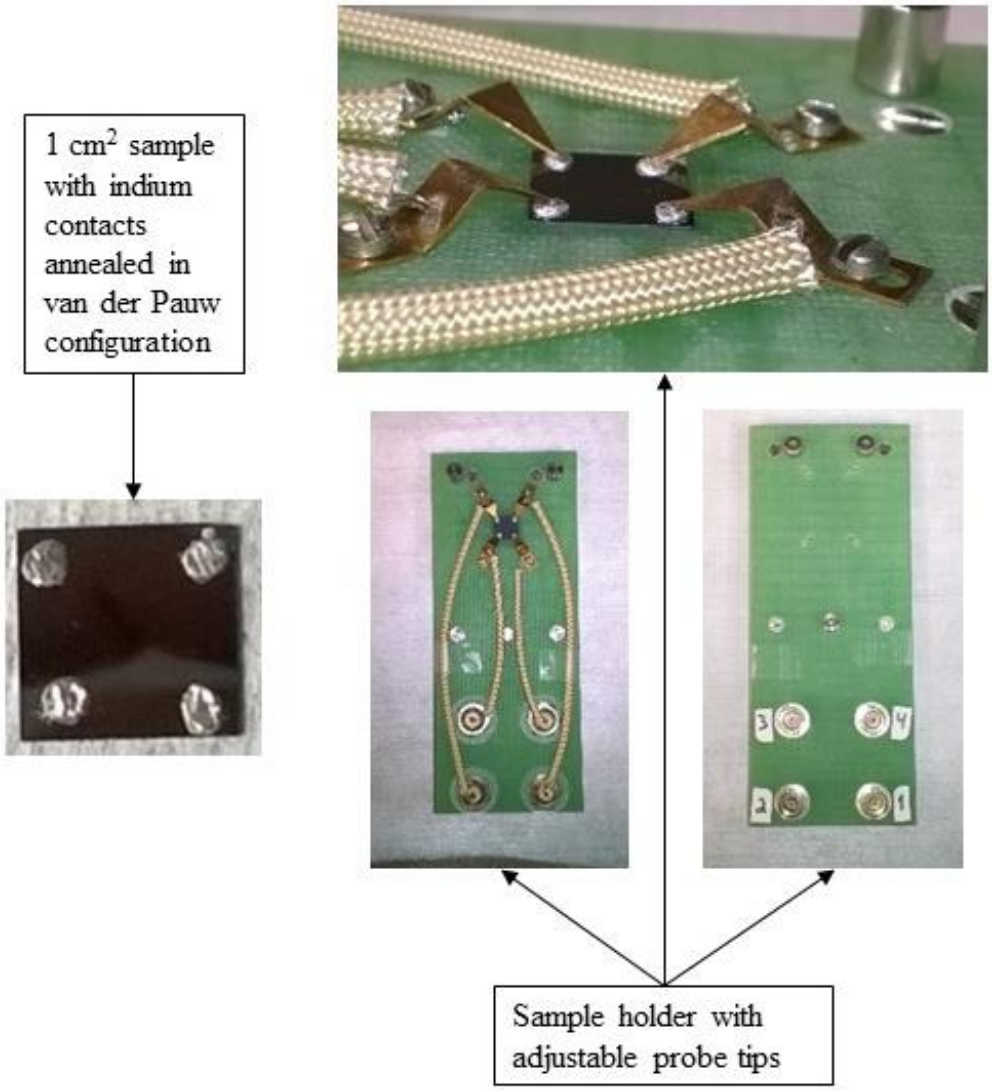

Figure 49. Hall sample holder.

Four triaxial cables were connected between the holder and the testing equipment, and the holder was placed into the magnet, as shown in Figure 50. The electronics were controlled by a LabVIEW program, which also calculated the electrical parameters based on measurement readings.

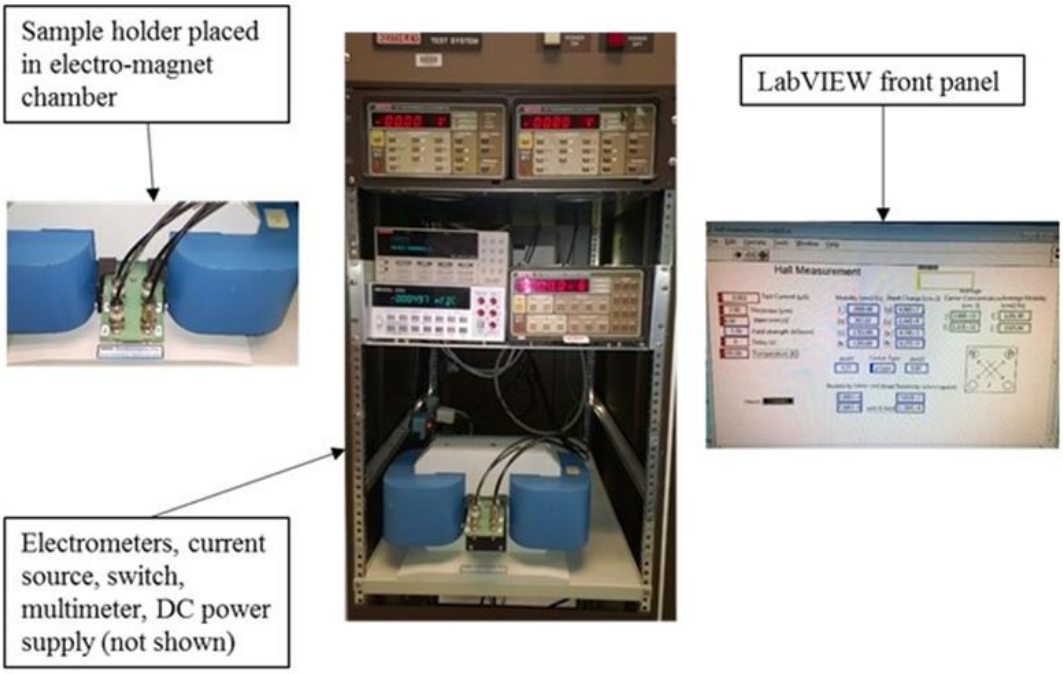

Figure 50. Hall equipment setup.

The Hall measurement LabVIEW program takes the resistances across the two diagonal paths between the four point contacts, along with the resistance of two neighboring contacts with and without the magnetic field applied. These resistance values are then used to calculate the following:

$$Sheet\ Resistivity\ [\Omega/square] = \left(\frac{|R_{12,34}| + |R_{23,,=41}|}{2\ln(2)}\right) F\pi$$

$$Bulk\ Resistivity\ [\Omega - cm] = (Sheet\ Resisitivity) * (Sample\ Thickness\ [cm])$$

$$Hall\ Mobility\ \left[\frac{cm^2}{Vs}\right] = \left(\frac{|R_{24.13} - R_{24,13\ with\ B-Field}|}{10^{-5}B[kGauss]}\right) * \left(\frac{1}{Sheet\ Resistivity}\right)$$

$$Sheet\ Charge\ [cm^{-2}] = \left(\frac{1}{Hall\ Mobility * Sheet\ Resistivity * 1.6 \times 10^{-19}}\right)$$

$$Carrier\ Concentration\ [cm^{-3}] = \frac{Sheet\ Charge}{Sample\ Thickness\ [cm]}$$

Because of the high resistance of several of the samples, the existing Hall setup was unable to measure the properties very accurately. For large resistance measurements, a very small test current was needed. The lower limit for the test current with the Keithley 224 Programmable Current Source was quoted at 20 μA, although it would allow currents as low as 0.005 μA (probably with less certainty). This limited the measurability of transport properties to samples with resistances less than about 20 MΩ, associated with carrier concentrations of about 10^{11} cm^{-3} or greater.

The resistance between contacts was measured with a handheld multimeter and the results are given in Table 6, along with the corresponding test current used to perform Hall measurements. Four of the samples were too resistive to be measured with the existing Hall setup. In order to measure the highly resistive samples, a current source mirror (transfer function $I_{out} = I_{in}/100{,}000$) was designed and constructed by F. K. Husher (see Appendix B for device documentation). Sample carrier concentrations were measured as low as 2×10^{9} cm^{-3} for undoped AlSb with the current mirror installed.

Table 6. Resistance and test current, in order of increasing resistance between contacts. The highlighted rows indicate highly resistive samples.

Sample #	Resistance between contacts	Test Current [μA]
R14-171	1.5 kΩ	200
R14-174	13 kΩ	15
R14-176	0.3 MΩ	0.8
R14-177	0.7 MΩ	160
R14-172	0.8 MΩ	20
R14-144	20 MΩ	0.01
R14-175	>50 MΩ	0.005
R14-145	>50 MΩ	0.005
R14-178	>50 MΩ	0.005
R15-034	>50 MΩ	0.005

4.2.3 Results & Analysis

Table 7 outlines the MBE growth doping details and the intended doping level versus the measured carrier concentration. Heavier doping was easier to predict, with concentrations larger than 10^{16} cm^{-3} being symmetric between intended and measured levels for both Be and Te doped samples. Lighter doping was especially problematic for Te-doped samples, where a difference of many orders of magnitude was observed. This is attributed to initial compensation effects of the mildly p-type AlSb.

Table 7. Doping details for samples with intentional added carriers. The highlighted rows indicate doped samples with very low carrier concentration, despite adding dopants.

Sample #	Dopant	Intended Doping Level [cm^{-3}]	Dopant Cell Temperature [˚C]	Measured Carrier Concentration [cm^{-3}]
R14-175	Te	1×10^{15}	320	8×10^{9}
R14-178	Te	5×10^{15}	365	2×10^{10}
R14-176	Be	5×10^{15}	590	6×10^{14}
R14-174	Be	1×10^{16}	615	1×10^{16}
R14-172	Te	2×10^{16}	393	2×10^{16}
R14-171	Be	1×10^{17}	660	1×10^{17}
R14-177	Te	1×10^{17}	430	1×10^{17}

Results for the Hall measurements of the undoped and intentionally doped samples are presented in Table 8, where the highlighted rows are representative of samples with exceptionally good values for both mobility and resistivity. These results follow the predicted nature for semiconductor materials, with mobility and resistivity increasing as the carrier concentration is reduced.

Table 8. Hall results, ordered by active layer and increasing carrier concentration. UID is unintentional doping - samples with no doping applied.

Sample #	Active Layer	Carrier Type	Measured Carrier Concentration [cm^{-3}]	Hall Mobility [cm^2/V-s]	Resistivity [Ω-cm]
R14-144	GaAs	p	5×10^{12}	260	4×10^{3}
R14-145	AlSb	SI	2×10^{9}	3000	1×10^{6}
R15-034	AlSb	SI	8×10^{9}	900	1×10^{6}
R14-175	AlSb	SI	8×10^{9}	1600	6×10^{5}
R14-178	AlSb	SI	2×10^{10}	3000	4×10^{5}
R14-176	AlSb	p	6×10^{14}	100	1×10^{2}
R14-174	AlSb	p	1×10^{16}	200	2×10^{0}
R14-172	AlSb	n	2×10^{16}	60	5×10^{0}
R14-171	AlSb	p	1×10^{17}	200	2×10^{-1}
R14-177	AlSb	n	1×10^{17}	140	4×10^{-1}

The measured net carrier concentration is shown as a function of inverse temperature in the semi-log Arrhenius plot in Figure 51. As expected, the Be-doped samples follow a linear trend due to the well-behaved nature of Be as a dopant. On the other hand, the GaTe-doped samples are more scattered, with a gap between very lightly

doped samples and more heavily doped samples. This region of doping is difficult to achieve because of compensation effects. The extrapolated vaporization temperature was calculated to be 231º C and 295º C for Te and Be doping sources, respectively.

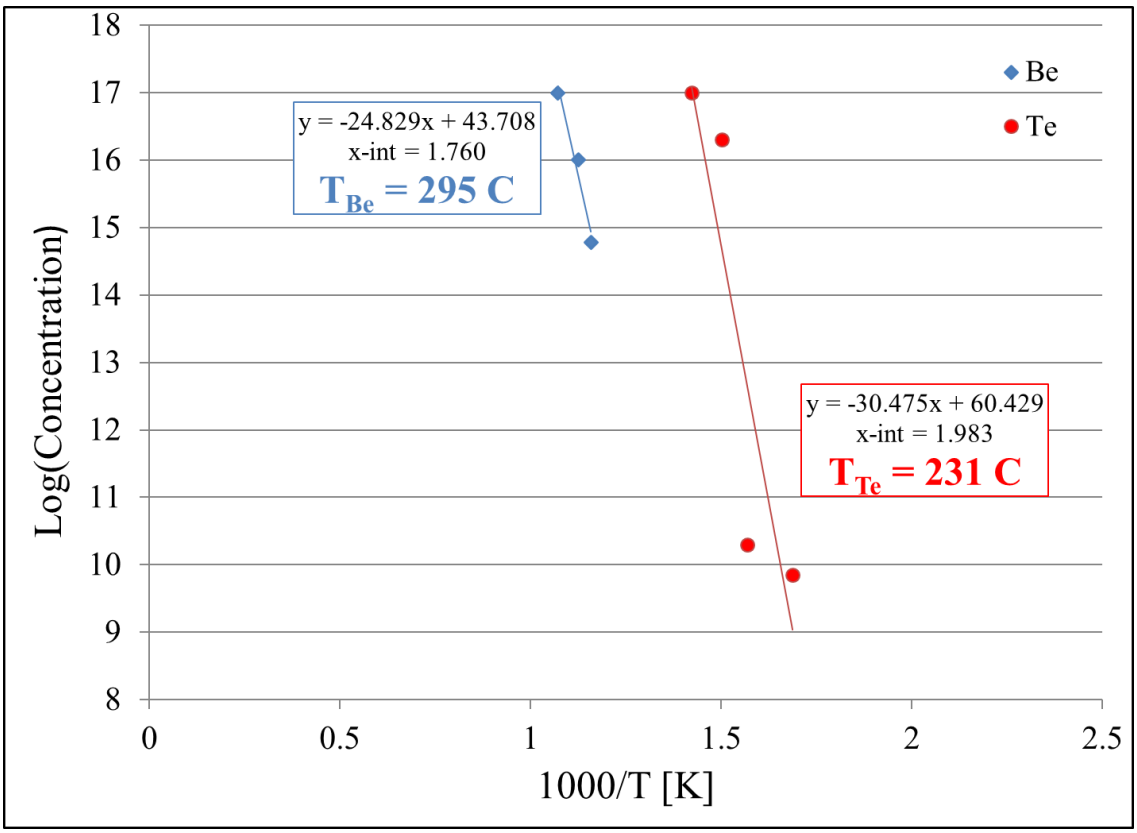

Figure 51. Arrhenius Plot of Te- and Be-doped AlSb samples. Extrapolated vaporization temperatures are 295 and 231 ˚C for Be and Te doping sources, respectively.

4.3 MW-PCD Carrier Lifetime Study

4.3.1 Carrier Lifetime

Carrier lifetime is a general term to describe all carrier trapping and scattering effects that determine the amount of time between carrier generation and carrier recombination. The primary mechanisms that result in the loss of carriers are Auger recombination, radiative recombination, and Shockley-Read-Hall (SRH) multi-phonon recombination. The associated lifetimes are related to the recombination lifetime, τ_r , by

$$\tau_r = \left[\frac{1}{\tau_{SRH}} + \frac{1}{\tau_{rad}} + \frac{1}{\tau_{Auger}}\right]^{-1} \tag{28}$$

All recombination processes are driven by the necessity to restore the system energy to equilibrium. The equations governing each of these mechanisms are given in [45], but are omitted here as they are not explicitly necessary for this discussion.

As the diagram in Figure 52 shows, Auger recombination occurs when the recombination energy is transferred to a third carrier, either an electron or a hole, and the Auger lifetime is proportional to the carrier density squared. It is an intrinsic property of the material. Radiative recombination releases an energetic photon when electron-hole pairs recombine directly from band to band, and is not dominant in indirect gap materials. SRH recombination depends on an intermediate energy level where electrons and holes meet and phonons are released. It is highly influenced by material quality, as the impurities serve as trapping centers. Impurity levels can have a large impact on the lifetime of

generated carriers in a material. The nearer a trap energy level is to the center of the semiconductor band gap, the higher the trapping efficiency [47]. In general, impurities in a material will shorten the carrier lifetime in the conduction band.

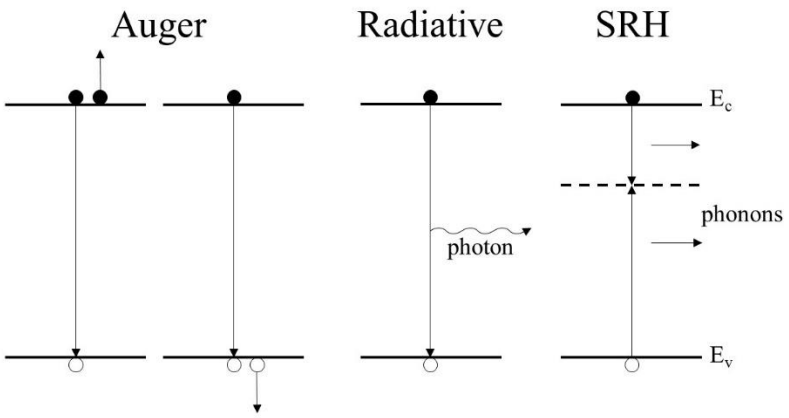

Figure 52. Carrier recombination mechanisms.

While there are several techniques available for measuring the carrier lifetime, microwave-reflectance (or microwave-detected) photoconductive decay (MW-PCD) was used in this research due to its ability to measure indirect band gap materials. The method is based on measuring the change in conductivity of a material after an initial pulse of laser light is used to excite the charge carriers. The microwaves are reflected off of the semiconductor and the intensity of the reflected microwave signal (which is dependent on the conductivity of the material) is measured. The amplitudes of the incident and reflected powers are related by the time constant, τ,

$$I = I_0 e^{-t/\tau} \tag{29}$$

The time-dependent excess carrier concentration, Δn(t), can be expressed as a ratio of the time-dependent conductivity, σ(t), and the mobilities, μ_e and μ_h,

$$\Delta n(t) = \frac{\sigma(t)}{q(\mu_e + \mu_h)} \tag{30}$$

This is how the changing conductivity is used to determine the decreasing minority carrier population as a function of time, resulting in the so-called minority carrier lifetime.

Minority carrier lifetime is a material property that is a good figure of merit for evaluating semiconductors with respect to carrier transport. There are many parameters that have the ability to influence both the actual lifetime and the measurable "effective" lifetime. Minority carrier lifetimes for direct bandgap materials are easily measured using straightforward photoluminescence (PL) techniques, but this method does not work for indirect bandgap materials such as silicon and AlSb. Also, the lifetimes for indirect-gap materials tends to be longer than for direct-gap, due to the necessary involvement of phonons in the recombination process [5], quenching radiative recombination [15].

In this study, the contactless method of measuring the carrier decay time by microwave-reflected photoconductive decay (MW-PCD) was used to determine the effect of p- and n-type doping. Results of this work are being prepared for publication.

4.3.2 MW-PCD Measurements

This process utilizes a light pulse from a laser to excite the carriers. Microwaves are directed toward the sample surface and a reflected microwave signal is measured. The intensity of the reflected signal is proportional to the conductivity, which decreases as the minority carrier population decreases as a result of recombination.

A schematic of the equipment setup is given in Figure 53 for the MW-PCD system used at the National Renewable Energy Laboratory (NREL) to perform measurements for this study. The spot size of the laser beam was about 1 cm diameter and the power was about 100 mW, with a laser pulse rate of 10 Hz. The pulse width was about 5 ns, ensuring that the carriers were nearly instantaneously excited. Measurements were taken using laser wavelengths of 1000, 920, 900, 880, 760, and 625 nm. During sample measurement, neutral density filters were used to attenuate the power. For the majority of the measurements the attenuation was 10^3.

The samples used for this study were the same as those used for the Hall study, outlined in Table 8, with AlSb layer doping densities ranging from unintentionally doped (UID) 2×10^8 cm^{-3} to moderately doped p- and n-type 1×10^{17} cm^{-3}. The undoped homoepitaxial GaAs sample was also included in consideration of contribution to the signal from the substrate.

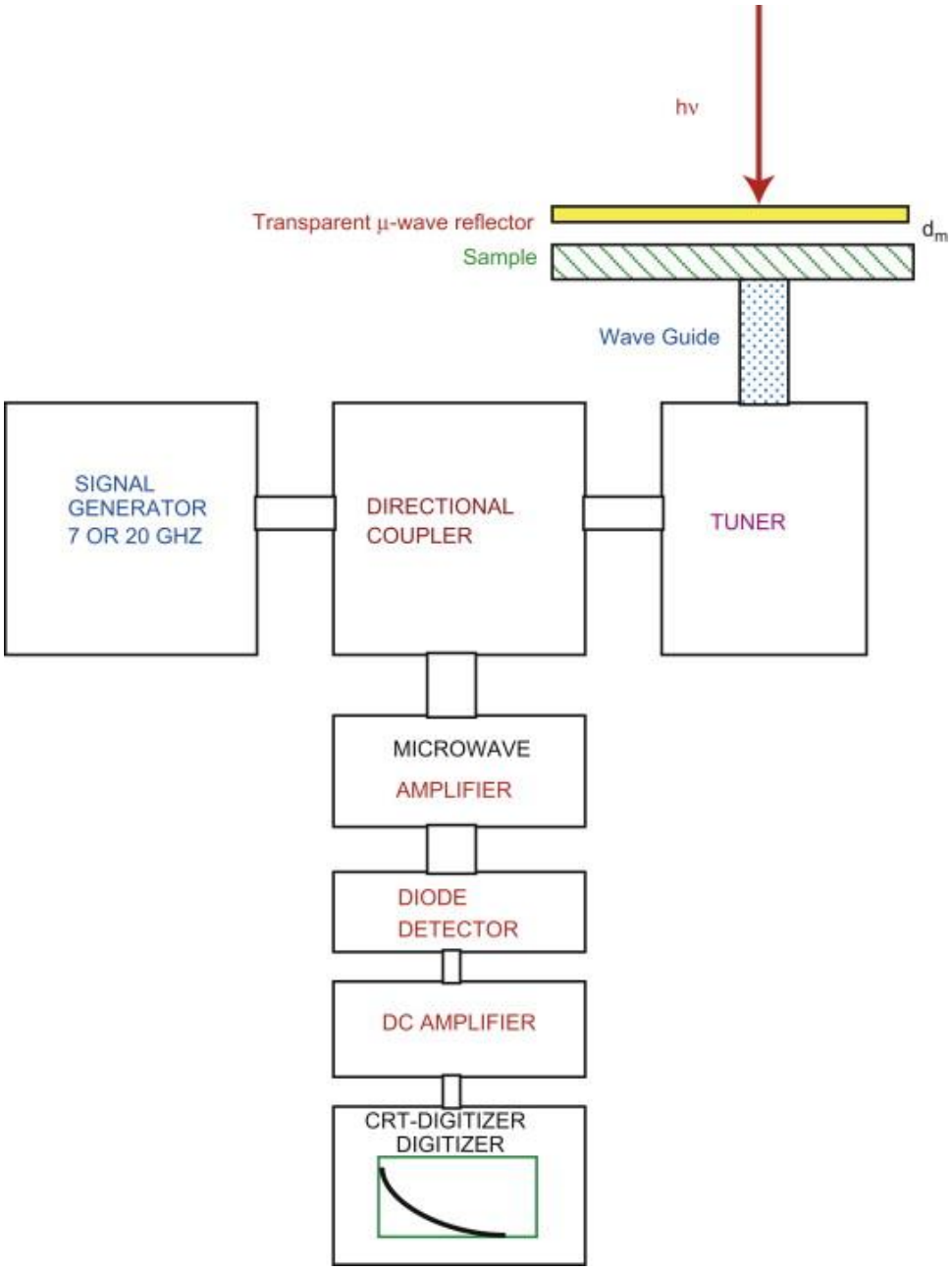

Figure 53. MW-PCD system diagram for setup at NREL [48].

4.3.3 Results & Analysis

For the MW-PCD measurements using laser wavelengths larger than 625 nm the decay behavior was very similar across all of the samples, including the GaAs sample. The signals had very long decay profiles, even as the wavelength reached far into the infrared region where signals were expected to disappear with sub-bandgap energy. As the bandgap for AlSb is 1.6 eV, it is essentially transparent for wavelengths longer than about 770 nm. Similarly, the GaAs substrate requires wavelengths shorter than about 880 nm to excite carriers in the 1.4 eV bandgap. Perhaps the measurements were representative of the GaAs substrate or the material used to support the samples during measurement, which would not show any variation with AlSb layer doping densities.

The 625 nm measurements revealed some distinction between the samples, with the GaAs sample following expected decay behavior with a single decay constant in the nanosecond range (Figure 54), and the other samples exhibiting a combination of multiple exponential decay curves (Figure 55, Figure 56, and Figure 57).

The results are plotted in groups according to the nature of the conductivity. In Figure 55, Figure 56, and Figure 57, the different decay regions are indicated by different colored line segments and boxes displaying associated decay constants. The insets in the doped sample plots show the time constants as a function of carrier concentration for each decay region.

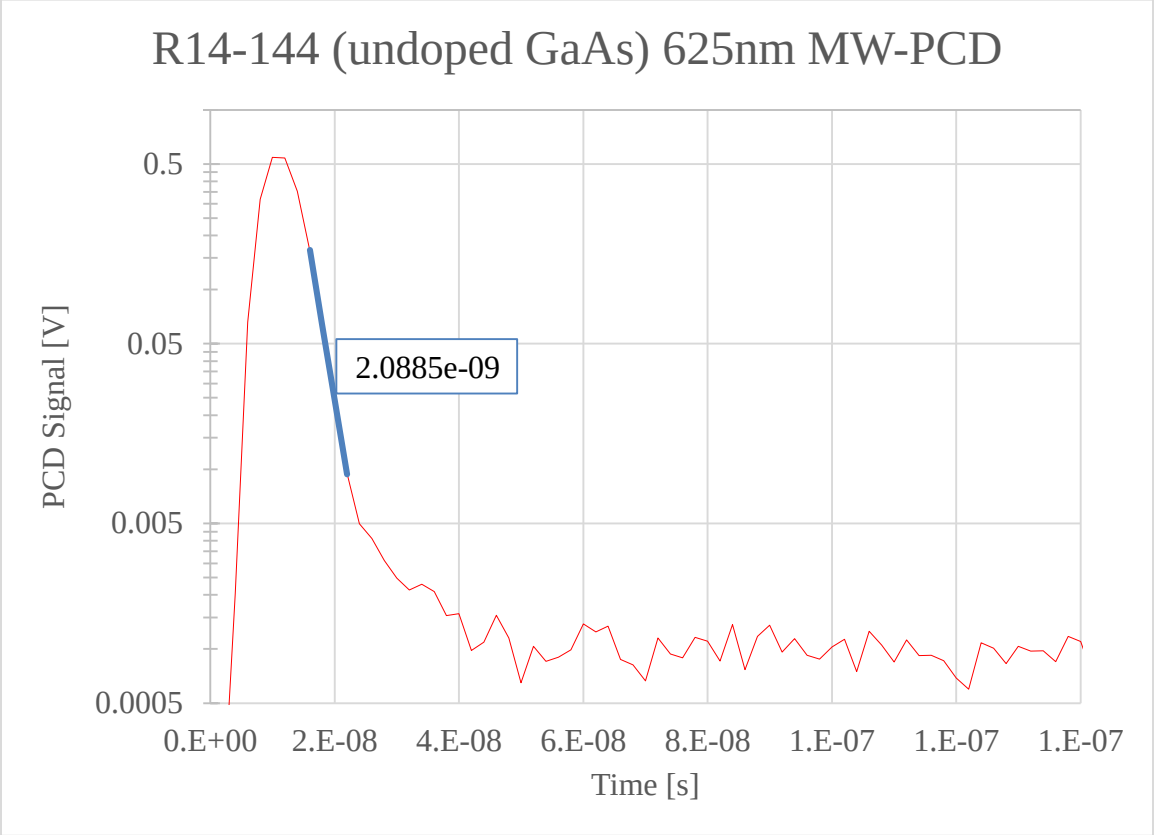

Figure 54. 625 nm MW-PCD results for R14-144 homoepitaxial GaAs sample, with the time constant associated with the decay indicated inside the blue box in units of s.

It appears that the dopants do have an effect on the decay signal, although the finding is in disagreement with initial expectations. Many researchers have observed decreased carrier lifetime for doped material, due to increased scattering. The results presented here clearly show longer decay times for doped samples, both p- and n-type, however the trend is not proportional to the doping concentration. One publication reported improved lifetime for compensated material [49], a phenomenon the researchers attributed to a reduction in recombination strength of the doping species and metal impurities by

increased compensation levels. Although, they admit that there may be a limit to the beneficial effects, and that further doping may degrade the lifetime behavior.

The other unusual feature seen in these plots is the multi-exponential shape of the decay curves, with at least three different decay regions, perhaps indicating different competing processes taking place. This phenomenon has been observed by others [50, 51, 52], where the behavior was explained by multiple trap levels within the bandgap, presumably associated with defects [50, 51, 52], or a transitional effect between surface and bulk recombination processes [51].

In Figure 58 the trend is nearly flat for the data points, indicating the negligible effect of doping concentration on carrier lifetime. Ahrenkiel *et al*. [53] published their work on doped InGaAs with the claim that the doping levels govern which recombination mechanism is favored. As the doping concentration increases from low to moderate to high, the dominant recombination process changes from Shockley-Read-Hall to radiative to Auger, respectively. In their study on doped silicon and germanium samples, Gaubas and Vanhellemont [51], report similar findings, with low to moderately doped material (up to about 10^{16} cm^{-3}) following Shockley-Read-Hall models, and heavily doped material dominated by Auger statistics.

Based on the literature [51, 53], it can be deduced that changes in doping concentrations do not influence the effective lifetime measurements in the SRH region, whereas in the radiative and Auger regions, increasing the doping level causes a proportional reduction in carrier lifetimes. Perhaps all of the samples measured in this study were doped mildly enough to remain in the SRH zone, where the doping has little effect

on the lifetime. Additional measurements with more highly doped samples should be taken to confirm this.

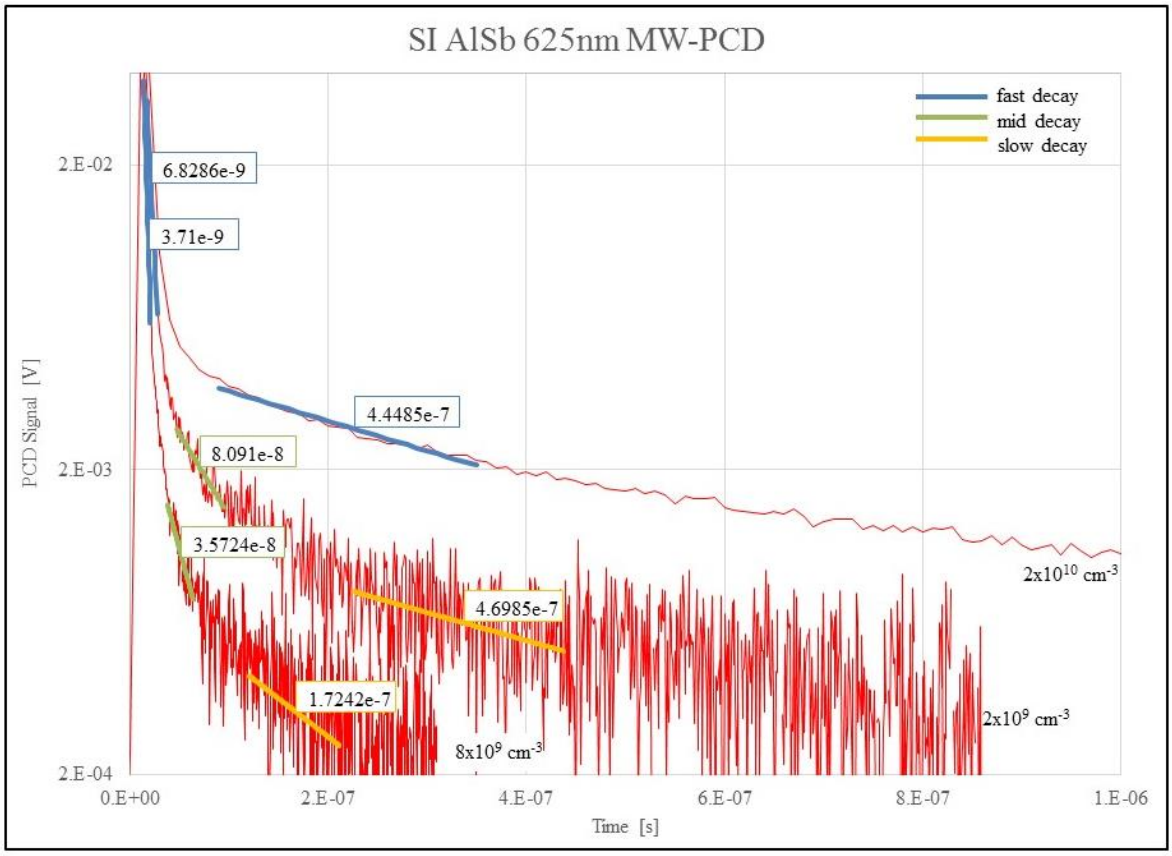

Figure 55. 625 nm MW-PCD results for semi-insulating samples R14-145 (middle curve), R14-175 (bottom curve), and R14-178 (top curve), with the associated Hall carrier concentration noted at the end of each curve and the decay time constants in the boxes next to each decay region in units of s.

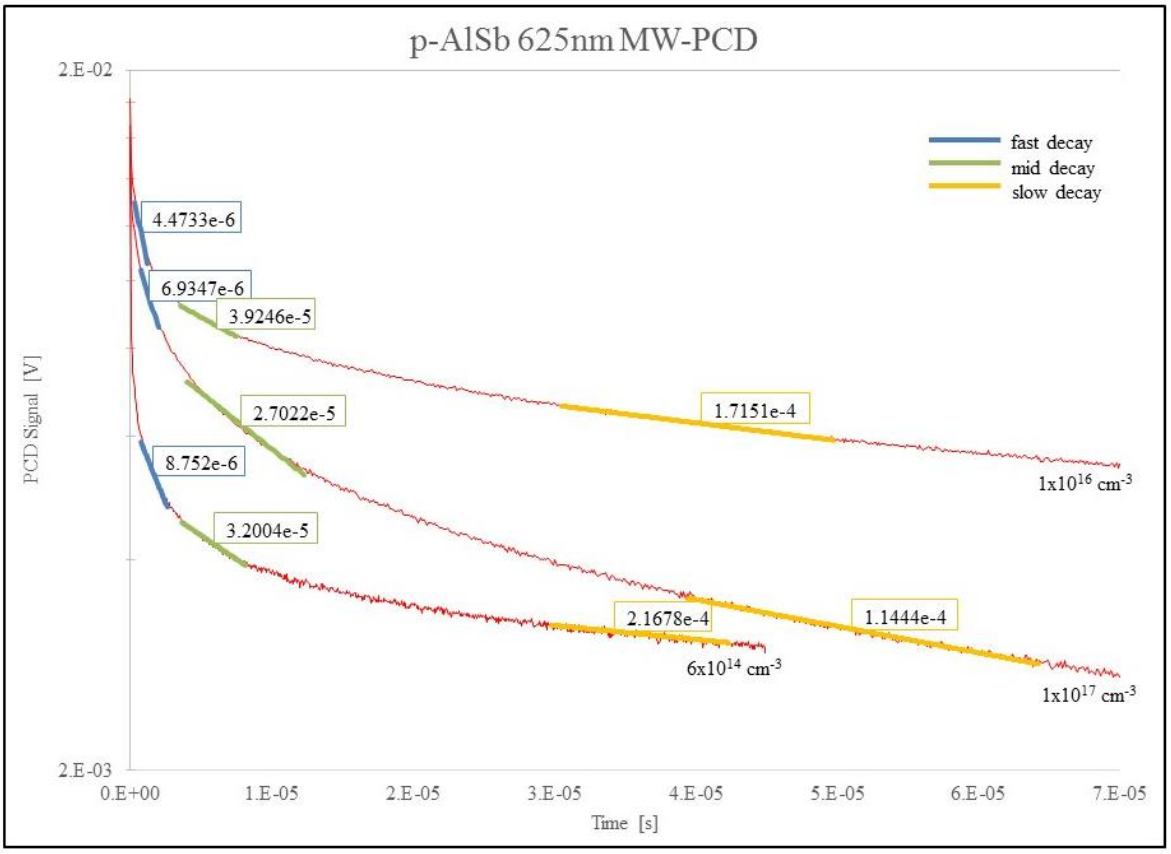

Figure 56. 625 nm MW-PCD results for p-type AlSb samples R14-174 (top curve), R14-171 (middle curve), and R14-176 (bottom curve), with the associated Hall carrier concentration noted at the end of each curve and the decay time constants in the boxes next to each decay region in units of s.

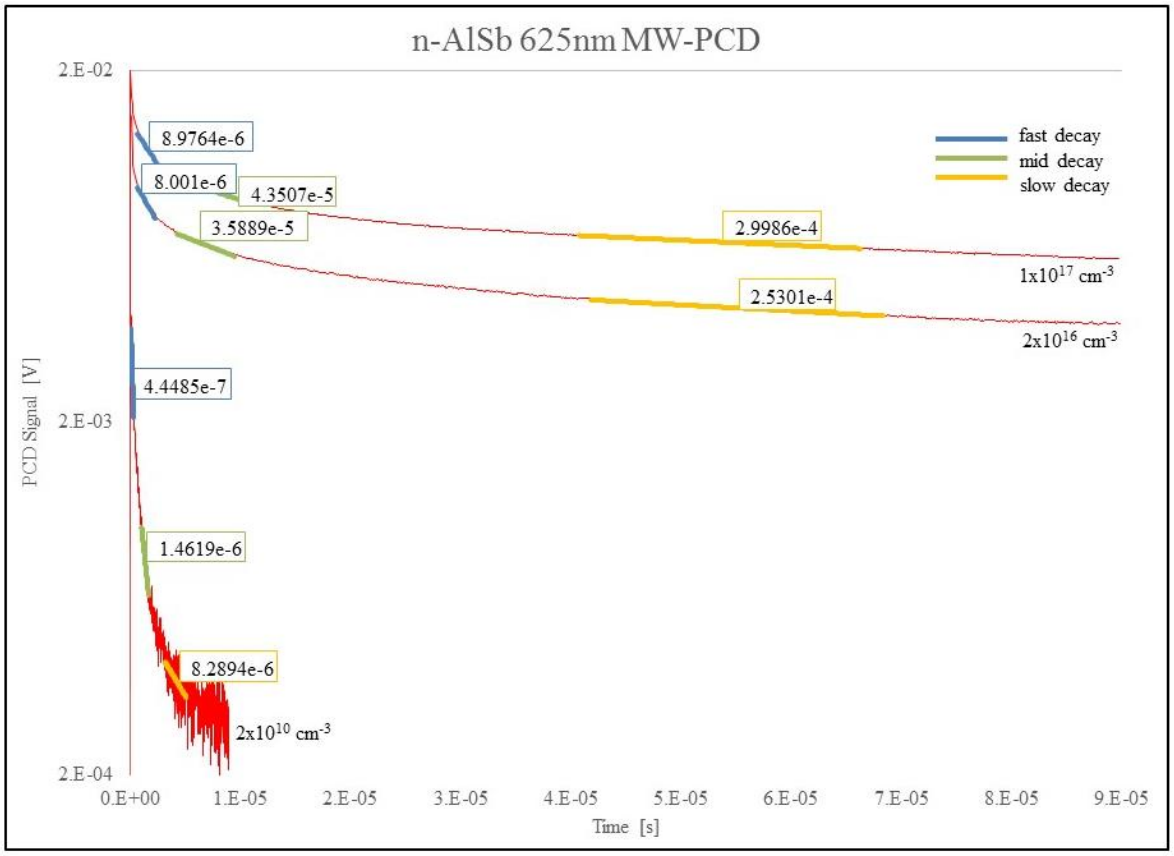

Figure 57. 625 nm MW-PCD results for n-type AlSb samples R14-177 (top curve), R14-172 (middle curve), R14-178 (bottom curve), with the associated Hall carrier concentration noted at the end of each curve and the decay time constants in the boxes next to each decay region in units of s.

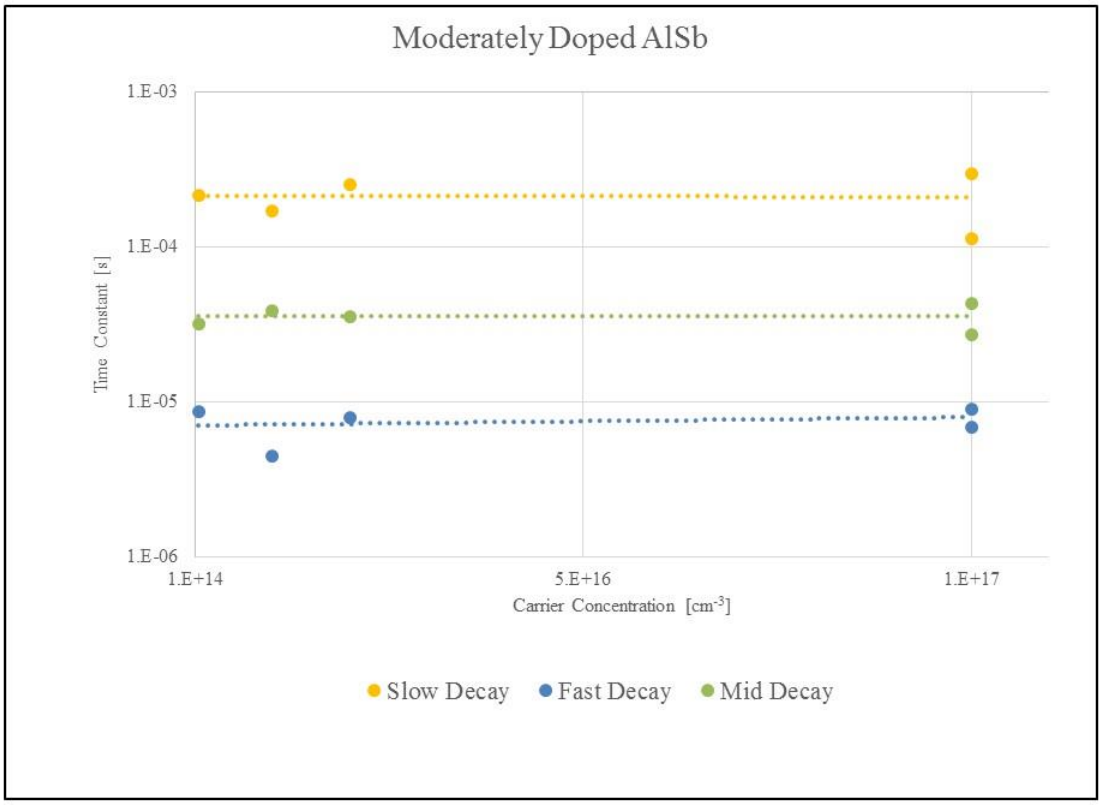

Figure 58. Time constants vs. carrier concentration for p- and n-type samples with densities larger than 1×10^{14} cm^{-3}.

Chapter 5

Discussion

5.1 Summary of Results

With MCNP benchmarking and simulations, it was shown that AlSb material had the potential to perform better than silicon with respect to counting statistics and low energy spectral features. Then, thin film AlSb was grown with very few surface defects and good quality lattice structure, despite the lattice mismatch between epitaxial layers. GaSb P-N diode structures were used to determine the effect of diode fabrication method on radiation response, with the finding that MBE grown structures behaved uniformly for similarly sized devices, whereas devices produced by ion-implantation were very irregular in their response. This observation was attributed to irregularity in the depletion width for the implanted samples, and very uniform depletion width in the epitaxial material. Next, the thin film AlSb P-I-N structures were characterized for their growth quality and radiation response. Charged particle spectra were obtained, with better signal to noise separation and counting statistics than was observed for GaSb.

A series of studies was conducted to investigate the important transport properties governing detector behavior for semiconductors. First, as part of a comprehensive Hall

study, the Hall carrier mobility was found to be optimal in undoped AlSb samples. The resistivity was also maximized when no doping was incorporated. Carrier lifetimes were examined in the MW-PCD study with the finding that undoped material suffers from very short recombination times. Samples doped both n- and p-type exhibited very long lifetimes with multiple exponential decay profiles, perhaps due to mid-gap trapping states.

5.2 Conclusions

While heavy charged particle detection is clearly possible using thin film AlSb, gamma- and x-ray detection has not been realized. However, there are several options for improvement in the design of the AlSb diode structure. Using a lattice-matched GaSb substrate would eliminate most of the strain-induced threading dislocations, reducing leakage currents. Also, growing a thicker AlSb layer would widen the depletion region and allow for larger signals.

The mobility-lifetime product is a well-established figure-of-merit for evaluating semiconductor radiation detectors, where larger values are ideal. Unfortunately, for AlSb the parameters cannot be optimized congruently; mobility is maximized in undoped material, whereas lifetime is longest for doped AlSb.

5.3 Future Work

To further characterize the drift behavior of the carriers a Modified Haynes-Shockley experiment [54] could be performed to measure the drift mobility of the electrons and holes independently. The measurement could be used to validate the high mobility results seen for undoped AlSb in the Hall study.

Also, as the AlSb P-I-N diode samples used for radiation response characterization were grown during a period where the MBE growths were inconsistent, perhaps either due to chamber issues or technician error, new samples should be grown. Later MBE growths for the transport studies were highly consistent and produced repeatable results. Diodes should be produced and spectra should then be re-measured with the higher quality material.

As mentioned in the previous section, GaSb substrate PIN diodes should also be fabricated to see if the radiation response can be further improved.

Appendix A

MCNPX Input Files

Simulated Spectra Distributions

```
Ba-122 Decay Energy Distribution:
SI1 L  0.00429 0.030625 0.030973 0.08  0.302851 0.356
SP1 D  0.163   0.351    0.643    0.341 0.1833   0.6205

Co-57 Decay Energy Distribution:
SI1 L  0.006409 0.006391 0.0144129 0.12206065 0.13647356
SP1 D  0.329    0.166    0.0916    0.856      0.1068
```

^{57}Co source incident on 5 microns AlSb

```
AlSb semiconductor detector

c cell cards
20 200  -0.0013    -7  8  1        $  "          "
21 200  -0.0013    -7 -8  9        $Variance Reduction
22 200  -0.0013    -7 -9  10       $  "          "
23 200  -0.0013    -7 -10 11       $  "          "
24 200  -0.0013    -7 -11          $  "          "
30 500  -19.3      -1 -2           $Gold
40 400  -5.61      -1 -3 2         $GaSb
50 100  -4.26      -1 -4 3         $AlSb
```

```
60 400   -5.61       -1 -5 4          $GaSb
70 300   -5.32       -1 -6 5          $GaAs
80 500   -19.3       -1 6             $Gold
90 200   -0.0013       1 -7           $Air
100 0                  7              $void

c surface cards
1   rpp         -1 1      -1 1         0 0.305584
2   pz   0.000100
3   pz   0.000200
4   pz   0.005200
5   pz   0.005300
6   pz   0.305300
7   rpp      -1.1 1.1    -1.1 1.1      -0.15 0.31
8   pz   -0.03
9   pz   -0.06
10  pz   -0.09
11  pz   -0.12

c data cards
nps 10000000
imp:p  1 1.23m 0.98m 1m 1 1 1 1 1 1 1 1 0
imp:e  1     1     1  1 1 1 1 1 1 1 1 0
mode p e
phys:p 100 1 0 0 0 0
m100   13027.04p       -0.5     $AlSb
       51000.04p       -0.5
m200    7000.04p -0.755636      $Air
        8000.04p -0.231475
       18000.04p -0.012889
m300   31000.04p       -0.5     $GaAs
       33074.04p       -0.5
m400   31000.04p       -0.5     $GaSb
       51000.04p       -0.5
m500   79197.04p       -1.0     $Gold
c - - - Materials - - - - - - - - - - - - - - - - - - -
m100   14000.04p       -1.0      $Si
m200   79000.04p       -1.0      $Au
```

```
m300     7000.04p -0.755636     $Air
         8000.04p -0.231475
        18000.04p -0.012889
c - - - Source - - - - - -Co-57 - - - - - - - - - - - - -
sdef pos=0 0 -0.14  par=2 erg=d1
SI1 L  0.006409 0.006391 0.0144129 0.12206065 0.13647356
SP1 D  0.329    0.166    0.0916    0.856      0.1068
c - - - Tallies - - - - - - - - - - - - - - - - - - - - -
f8:p 30
fmesh4*:p    geom=xyz    origin=-0.6 -0.6 -0.15
           imesh=0.6    iints=100
           jmesh=0.6    jints=100
           kmesh=0.006  kints=50
           factor=5e18
FT8 GEB 0 0.02 0
e8 0 1e-5 1000ilog 0.4
```

^{57}Co source incident on 50 microns SSB

```
Si detector with gold barrier layer
c cell cards
15 300 -0.0013     -3 -4          $ Var reduction cell
16 300 -0.0013     -3 -5 4        $  "                  "
17 300 -0.0013     -3 -6 5        $  "                  "
18 300 -0.0013     -3 -7 6        $  "                  "
19 300 -0.0013     -3  1 7        $  "                  "
20 200 -19.3       -1 -2          $ Gold
30 100 -2.33       -1  2          $ Si
40 0                3             $ Void

c Surface cards
1 rcc  0 0 0   0 0 0.0051     0.5
2 pz   0.0001
```

```
3 rpp  -0.6 0.6   -0.6 0.6   -0.15 0.006
4 pz   -0.12
5 pz   -0.09
6 pz   -0.06
7 pz   -0.03

c data cards
nps 10000000
imp:p 1 2.06m 1.05m 1.05m 0.595m 2.04m 1.15m 0
imp:e 1     1     1     1     1      1     1 0
mode p e
phys:p  100 1 0 0 0 0
c - - - Materials - - - - - - - - - - - - - - - - - - - - -
m100   14000.04p      -1.0            $Si
m200   79000.04p      -1.0            $Au
m300    7000.04p -0.755636            $Air
        8000.04p -0.231475
       18000.04p -0.012889
c - - - Source - - - - - - -Co-57 - - - - - - - - - - - -
sdef pos=0 0 -0.14  par=2 erg=d1
SI1 L  0.006409 0.006391 0.0144129 0.12206065 0.13647356
SP1 D  0.329    0.166    0.0916    0.856      0.1068
c - - - Tallies - - - - - - - - - - - - - - - - - - - - -
f8:p 30
fmesh4*:p    geom=xyz    origin=-0.6 -0.6 -0.15
           imesh=0.6    iints=100
           jmesh=0.6    jints=100
           kmesh=0.006  kints=50
           factor=5e18
FT8 GEB 0 0.02 0
e8 0 1e-5 1000ilog 0.4
```

^{133}Ba source incident on 5 microns AlSb

```
AlSb semiconductor detector
```

```
c cell cards
20 200  -0.0013     -7  8  1          $  "          "
21 200  -0.0013     -7 -8  9          $Variance Reduction
22 200  -0.0013     -7 -9  10         $  "          "
23 200  -0.0013     -7 -10 11         $  "          "
24 200  -0.0013     -7 -11            $  "          "
30 500  -19.3       -1 -2             $Gold
40 400  -5.61       -1 -3 2           $GaSb
50 100  -4.26       -1 -4 3           $AlSb
60 400  -5.61       -1 -5 4           $GaSb
70 300  -5.32       -1 -6 5           $GaAs
80 500  -19.3       -1 6              $Gold
90 200  -0.0013      1 -7             $Air
100 0                7                $void

c surface cards
1  rpp     -1.0 1.0   -1.0   1.0    0.0  0.305584
2  pz  0.000100
3  pz  0.000200
4  pz  0.005200
5  pz  0.005300
6  pz  0.305300
7  rpp     -1.1 1.1   -1.1   1.1   -0.15 0.31
8  pz  -0.03
9  pz  -0.06
10 pz  -0.09
11 pz  -0.12

c data cards
nps 10000000
imp:p  1 1.23m 0.98m 1m 1 1 1 1 1 1 1 1 0
imp:e  1     1     1  1 1 1 1 1 1 1 1 1 0
mode p e
phys:p 100 1 0 0 0 0
m100   13027.04p       -0.5    $AlSb
             51000.04p      -0.5
m200    7000.04p -0.755636    $Air
              8000.04p -0.231475
```

```
            18000.04p -0.012889
m300    31000.04p       -0.5    $GaAs
             33074.04p      -0.5
m400    31000.04p       -0.5    $GaSb
             51000.04p      -0.5
m500    79197.04p       -1.0    $Gold
c - - - Materials - - - - - - - - - - - - - - - - - - - - -
m100    14000.04p       -1.0            $Si
m200    79000.04p       -1.0            $Au
m300     7000.04p -0.755636             $Air
         8000.04p -0.231475
        18000.04p -0.012889
c - - - Source - - - - - - - - -Ba-133- - - - - - - - - - -
sdef pos=0 0 -0.14  par=2 erg=d1
SI1 L  0.00429 0.030625 0.030973 0.08  0.302851 0.356
SP1 D  0.163   0.351    0.643    0.341 0.1833   0.6205
c - - - Tallies - - - - - - - - - - - - - - - - - - - - -
f8:p 30
fmesh4*:p    geom=xyz    origin=-0.6 -0.6 -0.15
           imesh=0.6    iints=100
           jmesh=0.6    jints=100
           kmesh=0.006  kints=50
           factor=5e18
FT8 GEB 0 0.02 0
e8 0 1e-5 1000ilog 0.4
```

^{133}Ba source incident on 50 microns SSB

```
Si detector with gold barrier layer
c cell cards
15 300 -0.0013     -3 -4          $ Var reduction cell
16 300 -0.0013     -3 -5 4        $  "                "
17 300 -0.0013     -3 -6 5        $  "                "
```

```
18 300 -0.0013      -3 -7 6          $  "                  "
19 300 -0.0013      -3  1 7          $  "                  "
20 200 -19.3        -1 -2            $ Gold
30 100 -2.33        -1  2            $ Si
40 0                 3               $ Void

c Surface cards
1 rcc  0 0 0   0 0 0.0051   0.5
2 pz   0.0001
3 rpp  -0.6 0.6   -0.6 0.6   -0.15 0.006
4 pz   -0.12
5 pz   -0.09
6 pz   -0.06
7 pz   -0.03

c data cards
nps 10000000
imp:p 1 2.06m 1.05m 1.05m 0.595m 2.04m 1.15m 0
imp:e 1     1     1     1      1     1     1 0
mode p e
phys:p  100 1 0 0 0 0
c - - - Materials - - - - - - - - - - - - - - - - - - - - -
m100   14000.04p      -1.0            $Si
m200   79000.04p      -1.0            $Au
m300    7000.04p -0.755636            $Air
        8000.04p -0.231475
       18000.04p -0.012889
c - - - Source - - - - -Ba-133 - - - - - - - - - - - - - -
sdef pos=0 0 -0.14  par=2 erg=d1
SI1 L  0.00429 0.030625 0.030973 0.08  0.302851 0.356
SP1 D  0.163   0.351    0.643    0.341 0.1833   0.6205
c - - - Tallies - - - - - - - - - - - - - - - - - - - - - -
f8:p 30
fmesh4*:p    geom=xyz    origin=-0.6 -0.6 -0.15
           imesh=0.6    iints=100
           jmesh=0.6    jints=100
           kmesh=0.006  kints=50
           factor=5e18
```

FT8 GEB 0 0.02 0
e8 0 1e-5 1000ilog 0.4

Appendix B

Device Documentation

Current Source Mirror

Rev 1.0, 3-16-2015

Fred Husher

Overview

The current source mirror provides a step down translation of a programmable current source to provide an output of 1-100nA from a control input of 0.1-10mA. The compliance voltage can be manually adjusted between 10-100V. A compliance voltage monitor output provides a buffered 100:1 image of the output compliance voltage.

Circuit Description

The foundation of the current mirror is a Howland current source that is controlled by a current input to a load resistor. The control input current is flipped by a 1.00 ohm load resistor to 0.1-10mV. A buffer amplifier then drives the Howland current source, U3. Zero

offset correction of the overall converter is provided by the R22 trimpot. To avoid the feedback losses the current source output is buffered by a unity gain amplifier, U4. To ensure that the leakage paths of the output are minimal, the output is physically floated on a Teflon standoff post. Triaxial input and output connectors then ensure that the current signals are guarded. The overall transfer function is $I_{OUT}= I_{IN}(R4)$ or $I_{OUT} = (I_{IN})/100000$. All solder connections are done with Rosen core solder to ensure minimal noise.

The compliance voltage control is performed by a comparing the buffered feedback to the Howland current source with that of a reference voltage set by the front panel control, R15. When the compliance voltage is reached a clamp, Q1, is applied to the Howland feedback signal at the junction of R6 and R7. The clamp gain is set by the U2A feedback such that the V_{GS} of Q1 occurs when the compliance threshold is reached. Thereafter, Q1 is in its linear region and it can actively clamp the feedback signal. The compliance voltage can be monitored through a buffered output signal with a transfer function of 1V = 100V.

The entire current mirror circuit is shielded in an enclosure with a filtered power ground whose earth ground is established on the inside of the box via a ferrite bead. All power inputs to the enclosure are passed feed-through capacitors.

The power supply passes the AC through a two cascaded toroid transformers to minimize any line noise signals and reject magnetic field coupling. Both transformers are identical, but are wired differently: high to low voltage driving low to high voltage. To reduce the output voltages a series resistor, R101, drops the AC voltage into T102. The output windings of T102 provide about 110VAC and 20VAC. These two AC voltages are then

rectified and regulated to provide the necessary DC voltages for the current mirror: +125V, +15V, and -5V. The low voltages are half-wave rectified and regulated to develop +15V and -5V using three-terminal regulators. The high voltage is full-wave rectified to develop about +140VDC. The regulator circuit is a variant of the Miada HV regulator, see National Semiconductor Linear Brief #47 for a description of the Miada regulator. The main difference of this design is that it uses a deletion mode MOSFET, Q1, as the preliminary regulator. Depletion mode MOSFETs are normally on and become turned off as V_{GS} is applied. The control regulator, U1, is unable to handle a high voltage such as this without some help of a pre-regulator and a ramped control loop. Diodes D1 and D2 ensure that the regulator can never have more than 25V across its input to output. Thus, as the regulator is coming up to regulation the high voltage output occurs through these diodes. As soon as the voltage gradient across U1 drops below 25V the regulator U1 takes over control. Q1 is then able to perform the pre-regulation once the gradient across U1 drops to near V_{GS} of Q1. This all works because the low dropout regulator, U1, can operate (V_{in} to V_{out}) with less than the V_{GS} of Q1. This solution is more efficient in regulation than the original Miada or subsequent designs and provides a lower noise floor than previous designs. When power is turned off, the HV regulator is safely discharged through D3 and D4 into R4.

Operation

The current source mirror takes about 5-min to fully stabilize.

Alignment and Circuit Function Verification

*Note the test plugs are stored on the power supply PCB. The **compliance set plug** is a 10.0K resistor while the 10mA **I_{IN} test plug** is 4999 ohms (4.99K + 9.00ohms).*

- **HV adjustment**

  Adjust R11 on the voltage regulator PCB to +125V +-0.1V. The test point is the 200K, 1/2W resistor on the 6-pin connector side of the PCB.

- **Current source offset**

  Load the current source output with a 10.00M resistor. With no signal applied to the control input the voltage at U4-pin 6 to 0.00V. See the illustration below for the test point location.

- **Current source gain test**

  Load the current source output with a 10.00M resistor. Install the **I_{IN} test plug** into J207 with no signal into the control input. The output voltage seen at U4-pin 6 should be 1.00V. See the illustration below for the test point location.

- **Compliance voltage set**

  Remove all loading to the current source output. Install the **I_{IN} test plug** into J207 and the **compliance set plug** into J202. The voltage measured at U4-pin 6 should be nominally 10V. See the illustration below for the test point location. Note the slew rate for the compliance is slow to ensure that the noise floor is minimized.

Short the **compliance set plug** with a jumper and the compliance voltage should rise to nominally 100V.

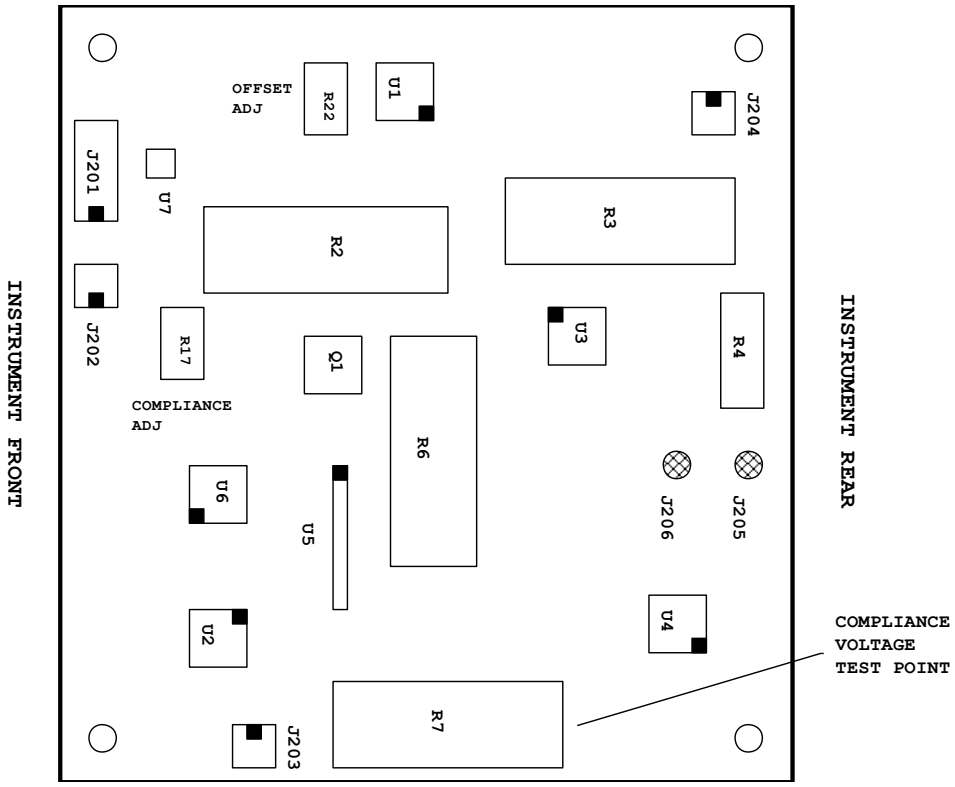

Figure 59. Schematic of current source mirror.

References

[1] H. Chen, S. A. Awadalla, P. Marthandam, K. Iniewski, P. H. Lu and G. Bindley, "CZT Device with improved sensitivity for medical imaging and homeland security applications," in *SPIE Invited Talk*, 2009.

[2] P. N. Luke and M. Amman, "Room-temperature replacement for Ge detectors - Are we there yet?," in *IEEE Nuclear Science Symposium Conference Record*, San Diego, 2006.

[3] G. A. Armantrout, S. P. Swierkowski, J. W. Sheroman and J. H. Yee, "What can be expected from high-Z semiconductor detectors?," *IEEE Transactions on Nuclear Science,* Vols. NS-24, no. No.1, pp. 121-125, February 1977.

[4] Z. He, "Review of the Shockley-Ramo theorem and its application in semiconductor gamma-ray detectors," *Nuclear Instruments and Methods in Physics Research A,* vol. 463, pp. 250-267, 2001.

[5] J. H. Yee, S. P. Swierkowski and J. W. Sheroman, "AlSb as a high-energy photon detector," *IEEE Transactions on Nuclear Science,* Vols. NS-24, no. No.4, pp. 1962-1967, August 1977.

[6] G. F. Knoll, Radiation Detection and Measurement, Fourth ed., John Wiley & Sons, Inc., 2010.

[7] G. Bertolini and A. Coche, Semiconductor Detectors, New York: John Wiley & Sons, Inc., 1968.

[8] M. J. Berger, J. H. Hubbell, S. M. Seltzer, J. Chang, J. S. Coursey, R. Sukumar, D. S. Zucker and K. Olsen, "XCOM: Photon Cross Sections Database, NIST Standard Reference Database 8 (XGAM)," 2001.

[9] G. Ottaviani, C. Canali and A. A. Quaranta, "Charge carrier transport properties of semiconductor materials suitable for nuclear radiation detectors," *IEEE Transactions on Nuclear Science*, Vols. NS-22, pp. 192-204, February 1975.

[10] V. Lordi, D. Aberg, P. Erhard and K. J. Wu, "First principles calculation of point defects and mobility degradation in bulk AlSb for radiaiton detection applicaiton," in *UCRL-PROC-233251 Hard X-Ray and Gamma-Ray Detector Physics VIII*, San Diego, 2007.

[11] [Online]. Available: Hyperphysics.phy-astr.gsu.edu/hbase/solids/Fermi.html#c2.

[12] R. E. Simspon, Introductory Electronics for Scientists and Engineers, Second ed., Allyn and Bacon, 1987.

[13] A. H. Titus, "CMOS photodetectors," *Photodiodes - World Activities in 2011*, 2011.

[14] K. Hecht, "Zum mechanismus des lichtelektrischen primastromes in isolierenden kristallen," *Z. Physik*, vol. 77, pp. 235-245, 1932.

[15] D. Aberg, P. Erhart, A. J. Williamson and V. Lordi, "Intrinsic point defects in aluminum antimonide," *Physical Review B,* vol. 77, no. 165206, 2008.

[16] V. E. Kutny, A. V. Rybka, A. S. Abyzov, L. N. Davydov, V. K. Komar, M. S. Rowland and C. F. Smith, "AlSb single-crystal grown by HPBM," *Nuclear Instruments and Methods in Physics Research A,* vol. 458, pp. 448-454, 2001.

[17] M. D. McCluskey, E. E. Haller and P. Becla, "Carbon acceptors and carbon-hydrogen complexes in AlSb," *Physical Review B,* vol. 65, no. 045201, 2001.

[18] M.-H. Du, "Defects in AlSb: A density functional study," *Physical Review B,* vol. 79, no. 045207, 2009.

[19] C. T. Lin, E. Schonherr and H. Bender, "Growth and characterization of doped and undoped AlSb single crystals," *Journal of Crystal Growth,* vol. 104, pp. 653-660, 1990.

[20] P. Erhart, D. Aberg, B. W. Sturm, K.-J. Wu and V. Lordi, "Theory-guided growth of aluminum antimonide single crystals with optimal properties for radiation detection," *Applied Physics Letters ,* vol. 97, no. 142104, 2010.

[21] A. F. Witt, P. Becla, C. Counterman, J. DiFrancesco, G. Landahl, K. Morse and J. Sanchez, "Top-seed solution growth and characterization of AlSb single crystals for gamma-ray detectors," DOE Grant # DE-FG08-94NV11627, 1995.

[22] Z.-Q. Zhou, y.-Q. Xu, R.-T. Hao, B. Tang, Z.-W. Ren and Z.-C. Niu, "Molecular beam epitaxy of GaSb on GaAs substrates with AlSb buffer layers," *Chinese Physics Letters*, vol. 26, no. 1, 2009.

[23] S. Subbanna, G. Tuttle and H. Kroemer, "N-type doping of gallium antimonide and aluminum antimonide grown by molecular beam epitaxy using lead telluride as a tellurium dopant source," *Journal of electronic materials*, vol. 17, no. 4, pp. 297-303, 1988.

[24] B. R. Bennett, W. J. Moore, M. J. Yang and B. V. Shanabrook, "Transport properties of Be- and Si-doped AlSb," *Journal of Applied Physics*, vol. 87, no. 11, pp. 7876-7879, 2000.

[25] S. Schulz, "CVD Deposition of Binary AlSb ang GaSb Material Films - A Single-Source Approach," in *Precursor Chemistry of Advanced Materials: CDV, ALD and Nanoparticles*, Berlin Heidelberg, Springer-Verlag, 2005, pp. 101-123.

[26] C. Chang, H. Takaoka, L. Chang and L. Esaki, "Molecular beam epitaxy of AlSb," *Applied Physics Letters*, vol. 40, no. 11, pp. 983-985, 1982.

[27] B. R. Bennet and B. V. Shanabrook, "Molecular Beam Epitaxy of Sb-based Semiconductors," in *Thin Films: Heteroepitaxial Systems* , Singapore, World Scientific, 1999, pp. 401-452.

[28] A. Furukawa and S. Ideshita, "Origin of deep donors in AlSb grown by molecular beam epitaxy," *Journal of Applied Physics*, vol. 75, no. 10, pp. 5012-5015, 1994.

[29] G. Balakrishnan, S. Huang, L. R. Dawson, Y.-C. Xin, P. Conlin and D. L. Huffaker, "Growth mechanisms of highly mismatched AlSb on a Si substrate," *Applied Physics Letters*, vol. 86, no. 034105, 2005.

[30] J. E. Ayers, Heteroepitaxy of Semiconductors; Theory, Growth and Characterization, Boca Raton: CRC Press Taylor and Francis Group, 2007.

[31] A. Jallipalli, G. Balakrishnan, S. H. Huang, T. J. Rotter, K. Nunna, B. L. Liang, R. L. Dawson and D. L. Huffaker, "Structural analysis of highly relaxed GaSb grown on GaAs substrates with periodic interfacial array of 90 degree misfit dislocations," *Nanoscale Research Letters*, vol. 4, no. 12, 2009.

[32] *MCNP - A General Monte Carlo N-Particle Transport, Version 5*, Vols. Volume I: Overview and Theory, Rev. Feb 2008.

[33] *MCNP - A General Monte Carlo N-Particle Transport, Version 5*, Vols. Volume II: User's Guide, Rev Feb 2008.

[34] E. I. Vaughan, N. Rahimi, G. Balakrishnan and A. A. Hecht, "Thin-film gallium antimonide for room-temperature radiation detection," *Journal of Electronic Materials*, vol. 44, no. 10, pp. 3288-3293, 2015.

[35] J. F. Ziegler, M. D. Ziegler and J. P. Biersack, "SRIM - The stopping and range of ions in matter (2010)," *Nuclear Instruments and Methods in Physics Research B*, vol. 268, 2010.

[36] N. Rahimi, A. A. Aragon, O. S. Romero, D. M. Shima, T. J. Rotter, G. Balakrishnan, S. D. Mukherjee and L. F. Lester, "Characterization of surface defects on Be implanted GaSb," *Journal of Vacuum Science and Technology B*, vol. 32, no. 4, 2014.

[37] N. Rahimi, A. A. Aragon, O. S. Romero, D. S. Shima, T. J. Rotter, G. Balakrishnan, S. D. Mukherjee and L. F. Lester, "Electrical and microstructure analysis of nickel-based low-resistance ohmic contacts to n-GaSb," *Applied Physics Letters - Materials* , vol. 1, no. 062105, 2013.

[38] A. Coche and P. Siffert, "N-P Detectors," in *Semicomductor Detectors*, New York, John Wiley & Sons, Inc., 1968, p. 107.

[39] R. Steinberg, "A technique for increasing the sensitivity of a solid-state fission probe," NASA, Washington, 1961.

[40] R. T. Klann and D. S. McGregor, "Development of coated gallium arsenide neutron detectors," in *ICONE-8110*, Baltimore, 2000.

[41] E. I. Vaughan, S. Addamane, D. M. Shima, G. Balakrishnan and A. A. Hecht, "High-Resistivity Semi-insulating AlSb on GaAs Substrates Grown by Molecular Beam Epitaxy," *Journal of Electronic Materials*, pp. 1-6, 2016.

[42] E. I. Vaughan, S. Addamane, D. Shima, G. Balakrishnan and A. A. Hecht, "Molecular Beam Epitaxy of High-Resistivity AlSb for Room-Temperature

Radiation Detectors," in *IEEE Nuclear Science Symposium and Medical Imaging Conference*, San Diego, 2015.

[43] G. Bertolini, "Pulse Shape and Time Resolution," in *Semiconductor Detectors*, New York, John Wiley & Sons, Inc., 1968, p. 243.

[44] S. Tiwari, Compound Semiconductor Device Physics, Boston: Academic Press, 1992.

[45] D. K. Schroder, Semiconductor Material and Device Characterization, New York: John Wiley & Sons, Inc, 1998.

[46] D. A. Neaman, Semiconductor Physics and Devices: Basic Principles, Third ed., McGraw-Hill, 2003.

[47] S. M. Sze, Physics of Semiconductor Devices, Second ed., New York: John Wiley & Sons, Inc., 1981.

[48] R. K. Ahrenkiel and S. W. Johnston, "Lifetime analysis of silicon solar cells by microwave reflection," *Solar Energy Materials & Solar Cells*, vol. 92, pp. 830-835, 2008.

[49] S. Dubois, N. Enjalbert, F. Servant, J. P. Garandet, R. Monna and J. Kraiem, "Beneficial effects of dopant compensation on carrier lifetime in upgraded metallurgical silicon," in *1445 23rd PVSC*, 2008.

[50] M. Ichimura, H. Tajiri, Y. Morita, N. Yamada and A. Usami, "Excess carrier lifetime of 3C-SiC measured by the microwave phoconductive decay method," *Applied Physics Letters,* vol. 70, no. 13, pp. 1745-1747, 1997.

[51] E. Gaubas and J. Vanhellemont, "Comparitive study of carrier lifetime dependence on dopand concentration in silicon and germanium," *Journal of the Electrochemical Society,* vol. 154, no. 3, pp. H231-H238, 2007.

[52] S. A. Studenikin and M. Cocivera, "Time-resolved luminescence and photoconductivity of polycrystalline ZnO films," *Journal of Applied Physics,* vol. 91, no. 8, pp. 5060-5065, 2001.

[53] R. K. Ahrenkiel, R. Ellingson, S. Johnston and M. Wanlass, "Recombination lifetime of In0.53Ga0.47As as a function of doping density," *Applied Physics Letters* , vol. 72, no. 26, pp. 3470-3472, 1998.

[54] C. S. Mayberry, D. Huang, G. Balakrishnan, C. Kouhestani, N. Islam, S. R. J. Brueck and A. K. Sharma, "Characterization of carrier transport properties in strained crystalline Si wall-like structures in the quasi-quantum regime," *Journal of Applied Physics,* vol. 118, no. 134301, 2015.

[55] S. P. Swierkowski and G. A. Armantrout, "Prognosis for high-Z semiconductor detectors," *IEEE Transactions on Nuclear Science,* Vols. NS-22, pp. 205-210, February 1975.

[56] A. Owens, "Semiconductor materials and radiation detection," *Journal of Synchrotron*, vol. 13, pp. 143-150, 2006.

[57] D. S. McGregor and H. Hermon, "Room-temperature compound semiconductor radiation detectors," *Nuclear Instruments and Methods in Physics Research A*, vol. 395, pp. 101-124, 1997.

[58] W. R. Thurber, "Semiconductor and Dimensional Metrology Division: The Hall Effect," NIST, [Online]. Available: www.nist.gov/pml/div683/hall_effect.cfm.

[59] F. Hartmann, Evolution of Silicon Sensor Technology in Particle Physics, Berlin Heidelberg: Springer, 2009.

[60] F. V. Wald, J. Bullit and R. O. Bell, "Bi2S3 as a high Z material for gamma-ray detectors," *IEEE Transactions on Nuclear Science*, Vols. NS-22, pp. 246-250, February 1975.

[61] H. A. J. Smith and M. Lucas, "Gamma-Ray Detectors," in *Passive Nondestructive Assay of Nuclear Materials*, Washington DC, Office of Nuclear Regulatory Research, 1991, pp. 43-63.

[62] A. Silenas, K. Pozela, L. Dapkus, V. Jasutis, V. Juciene, P. J and K. M. Smith, "Graded-gap AlxGa1-xAs X-ray detector with collected charge multiplication," *Nuclear Instruments and Methods in Physics Research A*, vol. 509, pp. 30-33, 2003.

[63] S.-H. Park, H. S. Kim, H.-S. Shin and H.-D. Kim, "Development of InSb semiconductor detector for high resolution radiation measurment," *Journal of the Korean Physical Society*, vol. 58, no. 6, pp. 1577-1580, June 2011.

[64] R. Pani, R. F. Laitano and R. Pellegrini, "Diagnostic x-ray spectra measurements using a silicon surface barrier detector," *Phys. Med. Biol*, vol. 32, no. 9, pp. 1135-1149, 1987.

[65] D. S. McGregor, R. A. Rojeski, G. F. Knoll, F. L. J. Terry, J. East and Y. Eisen, "Present status of undoped semi-insulating LEC bulk GaAs as a radiation spectrometer," *Nuclear Instruments and Methods in Physics Research A*, vol. 343, pp. 527-538, 1994.

[66] O. Limousin, "New trends in CdTe and CdZnTe detectors for X- and gamma-ray applications," *Nuclear Instruments and Methods in Physics Research Aq*, vol. 504, pp. 24-37, 2003.

[67] I. Kanno, Y. Morita, Y. Sato, A. Birumachi, T. Nakamura and M. Katagiri, "Radiation detection by liquid phase epitaxially grown InSb detector," *Progress in Nuclear Science and Technology*, vol. 1, pp. 214-217, 2011.

[68] A. Kargar, A. M. Jones, W. J. McNeil, M. J. Harrison and D. S. McGregor, "CdZnTe Frisch collar detectors for gamma-ray spectroscopyq," *Nuclear Instruments and Methods in Physics Research A*, vol. 558, pp. 497-503, 2006.

[69] C. R. Gruhn, "Epitaxial silicon semiconductor detectors; Past developments, future prospects," *IEEE Transactions on Nuclear Science*, Vols. NS-24, no. 1, pp. 93-103, February 1977.

[70] L. M. Federov, D. I. Mikulik, T. A. Orlova, N. K. Panteleev, N. A. Poletaev, C. A. Snytkina and Y. V. Zhilyaev, "GaAs P-I-N structures as detectors of x-ray radiation," in *III Nanotechnology International Forum*, 2011.

[71] M. Fiederle, F. A, J. Konrath, V. Babentsov, J. Franc and R. B. James, "Comparison of undoped and dopes high resistivity CdTe and (Cd,Zn)Te detector crystals," *IEEE Transactions on Nuclear Science*, vol. 51, no. 4, pp. 1864-1868, August 2004.

[72] M. Tani, K.-S. Lee and X.-C. Zhang, "Detection of terahertz radiation with low-temperature-grown GaAs-based photoconductive antenna using 1.55 um probe," *Applied Physics Letters*, vol. 77, no. 9, pp. 1396-1398, 28 August 2000.

[73] V. Virkkala, V. Havu, F. Tuomisto and M. J. Puska, "Native point defect energetics in GaSb: Enabling p-type conductivity of undoped GaSb," *Physical Review B*, vol. 86, no. 144101, 2012.

[74] R. Linnebach and K. W. Benz, "Bridgman growth of AlS," *Journal of Crystal Growth*, vol. 53, pp. 579-585, 1981.

[75] C. T. Lin, E. Schonherr, H. Bender and C. Busch, "On the growth of AlSb single crystals," *Journal of Crystal Growth*, vol. 94, pp. 955-958, 1989.

[76] B. R. Bennet, R. Magno and N. Papnicolaou, "Controlled n-type doping of antimonides and arsenides using GaTe," *Journal of Crystal Growth* , vol. 251, pp. 532-537, 2003.

[77] P. Hill, N. Weisse-Bernstein, R. L. Dawson, P. Dowd and S. Krishna, "Activation energies for Te and Be in metamorphically grown AlSb and InxAl1-xSb layers," *Applied Physics Letters,* vol. 87, no. 092105, 2005.

[78] A. Nakagawa, J. J. Pekarik, H. Kroemer and J. H. English, "Deep levels in Te-doped AlSb grown by molecular beam epitaxy," *Applied Physics Letters* , vol. 57, no. 15, pp. 1551-1553, 1990.

[79] V. M. Kaganer, R. Kohler, M. Schmidbauer and R. Opitz, "X-ray diffraction peaks due to misfit dislocations in heteroepitaxial structures," *Physical Review B,* vol. 55, no. 3, pp. 1793-1810, 1997.

[80] B. Brar and D. Leonard, "Spiral growth of GaSb on (001) GaAs using molecular beam epitaxy," *Applied Physics Letters,* vol. 66, no. 4, pp. 463-465, 1995.

[81] "Hall Effect in Semiconductor," 20 9 2013. [Online]. Available: www.advancedlab.org/mediawiki/index.php/Hall_Effect_in_Semiconductor.

[82] Ortec, "Overview of Semiconductor Photon Detectors," 2010. [Online]. Available: www.ortec-online.com.

[83] "Appendix A: Hall Effect Measurements," in *Lake Shore 7500/9500 Series Hall System User's Manual*.

[84] L. J. van der Pauw, "A method of measuring the resistivity and Hall coefficient on lamellae of arbitrary shape," *Philips Technical Review,* vol. 20, no. 8, pp. 220-224, 1958.

[85] S. P. Swierkoski, "A comprehensive model for predicting semiconductor detector performance," *IEEE Transactions on Nuclear Science,* Vols. NS-23, no. 1, pp. 131-137, 1976.

[86] C. A. C. Sequeira and D. M. F. Santos, "Hall effect measurements on p-n-p InP structures," *Brazilian Journal of Physics* , vol. 38, no. 1, pp. 147-155, 2008.

[87] M. P. G, Y. I. Khlebnikov, S. V. Regula, Y. Gao and T. S. Sudarshan, "High resistivity measurement of SiC Wafers using different techniques," *Journal of Electronic Materials* , vol. 32, no. 6, pp. 505-510, 2003.

[88] K. MacLean, T. S. Mentzel and M. A. Kastner, "Measuring charge transport in a thin solid film using charge sensing," *Nano Letters,* vol. 10, pp. 1037-1040, 2010.

[89] J. Lindermuth, "Hall mobility measurement of solar cell material," *Magnetics Technology International: Semiconducting Materials,* pp. 36-39, 2012.

[90] P. M. Hemenger, "Measurement of high resistivity semiconductors using the van der Pauw method," *Review of Scientific Instruments,* vol. 44, no. 6, pp. 698-700, 1973.

[91] Green, Robert; Keithley Instruments Inc., "White Paper: Hall Effect Measurements in Materials Characterization," 2011. [Online].

[92] D. C. Cronemeyer, "Hall and drift mobility in high-resisitvity single-crystal silicon," *Physical Review,* vol. 105, no. 2, pp. 522-523, 1957.

[93] G. Cavalleri, G. Fabri, E. Gatti and V. Svelto, "On the induced charge in semiconductor detectors," *Nuclear Instruments and Methods,* vol. 21, pp. 177-178, 1963.

[94] G. Cavelleri, E. Gatti, G. Fabri and V. Svelto, "Extension of Ramo's theorem as applied to induced charge in semiconductor detectors," *Nuclear Instruments and Methods* , vol. 92, pp. 137-140, 1971.

[95] Y. Gu, J. P. Romankiewicz, J. K. David, J. L. Lensch and L. J. Lauhon, "Quantitative measurement of the electron and hole mobility-lifetime products in semiconductor nanowires," *Nano Letters,* vol. 6, no. 5, pp. 948-952, 2006.

[96] J. F. Butler, C. L. Lingren and F. P. Doty, "CD1-xZnxTe gamma ray detectors," *IEEE Transactions on Nuclear Science* , vol. 39, no. 4, 1992.

[97] E. D. Klema, "Preparation of high-resistivity silicon surface-barrier detectors for use at large reverse bias voltages," *Nuclear Instruments and Methods,* vol. 26, pp. 205-208, 1964.

[98] E. E. Haller, H. W. Kraner and W. A. Higinbotham, "Nuclear Radiation Detector Materials," in *Materials Research Society Symposia Proceedings*, Boston, 1982.

[99] A. Owens and A. Peacock, "Compound semiconductor radiaiton detectors," *Nuclear Instruments and Methods in Physics Research A,* vol. 531, pp. 18-37, 2004.

[100] W. J. McNeil, D. S. McGregor, A. E. Bolotnikov, G. W. Wright and R. B. James, "Single-charge-carrier-type sensing with an insulated Frisch ring CdZnTe semiconductor radiation detector," *Applied Physics Letters,* vol. 84, 2004.

[101] N. Rahimi, A. A. Aragon, O. S. Romero, D. M. Shima, T. J. Rotter, G. Balakrishnan, S. D. Mukherjee and L. F. Lester, "Electrical and microstructure analysis of nickel-based low-resistance ohmic contacts to n-GaSb," *Applied Physics Letters - Materials*, vol. 1, no. 062105, 2013.

[102] W. Shi, Y. Zheng, Y. Guo, Y. Zhang, H. Xu, L. Wang and Y. Xia, "Electrical properties of radiation detector based on polycrystalline mercuric iodide (HgI2) thick film," in *SPIE*, Shanghai, 2008.

[103] G. C. Sun, M. Lenoir, E. Breelle, H. Samic, J. C. Bourgoin, H. El-Abbassi, P. J. Sellin and J. P. Montagne, "X-ray detector with thick epitaxial GaAs grown by

chemical reaction," in *Nuclear Science Symposium Conference Record*, Norfolk, 2002.

[104] F. Nava, P. Vanni, C. Lanzieri and C. Canali, "Epitaxial silicon carbide charge particle detectors," *Nuclear Instruments and Methods in Physics Research A*, vol. 437, no. 2-3, pp. 354-358, 1999.

[105] M. Rogalla, K. Runge and Soldner-Rembold, "Particle detectors based on semi-insulating silicon carbide," *Nuclear Physics B - Proceedings Supplements*, vol. 78, pp. 516-520, 1999.

[106] J. W. Murphy, L. Smith, J. Calkins, G. R. Kunnen, I. Mejia, K. D. Cantley, R. A. Chapman, J. Sastre-Hernandez, R. Mendoza-Perez, G. Contreras-Puente, D. R. Allee, M. Quevedo-Lopez and G. B, "Thin film cadmium telluride charged particle sensors for large area neutron detector," *Applied Physics Letters* , vol. 105, no. 112107, 2014.

[107] P. J. Sellin, "Thick film compound semiconductors for x-ray imaging applications," *Nuclear Instruments and Methods in Physics Research A*, vol. 563, no. 1, 2006.

[108] Q. Jiang, A. W. Brinkman, P. Veeramani and P. J. Sellin, "Epitaxial Growth of High-Resistivity CdTe Thick Films Grown Using a Modified Close Space Sublimation Method," *Japanese Journal of Applied Physics*, vol. 49, no. 2R, 2010.

[109] M. J. Sinnot, The Solid State for Engineers, New York: John Wiley & Sons, Inc., 1958.

[110] G. Lutz, Semiconductor Radiation Detectors, Berlin: Springer-Verlag, 1999.

[111] T. E. Schlesinger and R. B. James, Semiconductors and Semimetals: Semiconductors for Room Temperature Nuclear Detector Applications, vol. 43, San Diego: Academic Press, Inc, 1995.

[112] C. Hilsum and A. C. Rose-Innes, Semiconducting III-V Compounds, New York: Pergamon Press, 1961.

[113] R. J. Malik, Materials Processing Theory and Practices Volume 7: III-V Semiconductor Materials and Devices, Amsterdam: North Holland, 1989.

[114] P. W. Nicholson, Nuclear Electronics, London: John Wiley & Sons, Inc., 1974.

[115] D. Macdonald and A. Cuevas, "Trapping of minority carriers in multicrystalline silicon," *Applied Physics Lettersq*, vol. 74, no. 12, pp. 1710-1712, 1999.

[116] K. Lauer, M. Blech, A. Laades and A. Lawerenz, "Investigation of minority carrier trapping in silicon by MWPCD measurements," in *24th European Photovoltaic Solar Energy Conference*, Hamburg, Germany, 2009.

[117] A. R. K, R. Ellingson, S. Johnston and M. Wanlass, "Recombination lifetime of In0.53Ga0.47As as a function of doping density," *Applied Physics Letters*, vol. 72, no. 26, pp. 3470-3472, 1998.